Composite Structures 354 (2025) 118801

Contents lists available at ScienceDirect

Composite Structures

journal homepage: www.elsevier.com/locate/compstruct

Effect of thermal and electric coupling on the multifield response of laminated shell structures employing higher-order theories

Francesco Tornabene *, Matteo Viscoti, Rossana Dimitri

Department of Engineering for Innovation, University of Salento, 73100 Lecce, Italy

A R T I C L E I N F O

Keywords:
Magneto-electro-elastic materials
Equivalent Layer-Wise
Generalized Differential Quadrature
Higher-order theories
Navier solution
Recovery procedure
Smart structures

A B S T R A C T

The paper introduces a refined formulation, based on higher-order theories, for the thermo-electro-elastic analysis of laminated shell structures made of smart materials. The formulation employs a generalized higher-order model to describe the configuration variables, following the Equivalent Single Layer and Equivalent-Layer-Wise approaches. After presenting an effective homogenization procedure for thermo-electro-elastic smart composites, the fundamental equations are derived in curvilinear principal coordinates, taking into account the coupling effects among mechanical elasticity, electricity, and heat conduction. A semi-analytical solution is then obtained using Navier's method. Furthermore, the three-dimensional response of the panel is determined through a recovery procedure that applies the Generalized Differential Quadrature (GDQ) numerical method.

Numerical examples are provided, where the formulation is applied to both straight and curved panels subjected to various surface actions. These examples point out the coupling effect between different physical phenomena on the multifield three-dimensional response. Furthermore, the numerical results based on the proposed formulation are verified to be consistent with predictions from finite-element-based models, despite the reduced computational cost.

The manuscript enables in a simple way the study of physical couplings between different fields that are not considered in most commercial software. As a result, this formulation offers a valuable tool for designing doubly-curved laminated panels made of innovative smart materials for novel engineering applications.

1. Introduction

In recent years, there has been a growing interest on smart structures [1,2] made of advanced innovative materials. Novel applications in manufacturing industry, aerospace, structural monitoring, medical devices and other fields have increasingly relied on structural components that are sensitive not only to mechanical forces, but also to environmental conditions [3,4]. In this context, new engineering challenges have been studied, including sensors, actuators, and energy harvesting problems [5–7]. In addition, the structural design requires the development of elements with a reduced weight and size, while ensuring an adequate structural response under various multifield actions, including mechanical forces, electric and magnetic field, as well as hygro-thermal environmental variations.

In this context, advanced modelling strategies are required to accurately predict the multifield response of these structures. Various works have been presented in literature to model the coupling effects between different physical phenomena to account for their mutual interactions. The introduction of additional Degrees of Freedom (DOFs) yields a high computational cost, with the necessity of developing advanced modelling strategies. A milestone in this research area is the development of two-dimensional theories for analyzing straight and curved panels extensively used in common engineering applications [8–13]. These theories are based on pre-determined axiomatic assumptions for describing the unknown variables along the thickness direction. The Classical Plate Theory (CPT) accounts for a linear distribution of in-plane displacement field components and a uniform vertical deflection [14], while the First-order Shear Deformation Theory (FSDT) introduces an angular quantity among the DOFs, and the Third-order Shear Deformation Theory (TSDT) provides a third-order expansion of the unknown field variables [15,16]. However, it has been shown that only higher-order kinematic models can accurately predict the response of moderately thick shell structures, while classical approaches are not sufficiently accurate [17]. Thus, a generalized formulation has been

* Corresponding author.
E-mail address: francesco.tornabene@unisalento.it (F. Tornabene).

https://doi.org/10.1016/j.compstruct.2024.118801
Received 22 September 2024; Received in revised form 17 November 2024; Accepted 10 December 2024
Available online 20 December 2024

developed, which adopts the governing equations for laminated structures based on an arbitrary expansion of the unknown field variables along the thickness direction with generalized thickness functions [18,19]. As a result, several structural theories can be easily obtained by adopting specific expressions for these functions. On the other hand, in the case of laminated structures with softer layers within the lamination scheme, it has been shown that a Layer-Wise (LW) approach is appropriate [20,21]. Following the LW framework, the kinematic model is assigned to each layer, and the assembly of the equations through interlaminar compatibility conditions allows one to obtain the fundamental governing equations for the entire structure. In a previous work [22], it has been shown that various polynomials can be adopted to this end. On the other hand, when the thickness functions set is directly assigned to the entire laminate, an Equivalent Single Layer (ESL) model is obtained. Several formulations accounting for polynomial thickness functions can be found in the literature [23,24]. However, in some cases, trigonometric functions have been demonstrated to be a valid alternative [25–28]. In this context, the interlaminar deformation is well described if the so-called zigzag functions are adopted within the kinematic model, as shown in the work by Murakami [29,30]. More specifically, a general zigzag function is usually adopted, accounting for a slope variation in the vertical deflection. In Refs. [31,32], a refined zigzag theory has been presented, where the thickness functions set is derived from the mechanical shear properties of the laminate under consideration. Furthermore, in Ref. [33], analytical expressions for thickness functions are provided, derived from the geometric properties of the structure itself. A hybrid approach, named Equivalent Layer-Wise (ELW), has been also introduced, where the functions usually adopted in LW theories are applied to the ESL formulation [34–37]. In this way, it is possible to derive a model with three-dimensional Dirichlet boundary conditions, where a prescribed value of the unknown field variable is specified in a particular region of the solid. Some possible applications of this approach include displacement-imposed mechanical problems, hygro-thermal simulations with prescribed temperature and humidity, and electric problems with prescribed electric voltage.

In multifield problems [38], higher-order theories have been adopted to predict the piezoelectric response of smart laminated sensors. More specifically, power series expansions are extensively used to derive the electric voltage induced by the deflection of a panel. As shown in Ref. [5], the piezoelectric problem can be addressed using both power series [39–41] and trigonometric series expansions [42–44]. Various formulations have been provided for laminated structures with a piecewise variation of the material properties and for Functionally Graded Materials (FGM), which are characterized by a continuous smooth variation of material properties along the thickness direction [45,46]. In all these models, it is essential to develop a strategy to obtain the homogenized properties of an equivalent continuum material. Models of different complexities have been proposed. Each methodology is based on the definition of a proper reference volume element, and the equivalent multifield properties are derived through proper multifield reference load cases [47–49]. In this way, some analytical expressions have been derived, which can be grouped into series and parallel configurations. Another classification separates homogenization techniques that consider the geometric properties of each phase within the unit cell from those that adopt only their multifield properties, while the influence of the geometric configuration is neglected [50]. The latter approach provides accurate results only when the concentration of inclusions is relatively low compared to the whole size of the unit cell. An alternative approach, based on a volume deformation, is the well-known Mori-Tanaka's theory [51], which has been largely used to derive the homogenized properties of multiphase materials with dispersed short fibers [52,53]. This methodology can be also used for higher values of the volume fractions of inclusions. For multifield problems, the Mori-Tanaka's theory has been successfully adopted in Ref. [54] to obtain the analytical expression of the homogenized properties of a magneto-electro-elastic two-phase composite material consisting of cylindrical fibers embedded in an isotropic matrix. As cited in Ref. [54], materials simultaneously exhibiting piezoelectric and piezomagnetic properties are adopted in various applications, including energy harvesting, logical memory, miniature antennas, sensors and actuators, and thermal imaging, among others. It should be noted that for practical applications these materials should be characterized by large magneto-electric effect at a given temperature, therefore two- or three-phase materials are preferred to single phase materials with magnetic and electric polarization. To model these smart materials in numerical simulations, advanced modeling strategies are required which consider multiphysic phenomena. Among literature, two-dimensional approaches are extensively adopted which can be seen as an enhancement of plate and shell theories for mechanical elasticity.

The solution of the two-dimensional model can be used to obtain the dispersion of configuration variables such as displacement field components, temperature increment, and electric voltage [55–59]. For a mechanical elasticity problem, a post-processing correction of stress and strain profiles is necessary to obtain an accurate distribution of these quantities [60,61]. Indeed, the reconstruction of the actual response of a panel from the higher-order two-dimensional solution does not ensure a-priori the correct loading conditions at the top and bottom of the laminate. For this reason, a correction of stress and strain profiles derived from higher-order definition equations and constitutive relations is mandatory. Since the obtained profile depends on various factors including geometry, lamination scheme, loading conditions, and material variations, a numerical algorithm is adopted in this procedure rather than analytical expressions. The numerical procedure must be both accurate and computationally efficient.

One important issue in developing very complex structural theories is the validation of the model, as results from existing literature can be very scarce, and commercial codes often do not account for all aspects of the theory like pyroelectricity when developing a validation model [62–64]. For this reason, closed-form analytical solutions are usually derived under some specific assumptions, including geometry, material models, and boundary conditions [65–68]. In this context, the well-known Navier method allows one to derive a solution for simply-supported spherical panels with cross-ply lamination schemes. Furthermore, other mathematical strategies are available to derive proper analytical solutions for various boundary conditions, including cylindrical bending [69,70] and fully-clamped boundary conditions [71–73]. On the other hand, approximate solutions can be derived for a general configuration of panels. For instance, in Refs. [74,75] a solid shell element model is developed for curved structures with distributed piezoelectric sensors and actuators which account for pyroelectric effect. Here, it is shown that the stress distribution is rarely affected by pyroelectric effect, while electric potential and electric displacements are influenced by the presence of temperature variations within the solid. Mechanical and multifield problems are frequently addressed using the Finite Element Method (FEM), which involves the use of pre-determined shape functions within the computational domain, obtained from a proper discretization of the physical domain into regions called finite elements [76,77]. The main issue related to FEM is the local interpolation of the unknown variable, where the higher-order compatibility is not guaranteed a priori among adjacent elements. Therefore, accurate solutions can be only derived with refined meshes, with a high computational cost. This problem has been overcome by spectral collocation methods [78], which interpolate the unknown variables throughout the entire physical domain. In this way, the governing equations are solved by using a limited number of sampling points, with a significant reduction of the computational cost [79]. Among these methods, the Generalized Differential Quadrature (GDQ) has been extensively applied in structural mechanics problems due to its simplicity and accuracy [80,81]. Based on a higher-order interpolation of variables, the GDQ method approximates the derivatives with a weighted sum of the functional values and proper weighting coefficients that depend on the specific interpolation technique. Another important aspect is that the GDQ allows to solve the fundamental equations of a given problem directly in the strong form without using shape functions. This makes the numerical implementation relatively simple compared to other numerical techniques [82]. The GDQ method has been successfully applied to various engineering problems, including the free vibration analysis [83,84], transient simulations [85], and fracture mechanics problems [86,87]. Furthermore, general formulations have been developed for multi-domain simulations. Moving from GDQ, an efficient numerical technique called Generalized Integral Quadrature (GIQ) has been developed for the numerical computation of integrals [88]. Moreover, the Taylor-Based Generalized Integral Quadrature (T-GIQ) and the Harmonic Differential Quadrature (HDQ) are alternative versions of GIQ, using Taylor series and Fourier series expansions, respectively [89].

Referring to multifield problems, few works have been produced that fully couple thermal and electric fields with the mechanical elasticity in two-dimensional higher-order theories and solve the coupled multifield problem, accounting for all possible effects among these phenomena. As a consequence, the main purpose of this work is to investigate the multifield response of curved laminated structures under thermal and electric loading conditions, employing higher-order theories and a generalized formulation. More specifically, an arbitrary kinematic model is adopted in the formulation according to the ESL and ELW frameworks, allowing for the prescription of arbitrary values of multifield unknown variables at the top and bottom surfaces. The fundamental equations, derived in curvilinear principal coordinates, consider not only piezoelectric and thermal expansion effects but also the influence of temperature variations on the electric field distribution within the three-dimensional solid. A closed-form Navier solution is derived, and a recovery procedure, based on multifield balance equations and GDQ numerical technique, is adopted to derive the actual response of the three-dimensional solid. A systematic investigation is conducted in selected case studies, where the present higher-order formulation is used to study the multifield behavior of various laminated structures made of smart materials, treated with a continuum homogenization model. For each example, the model is successfully validated against 3D FEM, demonstrating the accuracy and computational convenience of higher-order two-dimensional theories compared to three-dimensional formulations. With many coupled numerical examples, otherwise not addressed by commercial packages, the paper explores new insights in multifield analysis of laminated shell structures, thus enabling the possibility to adopt smart materials for thermo-electro-mechanical novel engineering devices.

2. Higher-order thermo-electro-elastic theory for doubly-curved shells

This section introduces a generalized ESL and ELW thermo-electro-elastic theory for doubly-curved laminated panels, following the ESL approach. The fundamental equations are derived in curvilinear principal coordinates based on the Master Balance principle, and a semi-analytical Navier solution is derived under specific geometric, material, and mechanical assumptions. Within the ESL framework, a reference surface is defined, such that the position vector $\mathbf{R}$ of an arbitrary point is expressed as follows [38]:

$$\mathbf{R}(\alpha_1,\alpha_2,\zeta) = \mathbf{r}(\alpha_1,\alpha_2) + \frac{h(\alpha_1,\alpha_2)}{2} z\ \mathbf{n}(\alpha_1,\alpha_2) \tag{1}$$

Here, $\mathbf{r}$ denotes the position vector of the reference surface, which is described using the curvilinear principal coordinates $\alpha_i = \alpha_1, \alpha_2$, while $h(\alpha_1,\alpha_2)$ represents the total thickness of the shell. A rectangular physical domain $[\alpha_1^0,\alpha_1^1] \times [\alpha_2^0,\alpha_2^1]$ is defined, where $\alpha_i^0 < \alpha_i^1$ with $i = 1,2$. Furthermore, the parameter $z = 2\zeta/h$ is a dimensionless variable that depends on the thickness coordinate ζ. As shown in Eqn. (1), this coordinate is oriented along the outward normal unit vector $\mathbf{n}(\alpha_1,\alpha_2)$ of the reference surface, which is defined at each point of the physical domain as follows:

$$\mathbf{n}(\alpha_1,\alpha_2) = \frac{\mathbf{r}_{,1} \wedge \mathbf{r}_{,2}}{\left|\mathbf{r}_{,1} \wedge \mathbf{r}_{,2}\right|} \tag{2}$$

In the previous equation, $\mathbf{r}_{,i} = \partial\mathbf{r}/\partial\alpha_i$ represents the partial derivative of the reference surface position vector $\mathbf{r}$ with respect to $\alpha_i = \alpha_1, \alpha_2$ principal coordinates. Moreover, the first-order in-plane derivatives of $\mathbf{r}$ are used to derive the Lamé parameters of the reference surface, denoted by $A_i = A_1, A_2$, as defined by:

$$A_i(\alpha_1,\alpha_2) = \sqrt{\mathbf{r}_{,i}\cdot\mathbf{r}_{,i}} \tag{3}$$

Similarly, the principal radii of curvature of an arbitrary parametric line on the shell are introduced. If $\mathbf{r}_{,ij} = \partial^2\mathbf{r}/\left(\partial\alpha_i\partial\alpha_j\right)$ denotes the second-order partial derivative of the position vector $\mathbf{r}$ with respect to the principal coordinate $\alpha_i,\ \alpha_j = \alpha_1,\ \alpha_2$, the following definition is employed:

$$R_i(\alpha_1,\alpha_2) = -\frac{\mathbf{r}_{,i}\cdot\mathbf{r}_{,i}}{\mathbf{r}_{,ii}\cdot\mathbf{n}} \tag{4}$$

These quantities are used to express the infinitesimal arch length $ds_i = ds_1, ds_2$ along an arbitrary $\alpha_i = \alpha_1, \alpha_2$ principal direction in terms of an infinitesimal variation $d\alpha_i = d\alpha_1, d\alpha_2$. This leads to the introduction of the curvilinear coordinate $s_i \in [0, L_i]$:

$$ds_i = A_i d\alpha_i \tag{5}$$

The total length L_i along α_i principal direction is calculated for flat and curved panels, under certain geometric assumptions [38]. More specifically, uniform principal Lamé parameters, as defined in Eqn. (3), and uniform principal radii of curvature (4) are considered. In other words, it is assumed that the derivatives of these quantities remain uniform throughout the physical domain:

$$\frac{\partial^{n+m}A_1}{\partial s_1^n \partial s_2^m} = 0, \quad \frac{\partial^{n+m}A_2}{\partial s_1^n \partial s_2^m} = 0, \quad \frac{\partial^{n+m}R_1}{\partial s_1^n \partial s_2^m} = 0, \quad \frac{\partial^{n+m}R_2}{\partial s_1^n \partial s_2^m} = 0 \tag{6}$$

In this way, the quantities $L_i = L_1, L_2$ are evaluated as follows, setting $s_i^j = \alpha_i^j R_i$ for $i = 1,2$ and $j = 0,1$:

$$L_i = s_i^1 - s_i^0 = \left(\alpha_i^1 - \alpha_i^0\right) R_i \tag{7}$$

For a circular cylinder with $R_1 = +\infty$ and $R_2 = R$, the generatrix forms a circular arc, coinciding with the generatrix along the α_2 principal direction. Thus, Eqn. (7) can be written as $L_1 = s_1^1 - s_1^0 = \alpha_1^1 - \alpha_1^0$ and $L_2 = s_2^1 - s_2^0 = \left(\alpha_2^1 - \alpha_2^0\right)R$. On the other hand, if $R_1 = R$ and $R_2 = +\infty$, the generatrix lies along α_1 principal direction, and the quantities L_1 and L_2 are evaluated as $L_1 = s_1^1 - s_1^0 = \left(\alpha_1^1 - \alpha_1^0\right)R$ and $L_2 = s_2^1 - s_2^0 = \alpha_2^1 - \alpha_2^0$. Finally, the total thickness of the shell h is computed at each point of the physical domain as the sum of the individual thicknesses h_k with $k = 1, \dots, l$ of all layers in the stacking sequence. For an arbitrary $k-$th lamina of the shell located between heights ζ_k and ζ_{k+1}, one gets:

$$h(\alpha_1,\alpha_2) = \sum_{k=1}^{l} h_k(\alpha_1,\alpha_2) = \sum_{k=1}^{l} \left(\zeta_{k+1} - \zeta_k\right) \tag{8}$$

At this point, a generalized kinematic model is introduced, accounting for an arbitrary expansion of multifield configuration variables. These variables include the components $U_1^{(k)}, U_2^{(k)}$ and $U_3^{(k)}$ of the three-dimensional displacement field vector associated with the geometric reference system $\alpha_1, \alpha_2, \zeta$, measured in [m], as well as the electrostatic potential $\Delta\phi^{(k)} = \phi^{(k)} - \phi_0$ and the temperature variation $\Delta T^{(k)} = T^{(k)} - T_0$ with respect to the stress-free reference configuration of the solid, measured in [V] and [K], respectively. In addition, the reference values for the electric potential and absolute temperature are denoted by ϕ_0 and T_0, respectively. These quantities are organized in vector $\boldsymbol{\Delta}^{(k)}$, defined at each point of an arbitrary $k-$th layer of the three-dimensional solid with $k = 1,...,l$. The generalized model considers an arbitrary expansion of each element of $\boldsymbol{\Delta}^{(k)}$, consisting of $N+2$ terms, taking into account an arbitrary set of thickness functions $F_\tau^{(k)\alpha_i} = F_\tau^{(k)\alpha_i}(\zeta)$ with $\tau = 0,...,N+1$ and $i = 1, ..., 5$. By introducing vector $\boldsymbol{\delta}^{(\tau)}(\alpha_1,\alpha_2)$ of generalized configuration variables for each $\tau = 0,...,N+1$, the kinematic model can be expressed as follows [38]:

$$\boldsymbol{\Delta}^{(k)} = \sum_{\tau=0}^{N+1} \boldsymbol{F}_\tau^{(k)} \boldsymbol{\delta}^{(\tau)} \Leftrightarrow \begin{bmatrix} U_1^{(k)} \\ U_2^{(k)} \\ U_3^{(k)} \\ \Delta\phi^{(k)} \\ \Delta\mathrm{T}^{(k)} \end{bmatrix} = \sum_{\tau=0}^{N+1} \begin{bmatrix} F_\tau^{(k)\alpha_1} & 0 & 0 & 0 & 0 \\ 0 & F_\tau^{(k)\alpha_2} & 0 & 0 & 0 \\ 0 & 0 & F_\tau^{(k)\alpha_3} & 0 & 0 \\ 0 & 0 & 0 & F_\tau^{(k)\alpha_4} & 0 \\ 0 & 0 & 0 & 0 & F_\tau^{(k)\alpha_5} \end{bmatrix} \begin{bmatrix} u_1^{(\tau)} \\ u_2^{(\tau)} \\ u_3^{(\tau)} \\ \phi^{(\tau)} \\ \kappa^{(\tau)} \end{bmatrix} \tag{9}$$

Note that the formulation is derived regardless of the specific form of each thickness function. Furthermore, Eqn. (9) enables the derivation of various two-dimensional theories of different orders by choosing a particular expression for $F_\tau^{(k)\alpha_i}$, including classical theories such as FSDT and TSDT. Following the ELW approach, in the present work the following thickness function set is adopted for $\tau = 0,...,N$, where $\widetilde{z} = 2\zeta/h$ is a dimensionless parameter depending on coordinate ζ which identifies the points of the solid along the thickness direction [38]:

$$F_\tau^{(k)\alpha_i}(\zeta) = \begin{cases} \dfrac{1-\widetilde{z}}{2} & \text{for } \tau = 0 \\ \widetilde{z}^{\tau+1} - \widetilde{z}^{\tau-1} & \text{for } \tau = 1,..,N-1 \\ \dfrac{1+\widetilde{z}}{2} & \text{for } \tau = N \end{cases} \tag{10}$$

Finally, the following expression is adopted for any $\tau = N+1$:

$$F_{N+1}^{(k)\alpha_i}(\zeta) = \begin{cases} (-1)^k \widehat{z}_k = -\dfrac{\zeta-\zeta_1}{\zeta_2-\zeta_1} & \text{for } k = 1 \\ (-1)^k z_k = (-1)^k \left(2\dfrac{\zeta-\zeta_k}{\zeta_{k+1}-\zeta_k} - 1 \right) & \text{for } k = 2,...,l-1 \\ (-1)^k \breve{z}_k = (-1)^l \dfrac{\zeta-\zeta_{l+1}}{\zeta_{l+1}-\zeta_l} & \text{for } k = l \end{cases} \tag{11}$$

It should be also noted that thickness functions in Eqns. (10)-(11) assume a null value at the top and bottom surfaces of the laminate, for $\tau = 1,...,N-1$, while assuming a unit value at the bottom and top surface, for $\tau = 0$ and $\tau = N$, respectively. As a consequence, the generalized ELW unknown variables with $i = 1,...,5$ represent the prescribed values of configuration unknowns at the outer layers of the shell:

$$\begin{aligned} \Delta_i^{(1)}\left(\alpha_1,\alpha_2,\zeta = -\frac{h}{2}\right) &= \delta_i^{(0)}(\alpha_1,\alpha_2) \\ \Delta_i^{(l)}\left(\alpha_1,\alpha_2,\zeta = \frac{h}{2}\right) &= \delta_i^{(N)}(\alpha_1,\alpha_2) \end{aligned} \tag{12}$$

On the other hand, the ESL formulation uses the set of thickness functions reported below, which are associated with $\tau = 0,...,N+1$ kinematic expansion orders:

$$F^{(k\tau)\alpha_i}(\zeta) = \begin{cases} \zeta^\tau & \text{for } \tau = 0,...,N \\ (-1)^k z_k = (-1)^k \dfrac{2}{\zeta_{k+1}-\zeta_k}\zeta - \dfrac{\zeta_{k+1}+\zeta_k}{\zeta_{k+1}-\zeta_k} & \text{for } \tau = N+1 \end{cases} \tag{13}$$

for any $k = 1, ..., l$. At this point, the nomenclature ELD $-N$ and ELDZL $-N$ is introduced to clearly identify the specific kinematic model used in each simulation. The acronym "EL" denotes the ELW kinematic model, while "D" indicates that the unknown configuration variables for the mechanical elasticity case are the displacement field components. In addition, N represents the maximum kinematic expansion order as shown in Eqn. (9). Finally, "ZL" is used when the ELW zigzag function (11) is considered within the kinematic model. In the same way, for the ESL kinematic model, the acronyms ED $-N$ and EDZ $-N$ are used. In this case, "Z" indicates that the zigzag function from Eqn. (13) for $\tau = N+1$ is used within the model, while "E" denotes the ESL formulation.

Once the kinematic model is established using the generalized model in Eqn. (9), higher-order equations are derived from those ones for a doubly-curved three-dimensional solid. More specifically, the present thermo-electro-mechanical formulation accounts for the vectors of primary variables, including the three-dimensional strain vector $\boldsymbol{\varepsilon}^{(k)} = \begin{bmatrix} \varepsilon_1^{(k)} & \varepsilon_2^{(k)} & \gamma_{12}^{(k)} & \gamma_{13}^{(k)} & \gamma_{23}^{(k)} & \varepsilon_3^{(k)} \end{bmatrix}^T$, the electrostatic field $\boldsymbol{\theta}^{(k)} = \begin{bmatrix} \theta_1^{(k)} & \theta_2^{(k)} & \theta_3^{(k)} \end{bmatrix}^T$, and the temperature gradient $\mathscr{E}^{(k)} = \begin{bmatrix} \mathscr{E}_1^{(k)} & \mathscr{E}_2^{(k)} & \mathscr{E}_3^{(k)} \end{bmatrix}^T$, all referring to the curvilinear reference system $O'\alpha_1\alpha_2\zeta$. In addition to these vectorial quantities, the relation $\widehat{\Delta\mathrm{T}}^{(k)} = \Delta\mathrm{T}^{(k)}$ is also introduced. These vectors are included in vector $\boldsymbol{\pi}^{(k)} = \begin{bmatrix} \boldsymbol{\varepsilon}^{(k)T} & \mathscr{E}^{(k)T} & \widehat{\Delta\mathrm{T}}^{(k)} & \boldsymbol{\theta}^{(k)} \end{bmatrix}^T$. As a consequence, the electro-thermo-mechanical definition of equations [38] for a doubly-curved three-dimensional solid can be expressed in a compact matrix form by introducing a proper differential operator $\mathbf{D}$ as follows:

$$\boldsymbol{\pi}^{(k)} = \mathbf{D}\boldsymbol{\Delta}^{(k)} = \mathbf{D}_\zeta \mathbf{D}_\Omega \boldsymbol{\Delta}^{(k)} \Leftrightarrow \begin{bmatrix} \boldsymbol{\varepsilon}^{(k)} \\ \mathscr{E}^{(k)} \\ \widehat{\Delta\mathrm{T}}^{(k)} \\ \boldsymbol{\theta}^{(k)} \end{bmatrix} = \begin{bmatrix} \mathbf{D}_{(1)} & \mathbf{0} & \mathbf{0} \\ \mathbf{0} & \mathbf{D}_{(2)} & \mathbf{0} \\ \mathbf{0} & \mathbf{0} & \mathbf{D}_{(3)} \\ \mathbf{0} & \mathbf{0} & \mathbf{D}_{(2)} \end{bmatrix} \begin{bmatrix} \mathbf{U}^{(k)} \\ \Delta\phi^{(k)} \\ \Delta\mathrm{T}^{(k)} \end{bmatrix} \tag{14}$$

In particular, $\mathbf{D}$ is derived from the definitions of sub-operators $\mathbf{D}_{(1)}$ and $\mathbf{D}_{(2)}$, which represent the symmetric part of the three-dimensional strain gradient operator and the gradient operator of a scalar field, respectively. It is also, $\mathbf{D}_{(3)} = 1$.

As can be seen, $\mathbf{D}$ is expressed as the product of operators $\mathbf{D}_\Omega$ and $\mathbf{D}_\zeta$, which account for derivatives along coordinates α_1,α_2 and ζ, respectively. More specifically, $\mathbf{D}_\Omega$ and $\mathbf{D}_\zeta$ take the following extended form:

$$\mathbf{D}_\Omega = \begin{bmatrix} \mathbf{D}_{\Omega(1)} & \mathbf{0} & \mathbf{0} \\ \mathbf{0} & \mathbf{D}_{\Omega(2)} & \mathbf{0} \\ \mathbf{0} & \mathbf{0} & \mathbf{D}_{\Omega(3)} \\ \mathbf{0} & \mathbf{0} & \mathbf{D}_{\Omega(2)} \end{bmatrix}, \quad \mathbf{D}_\zeta = \begin{bmatrix} \mathbf{D}_{\zeta(1)} & \mathbf{0} & \mathbf{0} & \mathbf{0} \\ \mathbf{0} & \mathbf{D}_{\zeta(2)} & \mathbf{0} & \mathbf{0} \\ \mathbf{0} & \mathbf{0} & \mathbf{D}_{\zeta(3)} & \mathbf{0} \\ \mathbf{0} & \mathbf{0} & \mathbf{0} & \mathbf{D}_{\zeta(2)} \end{bmatrix} \tag{15}$$

The sub-operators $\mathbf{D}_{\Omega(1)}, \mathbf{D}_{\Omega(2)}$ and $\mathbf{D}_{\Omega(3)}$ are defined as follows:

$$\begin{aligned} \mathbf{D}_{\Omega(1)} &= \begin{bmatrix} \overline{\mathbf{D}}_\Omega^{\alpha_1} & \overline{\mathbf{D}}_\Omega^{\alpha_2} & \overline{\mathbf{D}}_\Omega^{\alpha_3} \end{bmatrix} \\ \mathbf{D}_{\Omega(2)} &= \begin{bmatrix} -\dfrac{1}{A_1}\dfrac{\partial}{\partial\alpha_1} & -\dfrac{1}{A_2}\dfrac{\partial}{\partial\alpha_2} & -1 \end{bmatrix}^T \\ \mathbf{D}_{\Omega(3)} &= 1 \end{aligned} \tag{16}$$

while the sub-operators $\overline{\mathbf{D}}_\Omega^{\alpha_1}, \overline{\mathbf{D}}_\Omega^{\alpha_2}, \overline{\mathbf{D}}_\Omega^{\alpha_3}$ assume the following extended form:

$$\begin{gathered}
\overline{\mathbf{D}}_{\Omega}^{\alpha_1}=\left[\frac{1}{A_1}\frac{\partial}{\partial\alpha_1}\quad \frac{1}{A_1A_2}\frac{\partial A_2}{\partial\alpha_1}\quad -\frac{1}{A_1A_2}\frac{\partial A_1}{\partial\alpha_2}\quad \frac{1}{A_2}\frac{\partial}{\partial\alpha_2}\quad -\frac{1}{R_1}\quad 0\quad 1\quad 0\quad 0\right]^T\\
\overline{\mathbf{D}}_{\Omega}^{\alpha_2}=\left[\frac{1}{A_1A_2}\frac{\partial A_1}{\partial\alpha_2}\quad \frac{1}{A_2}\frac{\partial}{\partial\alpha_2}\quad \frac{1}{A_1}\frac{\partial}{\partial\alpha_1}\quad -\frac{1}{A_1A_2}\frac{\partial A_2}{\partial\alpha_1}\quad 0\quad -\frac{1}{R_2}\quad 0\quad 1\quad 0\right]^T\\
\overline{\mathbf{D}}_{\Omega}^{\alpha_3}=\left[\frac{1}{R_1}\quad \frac{1}{R_2}\quad 0\quad 0\quad \frac{1}{A_1}\frac{\partial}{\partial\alpha_1}\quad \frac{1}{A_2}\frac{\partial}{\partial\alpha_2}\quad 0\quad 0\quad 1\right]^T
\end{gathered}\tag{17}$$

The matrices $\mathbf{D}_{\zeta(1)},\mathbf{D}_{\zeta(2)}$ and $\mathbf{D}_{\zeta(3)}$ are defined as follows:

$$\mathbf{D}_{\zeta(1)}=\begin{bmatrix}
\frac{1}{H_1} & 0 & 0 & 0 & 0 & 0 & 0 & 0 & 0\\
0 & \frac{1}{H_2} & 0 & 0 & 0 & 0 & 0 & 0 & 0\\
0 & 0 & \frac{1}{H_1} & \frac{1}{H_2} & 0 & 0 & 0 & 0 & 0\\
0 & 0 & 0 & 0 & \frac{1}{H_1} & 0 & \frac{\partial}{\partial\zeta} & 0 & 0\\
0 & 0 & 0 & 0 & 0 & \frac{1}{H_2} & 0 & \frac{\partial}{\partial\zeta} & 0\\
0 & 0 & 0 & 0 & 0 & 0 & 0 & 0 & \frac{\partial}{\partial\zeta}
\end{bmatrix},\quad \mathbf{D}_{\zeta(2)}=\begin{bmatrix}
\frac{1}{H_1} & 0 & 0\\
0 & \frac{1}{H_2} & 0\\
0 & 0 & \frac{\partial}{\partial\zeta}
\end{bmatrix},\quad \mathbf{D}_{\zeta(3)}=1\tag{18}$$

being H_1,H_2 the geometric scaling parameters. It is convenient to express the kinematic operator $\mathbf{D}_{\Omega}$ of Eqn. (15) as the sum of the definition operators $\mathbf{D}_{\Omega}^{\alpha_i}$ associated to each unknown variable of the formulation, which means:

$$\mathbf{D}_{\Omega}=\sum_{i=1}^{5}\mathbf{D}_{\Omega}^{\alpha_i}\tag{19}$$

where the definition operators $\mathbf{D}_{\Omega}^{\alpha_i}$ with $i=1,\ldots,5$ are reported below, setting $\overline{\mathbf{D}}_{\Omega(2)}^{\alpha_4}=\overline{\mathbf{D}}_{\Omega(2)}^{\alpha_5}=\mathbf{D}_{\Omega(2)}$ and $\widetilde{\mathbf{D}}_{\Omega(2)}^{\alpha_5}=\mathbf{D}_{\Omega(3)}$:

$$\begin{gathered}
\mathbf{D}_{\Omega}^{\alpha_1}=\begin{bmatrix}
\overline{\mathbf{D}}_{\Omega}^{\alpha_1} & \mathbf{0} & \mathbf{0} & \mathbf{0} & \mathbf{0}\\
\mathbf{0} & \mathbf{0} & \mathbf{0} & \mathbf{0} & \mathbf{0}\\
\mathbf{0} & \mathbf{0} & \mathbf{0} & \mathbf{0} & \mathbf{0}\\
\mathbf{0} & \mathbf{0} & \mathbf{0} & \mathbf{0} & \mathbf{0}
\end{bmatrix},\quad
\mathbf{D}_{\Omega}^{\alpha_2}=\begin{bmatrix}
\mathbf{0} & \overline{\mathbf{D}}_{\Omega}^{\alpha_2} & \mathbf{0} & \mathbf{0} & \mathbf{0}\\
\mathbf{0} & \mathbf{0} & \mathbf{0} & \mathbf{0} & \mathbf{0}\\
\mathbf{0} & \mathbf{0} & \mathbf{0} & \mathbf{0} & \mathbf{0}\\
\mathbf{0} & \mathbf{0} & \mathbf{0} & \mathbf{0} & \mathbf{0}
\end{bmatrix},\quad
\mathbf{D}_{\Omega}^{\alpha_3}=\begin{bmatrix}
\mathbf{0} & \mathbf{0} & \overline{\mathbf{D}}_{\Omega}^{\alpha_3} & \mathbf{0} & \mathbf{0}\\
\mathbf{0} & \mathbf{0} & \mathbf{0} & \mathbf{0} & \mathbf{0}\\
\mathbf{0} & \mathbf{0} & \mathbf{0} & \mathbf{0} & \mathbf{0}\\
\mathbf{0} & \mathbf{0} & \mathbf{0} & \mathbf{0} & \mathbf{0}
\end{bmatrix},\\
\mathbf{D}_{\Omega}^{\alpha_4}=\begin{bmatrix}
\mathbf{0} & \mathbf{0} & \mathbf{0} & \mathbf{0} & \mathbf{0}\\
\mathbf{0} & \mathbf{0} & \mathbf{0} & \overline{\mathbf{D}}_{\Omega}^{\alpha_4} & \mathbf{0}\\
\mathbf{0} & \mathbf{0} & \mathbf{0} & \mathbf{0} & \mathbf{0}\\
\mathbf{0} & \mathbf{0} & \mathbf{0} & \mathbf{0} & \mathbf{0}
\end{bmatrix},\quad
\mathbf{D}_{\Omega}^{\alpha_5}=\begin{bmatrix}
\mathbf{0} & \mathbf{0} & \mathbf{0} & \mathbf{0} & \mathbf{0}\\
\mathbf{0} & \mathbf{0} & \mathbf{0} & \mathbf{0} & \mathbf{0}\\
\mathbf{0} & \mathbf{0} & \mathbf{0} & \mathbf{0} & \widetilde{\mathbf{D}}_{\Omega}^{\alpha_5}\\
\mathbf{0} & \mathbf{0} & \mathbf{0} & \mathbf{0} & \overline{\mathbf{D}}_{\Omega}^{\alpha_5}
\end{bmatrix}
\end{gathered}\tag{20}$$

Employing the generalized expansion of the kinematic model in Eqn. (9), the three-dimensional multifield definition equations (14) can be expressed in terms of higher-order theories as follows, with $\mathbf{Z}^{(k\tau)\alpha_i}=\mathbf{D}_{\zeta}F_{\tau}^{(k)\alpha_i}$ and $\boldsymbol{\pi}^{(\tau)\alpha_i}=\mathbf{D}_{\Omega}^{\alpha_i}\boldsymbol{\delta}^{(\tau)}$ representing the kinematic operator and the generalized primary variables vector, respectively, for any given $\tau=0,\ldots,N+1$ and $i=1,\ldots,5$:

$$\boldsymbol{\pi}^{(k)}=\sum_{\tau=0}^{N+1}\sum_{i=1}^{5}\mathbf{Z}^{(k\tau)\alpha_i}\boldsymbol{\pi}^{(\tau)\alpha_i}\tag{21}$$

In this way, each vector $\boldsymbol{\varepsilon}^{(k)}$, $\mathscr{E}^{(k)}$, $\widehat{\Delta\mathrm{T}}^{(k)}$, $\boldsymbol{\theta}^{(k)}$ of three-dimensional primary variables can be expanded using its corresponding generalized vector $\boldsymbol{\varepsilon}^{(\tau)\alpha_i}$, $\mathscr{E}^{(\tau)\alpha_i}$, $\widehat{\Delta\mathrm{T}}^{(\tau)\alpha_i}$, $\boldsymbol{\theta}^{(\tau)\alpha_i}$ as follows:

$$\begin{bmatrix}\boldsymbol{\varepsilon}^{(k)}\\ \mathscr{E}^{(k)}\\ \widehat{\Delta\mathrm{T}}^{(k)}\\ \boldsymbol{\theta}^{(k)}\end{bmatrix}=\sum_{\tau=0}^{N+1}\sum_{i=1}^{5}\begin{bmatrix}
\mathbf{Z}_1^{(k\tau)\alpha_i} & \mathbf{0} & \mathbf{0} & \mathbf{0}\\
\mathbf{0} & \mathbf{Z}_2^{(k\tau)\alpha_i} & \mathbf{0} & \mathbf{0}\\
\mathbf{0} & \mathbf{0} & \mathbf{Z}_3^{(k\tau)\alpha_i} & \mathbf{0}\\
\mathbf{0} & \mathbf{0} & \mathbf{0} & \mathbf{Z}_2^{(k\tau)\alpha_i}
\end{bmatrix}\begin{bmatrix}\boldsymbol{\varepsilon}^{(\tau)\alpha_i}\\ \mathscr{E}^{(\tau)\alpha_i}\\ \widehat{\Delta\mathrm{T}}^{(\tau)\alpha_i}\\ \boldsymbol{\theta}^{(\tau)\alpha_i}\end{bmatrix}\tag{22}$$

where the generalized sub-operator $\mathbf{Z}_m^{(k\tau)\alpha_i}=\mathbf{D}_{\zeta(m)}F_{\tau}^{(k)\alpha_i}$ with $m=1,2,3$ is defined by applying the kinematic operator $\mathbf{D}_{\zeta(m)}$ from Eqn. (18) to the thickness function $F_{\tau}^{(k)\alpha_i}$. Finally, it should be noted that the generalized primary variable vectors are defined for the entire lamination scheme and, therefore, do not depend on the thickness coordinate ζ. They are expressed in the following extended form:

$$\begin{gathered}
\boldsymbol{\varepsilon}^{(\tau)\alpha_i}(\alpha_1,\alpha_2)=\left[\varepsilon_1^{(\tau)\alpha_i}\quad \varepsilon_2^{(\tau)\alpha_i}\quad \gamma_1^{(\tau)\alpha_i}\quad \gamma_2^{(\tau)\alpha_i}\quad \gamma_{13}^{(\tau)\alpha_i}\quad \gamma_{23}^{(\tau)\alpha_i}\quad \omega_{13}^{(\tau)\alpha_i}\quad \omega_{23}^{(\tau)\alpha_i}\quad \varepsilon_3^{(\tau)\alpha_i}\right]^T\\
\mathscr{E}^{(\tau)\alpha_i}(\alpha_1,\alpha_2)=\left[\mathscr{E}_1^{(\tau)\alpha_i}\quad \mathscr{E}_2^{(\tau)\alpha_i}\quad \mathscr{E}_3^{(\tau)\alpha_i}\right]^T\\
\widehat{\Delta\mathrm{T}}^{(\tau)\alpha_i}(\alpha_1,\alpha_2)=\widehat{\Delta\mathrm{T}}^{(\tau)\alpha_i},\quad \boldsymbol{\theta}^{(\tau)\alpha_i}(\alpha_1,\alpha_2)=\left[\theta_1^{(\tau)\alpha_i}\quad \theta_2^{(\tau)\alpha_i}\quad \theta_3^{(\tau)\alpha_i}\right]^T
\end{gathered}\tag{23}$$

The multifield constitutive relation is determined by defining, within each k−th lamina of the stacking sequence, the three-dimensional constitutive matrix $\overline{\boldsymbol{\Gamma}}^{(k)}$, defined in the geometric curvilinear reference system α_1,α_2,ζ. This matrix relates vector $\boldsymbol{\pi}^{(k)}$ of primary variables, as defined in Eqn. (14), to vector $\boldsymbol{\chi}^{(k)}$ of secondary variables. The interaction between the thermal, electrical, and mechanical physical problems can be easily seen from the following relation:

$$\boldsymbol{\chi}^{(k)}=\overline{\boldsymbol{\Gamma}}^{(k)}\boldsymbol{\pi}^{(k)}\quad\Leftrightarrow\quad\begin{bmatrix}\boldsymbol{\sigma}^{(k)}\\ \mathscr{D}^{(k)}\\ \eta^{(k)}\\ \mathbf{h}^{(k)}\end{bmatrix}=\begin{bmatrix}
\overline{\boldsymbol{\Gamma}}_{\mathrm{C}}^{(k)} & -\overline{\boldsymbol{\Gamma}}_{\mathrm{P}}^{(k)T} & -\overline{\boldsymbol{\Gamma}}_{\mathrm{z}}^{(k)T} & \mathbf{0}\\
\overline{\boldsymbol{\Gamma}}_{\mathrm{P}}^{(k)} & \overline{\boldsymbol{\Gamma}}_{\mathrm{L}}^{(k)} & \overline{\boldsymbol{\Gamma}}_{\mathrm{o}}^{(k)T} & \mathbf{0}\\
\overline{\boldsymbol{\Gamma}}_{\mathrm{z}}^{(k)} & \overline{\boldsymbol{\Gamma}}_{\mathrm{o}}^{(k)} & \overline{\Gamma}_{\mathrm{TT}}^{(k)} & \mathbf{0}\\
\mathbf{0} & \mathbf{0} & \mathbf{0} & \overline{\boldsymbol{\Gamma}}_{\mathrm{K}}^{(k)}
\end{bmatrix}\begin{bmatrix}\boldsymbol{\varepsilon}^{(k)}\\ \mathscr{E}^{(k)}\\ \widehat{\Delta\mathrm{T}}^{(k)}\\ \boldsymbol{\theta}^{(k)}\end{bmatrix}\tag{24}$$

Vectors of secondary variables in Eqn. (24) refer to the three-dimensional stress field $\boldsymbol{\sigma}^{(k)}=\left[\sigma_1^{(k)}\quad \sigma_2^{(k)}\quad \tau_{12}^{(k)}\quad \tau_{13}^{(k)}\quad \tau_{23}^{(k)}\quad \sigma_3^{(k)}\right]^T$, the electric displacement $\mathscr{D}^{(k)}=\left[\mathscr{D}_1^{(k)}\quad \mathscr{D}_2^{(k)}\quad \mathscr{D}_3^{(k)}\right]^T$, and the thermal

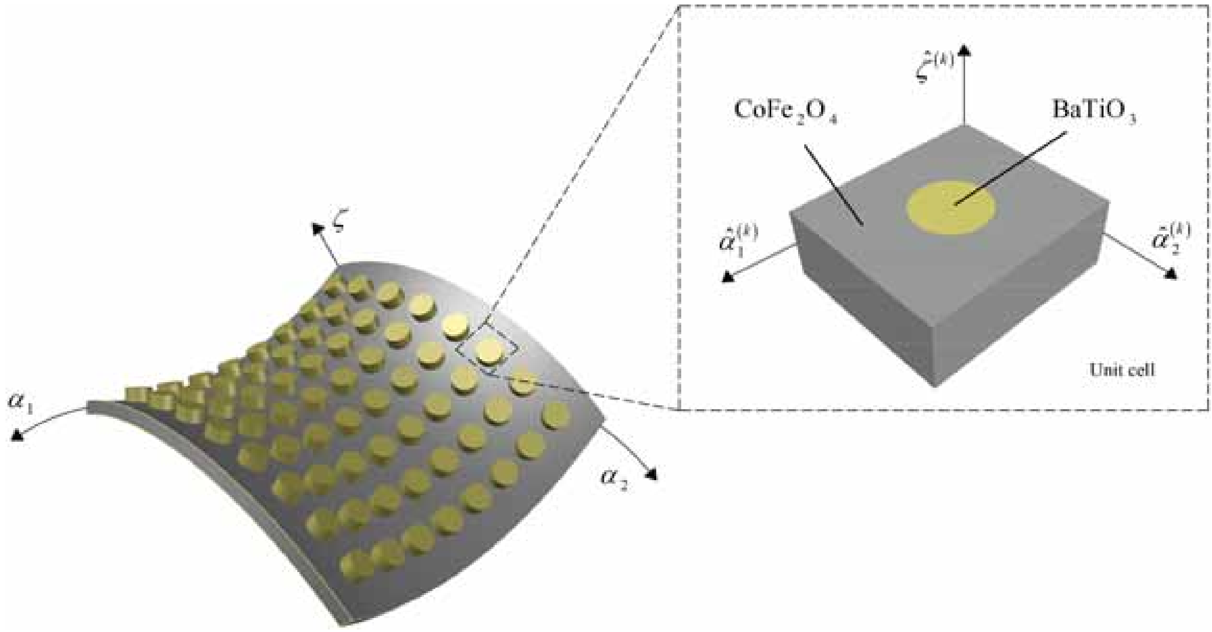

Fig. 1. Representation of a doubly-curved shell panel made of smart ETE materials. Individuation of the unit cell for the homogenization of the multifield properties.

flux $\mathbf{h}^{(k)} = \begin{bmatrix} h_1^{(k)} & h_2^{(k)} & h_3^{(k)} \end{bmatrix}^T$. Finally, $\eta^{(k)}$ represents the specific entropy. The three-dimensional constitutive relation applies to generally anisotropic materials, considering all possible coupling effects between mechanical elasticity, electrostatics, and thermal conduction. More specifically, $\overline{\boldsymbol{\Gamma}}_{\mathrm{C}}^{(k)}$ represents the mechanical stiffness matrix, while $\overline{\boldsymbol{\Gamma}}_{\mathrm{P}}^{(k)}$ accounts for direct and inverse piezoelectric effects. The dielectric matrix is denoted by $\overline{\boldsymbol{\Gamma}}_{\mathrm{L}}^{(k)}$, where $\overline{\boldsymbol{\Gamma}}_{\mathrm{K}}^{(k)}$ represents the thermal conductivity matrix of the solid. Furthermore, $\overline{\boldsymbol{\Gamma}}_{\mathrm{z}}^{(k)}$ and $\overline{\boldsymbol{\Gamma}}_{\mathrm{o}}^{(k)}$ are used to model the thermal expansion and pyroelectricity, respectively, while $\overline{\boldsymbol{\Gamma}}_{\mathrm{TT}}^{(k)}$ relates the absolute temperature variation to the change in the specific entropy within the solid. The submatrices in Eqn. (24) are given by [38]:

$$\overline{\boldsymbol{\Gamma}}_{\mathrm{C}}^{(k)} = \begin{bmatrix} \overline{C}_{11}^{(k)} & \overline{C}_{12}^{(k)} & \overline{C}_{16}^{(k)} & \overline{C}_{14}^{(k)} & \overline{C}_{15}^{(k)} & \overline{C}_{13}^{(k)} \\ \overline{C}_{12}^{(k)} & \overline{C}_{22}^{(k)} & \overline{C}_{26}^{(k)} & \overline{C}_{24}^{(k)} & \overline{C}_{25}^{(k)} & \overline{C}_{23}^{(k)} \\ \overline{C}_{16}^{(k)} & \overline{C}_{26}^{(k)} & \overline{C}_{66}^{(k)} & \overline{C}_{46}^{(k)} & \overline{C}_{56}^{(k)} & \overline{C}_{36}^{(k)} \\ \overline{C}_{14}^{(k)} & \overline{C}_{24}^{(k)} & \overline{C}_{46}^{(k)} & \overline{C}_{44}^{(k)} & \overline{C}_{45}^{(k)} & \overline{C}_{34}^{(k)} \\ \overline{C}_{15}^{(k)} & \overline{C}_{25}^{(k)} & \overline{C}_{56}^{(k)} & \overline{C}_{45}^{(k)} & \overline{C}_{55}^{(k)} & \overline{C}_{35}^{(k)} \\ \overline{C}_{13}^{(k)} & \overline{C}_{23}^{(k)} & \overline{C}_{36}^{(k)} & \overline{C}_{34}^{(k)} & \overline{C}_{35}^{(k)} & \overline{C}_{33}^{(k)} \end{bmatrix}, \quad \overline{\boldsymbol{\Gamma}}_{\mathrm{L}}^{(k)} = \begin{bmatrix} \overline{l}_{11}^{(k)} & \overline{l}_{12}^{(k)} & \overline{l}_{13}^{(k)} \\ \overline{l}_{12}^{(k)} & \overline{l}_{22}^{(k)} & \overline{l}_{23}^{(k)} \\ \overline{l}_{13}^{(k)} & \overline{l}_{23}^{(k)} & \overline{l}_{33}^{(k)} \end{bmatrix}, \quad \overline{\boldsymbol{\Gamma}}_{\mathrm{K}}^{(k)} = \begin{bmatrix} \overline{k}_{11}^{(k)} & \overline{k}_{12}^{(k)} & \overline{k}_{13}^{(k)} \\ \overline{k}_{12}^{(k)} & \overline{k}_{22}^{(k)} & \overline{k}_{23}^{(k)} \\ \overline{k}_{13}^{(k)} & \overline{k}_{23}^{(k)} & \overline{k}_{33}^{(k)} \end{bmatrix}$$

$$\overline{\boldsymbol{\Gamma}}_{\mathrm{P}}^{(k)} = \begin{bmatrix} \overline{p}_{11}^{(k)} & \overline{p}_{12}^{(k)} & \overline{p}_{16}^{(k)} & \overline{p}_{14}^{(k)} & \overline{p}_{15}^{(k)} & \overline{p}_{13}^{(k)} \\ \overline{p}_{21}^{(k)} & \overline{p}_{22}^{(k)} & \overline{p}_{26}^{(k)} & \overline{p}_{24}^{(k)} & \overline{p}_{25}^{(k)} & \overline{p}_{23}^{(k)} \\ \overline{p}_{31}^{(k)} & \overline{p}_{32}^{(k)} & \overline{p}_{36}^{(k)} & \overline{p}_{34}^{(k)} & \overline{p}_{35}^{(k)} & \overline{p}_{33}^{(k)} \end{bmatrix}, \quad \overline{\boldsymbol{\Gamma}}_{\mathrm{z}}^{(k)} = \begin{bmatrix} \overline{z}_{11}^{(k)} & \overline{z}_{22}^{(k)} & \overline{z}_{12}^{(k)} & \overline{z}_{13}^{(k)} & \overline{z}_{23}^{(k)} & \overline{z}_{33}^{(k)} \end{bmatrix}$$

$$\overline{\boldsymbol{\Gamma}}_{\mathrm{o}}^{(k)} = \begin{bmatrix} \overline{o}_{11}^{(k)} & \overline{o}_{22}^{(k)} & \overline{o}_{33}^{(k)} \end{bmatrix}, \quad \overline{\boldsymbol{\Gamma}}_{\mathrm{KK}}^{(k)} = \overline{\xi}_{11}^{(k)} = \frac{\rho^{(k)} c_p^{(k)}}{\mathrm{T}_0} \tag{25}$$

The term $\overline{\xi}_{11}^{(k)}$ is defined at each point of the three-dimensional solid in terms of material density $\rho^{(k)}$ and specific heat $c_p^{(k)}$ at a given reference absolute temperature T_0. In this contribution, the value $\mathrm{T}_0 = 297\,\mathrm{K}$ is considered. It is useful to express the three-dimensional constitutive relation (24) in the material reference system, denoted by $O'\widehat{\alpha}_1^{(k)}\widehat{\alpha}_2^{(k)}\widehat{\zeta}^{(k)}$, which is defined based on the symmetry axes of the constituent material in each k–th layer. The following notation is, thus, introduced:

$$\widehat{\boldsymbol{\chi}}^{(k)} = \boldsymbol{\Gamma}^{(k)}\widehat{\boldsymbol{\pi}}^{(k)} \Leftrightarrow \begin{bmatrix} \widehat{\boldsymbol{\sigma}}^{(k)} \\ \widehat{\mathscr{D}}^{(k)} \\ \eta^{(k)} \\ \widehat{\mathbf{h}}^{(k)} \end{bmatrix} = \begin{bmatrix} \boldsymbol{\Gamma}_{\mathrm{C}}^{(k)} & -\boldsymbol{\Gamma}_{\mathrm{P}}^{(k)T} & -\boldsymbol{\Gamma}_{\mathrm{z}}^{(k)T} & \mathbf{0} \\ \boldsymbol{\Gamma}_{\mathrm{P}}^{(k)} & \boldsymbol{\Gamma}_{\mathrm{L}}^{(k)} & \boldsymbol{\Gamma}_{\mathrm{o}}^{(k)T} & \mathbf{0} \\ \boldsymbol{\Gamma}_{\mathrm{z}}^{(k)} & \boldsymbol{\Gamma}_{\mathrm{o}}^{(k)} & \boldsymbol{\Gamma}_{\mathrm{TT}}^{(k)} & \mathbf{0} \\ \mathbf{0} & \mathbf{0} & \mathbf{0} & \boldsymbol{\Gamma}_{\mathrm{K}}^{(k)} \end{bmatrix} \begin{bmatrix} \widehat{\boldsymbol{\varepsilon}}^{(k)} \\ \widehat{\mathscr{E}}^{(k)} \\ \Delta\mathrm{T}^{(k)} \\ \widehat{\boldsymbol{\theta}}^{(k)} \end{bmatrix} \tag{26}$$

Matrix $\overline{\boldsymbol{\Gamma}}_{\mathrm{z}}^{(k)}$ of thermal expansion is defined as $\overline{\boldsymbol{\Gamma}}_{\mathrm{z}}^{(k)T} = \overline{\boldsymbol{\Gamma}}_{\mathrm{C}}^{(k)}\overline{\boldsymbol{\Gamma}}_{\mathrm{a}}^{(k)}$, where the vector $\overline{\boldsymbol{\Gamma}}_{\mathrm{a}}^{(k)} = \begin{bmatrix} a_{11}^{(k)} & a_{22}^{(k)} & a_{12}^{(k)} & a_{13}^{(k)} & a_{23}^{(k)} & a_{33}^{(k)} \end{bmatrix}^T$ contains the elements of the rotated matrix $\overline{\boldsymbol{A}}^{(k)}$, which is defined using the well-known Hadamard product $\odot$ as follows:

$$\overline{\boldsymbol{A}}^{(k)} = \boldsymbol{Y}_{\varepsilon} \odot \left(\boldsymbol{H}^{(k)T}\widehat{\mathbf{A}}^{(k)}\boldsymbol{H}^{(k)}\right) \tag{27}$$

Matrix $\boldsymbol{Y}_{\varepsilon}$ enables the expression of the rotated thermal expansion coefficients $\overline{a}_{ij}^{(k)}$ with $i,j = 1,2,3$, for engineering strain components, starting from coefficients collected in matrix $\widehat{\boldsymbol{A}}^{(k)}$ and denoted by $\widehat{a}_{ij}^{(k)}$ with $i,j = 1,2,3$, which are associated with the elements of the three-dimensional strain tensor:

$$\boldsymbol{A}^{(k)} = \begin{bmatrix} a_{11}^{(k)} & a_{12}^{(k)} & a_{13}^{(k)} \\ a_{12}^{(k)} & a_{22}^{(k)} & a_{23}^{(k)} \\ a_{13}^{(k)} & a_{23}^{(k)} & a_{33}^{(k)} \end{bmatrix} = \begin{bmatrix} 1 & 2 & 2 \\ 2 & 1 & 2 \\ 2 & 2 & 1 \end{bmatrix} \odot \begin{bmatrix} \widehat{a}_{11}^{(k)} & \widehat{a}_{12}^{(k)} & \widehat{a}_{13}^{(k)} \\ \widehat{a}_{12}^{(k)} & \widehat{a}_{22}^{(k)} & \widehat{a}_{23}^{(k)} \\ \widehat{a}_{13}^{(k)} & \widehat{a}_{23}^{(k)} & \widehat{a}_{33}^{(k)} \end{bmatrix} = \boldsymbol{Y}_{\varepsilon} \odot \widehat{\boldsymbol{A}}^{(k)} \tag{28}$$

$\boldsymbol{A}^{(k)}$ being the thermal expansion coefficient matrix expressed in the material reference system.

Referring to Eqn. (26), $\widehat{\boldsymbol{\pi}}^{(k)}$ and $\widehat{\boldsymbol{\chi}}^{(k)}$ represent the vectors of primary and secondary variables, respectively, in the material reference system. Eqn. (26) is used to derive the corresponding constitutive relation in the geometric reference system by rotating the three-dimensional multifield constitutive matrix. This yields the following relation [38]:

$$\overline{\boldsymbol{\Gamma}}^{(k)} = \begin{bmatrix} \boldsymbol{T}^{(k)}\boldsymbol{\Gamma}_{\mathrm{C}}^{(k)}\boldsymbol{T}^{(k)T} & -\boldsymbol{T}^{(k)}\boldsymbol{\Gamma}_{\mathrm{P}}^{(k)T}\boldsymbol{H}^{(k)} & -\mathbf{T}^{(k)}\boldsymbol{\Gamma}_{\mathrm{C}}^{(k)}\mathbf{T}^{(k)T}\boldsymbol{\Gamma}_{\mathrm{a}}^{(k)} & \mathbf{0} \\ \boldsymbol{H}^{(k)T}\boldsymbol{\Gamma}_{\mathrm{P}}^{(k)}\boldsymbol{T}^{(k)T} & \boldsymbol{H}^{(k)T}\boldsymbol{\Gamma}_{\mathrm{L}}^{(k)}\boldsymbol{H}^{(k)} & \boldsymbol{H}^{(k)T}\boldsymbol{\Gamma}_{\mathrm{o}}^{(k)T} & \mathbf{0} \\ \boldsymbol{\Gamma}_{\mathrm{a}}^{(k)T}\mathbf{T}^{(k)T}\boldsymbol{\Gamma}_{\mathrm{C}}^{(k)}\mathbf{T}^{(k)} & \boldsymbol{\Gamma}_{\mathrm{o}}^{(k)}\boldsymbol{H}^{(k)} & \Gamma_{\mathrm{TT}}^{(k)} & 0 \\ \mathbf{0} & \mathbf{0} & 0 & \boldsymbol{H}^{(k)T}\boldsymbol{\Gamma}_{\mathrm{K}}^{(k)}\boldsymbol{H}^{(k)} \end{bmatrix} \tag{29}$$

As can be seen, matrix $\overline{\boldsymbol{\Gamma}}^{(k)}$ is derived from $\boldsymbol{\Gamma}^{(k)}$ by applying the rotation transformations to its sub-matrices. These are defined in terms of the rotation matrices $\boldsymbol{H}^{(k)}$ and $\boldsymbol{T}^{(k)}$ of sizes 3×3 and 6×6, respectively. In this work, it is assumed that the material axis $\widehat{\zeta}^{(k)}$ is always parallel to the outward normal direction of the shell (Fig. 1), namely $\widehat{\zeta}^{(k)} = \zeta^{(k)}$. In this way, $\boldsymbol{H}^{(k)}, \boldsymbol{T}^{(k)}$ depend on the angle $\vartheta^{(k)}$ between the axes $\widehat{\alpha}_1^{(k)}$ and α_1, and take the following form, setting $\otimes$ the Kronecker product:

$$\boldsymbol{H}^{(k)} = \begin{bmatrix} \cos\vartheta^{(k)} & \sin\vartheta^{(k)} & 0 \\ -\sin\vartheta^{(k)} & \cos\vartheta^{(k)} & 0 \\ 0 & 0 & 1 \end{bmatrix}$$

$$\begin{aligned} \boldsymbol{T}^{(k)} &= \overline{\boldsymbol{T}}^{(k)}_{([1,5,4,7,8,9]\times[1,5,2+4,3+7,6+8,9])} \\ &= \left(\boldsymbol{H}^{(k)T}\otimes\left(\boldsymbol{H}^{(k)}\right)^{-1}\right)_{([1,5,4,7,8,9]\times[1,5,2+4,3+7,6+8,9])} \end{aligned} \tag{30}$$

The higher-order constitutive relationship is now derived within the ESL framework, starting from the three-dimensional multifield relation in Eqn. (24). To achieve this, the virtual variation $\delta\Upsilon$ of the total energy of the doubly-curved shell solid is computed using the curvilinear principal coordinates, taking into account all possible coupling effects between multifield primary and secondary variables related to the mechanical elasticity, electrostatic and thermal conduction. It is convenient to introduce the modified vector of three-dimensional primary variables $\overline{\boldsymbol{\pi}}^{(k)T} = \left[\boldsymbol{\varepsilon}^{(k)T} \quad -\mathscr{E}^{(k)T} \quad -\widehat{\Delta}\mathrm{T}^{(k)} \quad \boldsymbol{\theta}^{(k)T}\right]^T$, as well as the modified vector of three-dimensional multifield secondary variables, denoted by $\overline{\boldsymbol{\chi}}^{(k)}$:

$$\begin{bmatrix} \boldsymbol{\sigma}^{(k)} \\ \mathscr{D}^{(k)} \\ \eta^{(k)} \\ \mathbf{h}^{(k)} \end{bmatrix} = \begin{bmatrix} \widehat{\mathbf{I}} & \mathbf{0} & \mathbf{0} & \mathbf{0} \\ \mathbf{0} & \mathbf{I} & \mathbf{0} & \mathbf{0} \\ \mathbf{0} & \mathbf{0} & 1 & \mathbf{0} \\ \mathbf{0} & \mathbf{0} & \mathbf{0} & \dfrac{1}{\mathrm{T}_0}\mathbf{I} \end{bmatrix} \begin{bmatrix} \boldsymbol{\sigma}^{(k)} \\ \mathscr{D}^{(k)} \\ \eta^{(k)} \\ \mathbf{h}^{(k)} \end{bmatrix} \Leftrightarrow \overline{\boldsymbol{\chi}}^{(k)} = \mathbf{B}\boldsymbol{\chi}^{(k)} \tag{31}$$

Here, $\widehat{\boldsymbol{I}}$ and $\boldsymbol{I}$ denote the identity matrices of sizes 6×6 and 3×3, respectively. In this way, the virtual variation of the total energy Υ of the shell is computed as [38]:

$$\begin{aligned} \delta\Upsilon &= \sum_{k=1}^{l}\int_{\alpha_1}\int_{\alpha_2}\int_{\zeta_k}^{\zeta_{k+1}}\left(\delta\overline{\boldsymbol{\pi}}^{(k)T}\overline{\boldsymbol{\chi}}^{(k)}\right)A_1A_2H_1H_2\,d\alpha_1 d\alpha_2 d\zeta = \\ &= \sum_{k=1}^{l}\int_{\alpha_1}\int_{\alpha_2}\int_{\zeta_k}^{\zeta_{k+1}}\left(\delta\boldsymbol{\varepsilon}^{(k)T}\boldsymbol{\sigma}^{(k)} - \delta\mathscr{E}^{(k)T}\mathscr{D}^{(k)} - \delta\widehat{\Delta}\mathrm{T}^{(k)}\eta^{(k)} - \delta\boldsymbol{\theta}^{(k)T}\frac{\mathbf{h}^{(k)}}{\mathrm{T}_0}\right)A_1A_2H_1H_2\,d\alpha_1 d\alpha_2 d\zeta \end{aligned} \tag{32}$$

The virtual variations $\delta\boldsymbol{\varepsilon}^{(k)T}, \delta\mathscr{E}^{(k)T}, \delta\widehat{\Delta}\mathrm{T}^{(k)}, \delta\boldsymbol{\theta}^{(k)T}$ of thermo-electro-mechanical primary variables are expressed using Eqs. (22) in terms of the virtual variations $\delta\boldsymbol{\varepsilon}^{(\tau)\alpha_i T}, \delta\mathscr{E}^{(\tau)\alpha_i T}, \delta\widehat{\Delta}\mathrm{T}^{(\tau)\alpha_i}, \delta\boldsymbol{\theta}^{(\tau)\alpha_i T}$ of the generalized primary variables. As a consequence, Eqn. (32) becomes:

$$\begin{aligned} \delta\Upsilon &= \sum_{k=1}^{l}\int_{\alpha_1}\int_{\alpha_2}\int_{\zeta_k}^{\zeta_{k+1}}\left(\sum_{\tau=0}^{N+1}\sum_{i=1}^{5}\mathbf{Z}^{(k\tau)\alpha_i}\delta\overline{\boldsymbol{\pi}}^{(\tau)\alpha_i}\right)^T\boldsymbol{\chi}^{(k)}A_1A_2H_1H_2\,d\zeta\, d\alpha_1 d\alpha_2 = \\ &= \sum_{\tau=0}^{N+1}\sum_{i=1}^{5}\int_{\alpha_1}\int_{\alpha_2}\left(\delta\overline{\boldsymbol{\pi}}^{(\tau)\alpha_i}\right)^T\left(\sum_{k=1}^{l}\int_{\zeta_k}^{\zeta_{k+1}}\left(\mathbf{Z}^{(k\tau)\alpha_i}\right)^T\boldsymbol{\chi}^{(k)}H_1H_2\,d\zeta\right)A_1A_2\,d\alpha_1 d\alpha_2 = \\ &= \sum_{\tau=0}^{N+1}\sum_{i=1}^{5}\int_{\alpha_1}\int_{\alpha_2}\left(\delta\overline{\boldsymbol{\pi}}^{(\tau)\alpha_i}\right)^T\boldsymbol{\Sigma}^{(\tau)\alpha_i}A_1A_2\,d\alpha_1 d\alpha_2 \end{aligned} \tag{33}$$

where $\overline{\boldsymbol{\pi}}^{(\tau)\alpha_i T} = \left[\boldsymbol{\varepsilon}^{(\tau)\alpha_i T} \quad -\mathscr{E}^{(\tau)\alpha_i T} \quad -\widehat{\Delta}\mathrm{T}^{(\tau)\alpha_i} \quad \boldsymbol{\theta}^{(\tau)\alpha_i T}\right]^T$ is the improved vector of higher-order primary unknowns. Note that in Eqn. (33), the higher-order secondary variables vector $\boldsymbol{\Sigma}^{(\tau)\alpha_i}$ is introduced for each $\tau = 0,\dots,N+1$ and $i = 1,\dots,5$, which includes the integration with respect to the ζ thickness coordinate. It is convenient to express vector $\Sigma^{(\tau)\alpha_i} = \left[\mathbf{S}^{(\tau)\alpha_i T} \quad \mathbf{D}^{(\tau)\alpha_i T} \quad E^{(\tau)\alpha_i} \quad \mathbf{H}^{(\tau)\alpha_i T}\right]^T$ as an assembly of sub-vectors given below, in an extended form:

$$\begin{aligned} &\mathbf{S}^{(\tau)\alpha_i} = \left[N_1^{(\tau)\alpha_i} \quad N_2^{(\tau)\alpha_i} \quad N_{12}^{(\tau)\alpha_i} \quad N_{21}^{(\tau)\alpha_i} \quad T_1^{(\tau)\alpha_i} \quad T_2^{(\tau)\alpha_i} \quad P_1^{(\tau)\alpha_i} \quad P_2^{(\tau)\alpha_i} \quad S_3^{(\tau)\alpha_i}\right]^T \\ &\mathbf{D}^{(\tau)\alpha_i} = \left[D_1^{(\tau)\alpha_i} \quad D_2^{(\tau)\alpha_i} \quad D_3^{(\tau)\alpha_i}\right]^T, \quad \mathbf{H}^{(\tau)\alpha_i} = \left[H_1^{(\tau)\alpha_i} \quad H_2^{(\tau)\alpha_i} \quad H_3^{(\tau)\alpha_i}\right]^T \end{aligned} \tag{34}$$

By performing the matrix multiplications in Eqn. (33), it is possible to compute all elements of the secondary variables vectors (34) at an arbitrary point of the two-dimensional physical domain.

Substituting Eqn. (24) into Eqn. (33) yields a higher-order expression of the constitutive relation, which embeds the multifield constitutive relations for all laminae of the stacking sequence. Employing the higher-order kinematic equations (21) to compute the three-dimensional strain vector $\boldsymbol{\pi}^{(k)}$, the following results are obtained for an arbitrary $\tau = 0,\dots,N+1$ and $i = 1,\dots,5$:

$$\begin{aligned} \boldsymbol{\Sigma}^{(\tau)\alpha_i} &= \sum_{\eta=0}^{N+1}\sum_{j=1}^{5}\left(\sum_{k=1}^{l}\int_{\zeta_k}^{\zeta_{k+1}}\left(\mathbf{Z}^{(k\tau)\alpha_i}\right)^T\overline{\boldsymbol{\Gamma}}^{(k)}\mathbf{Z}^{(k\eta)\alpha_j}H_1H_2\,d\zeta\right)\boldsymbol{\pi}^{(\eta)\alpha_j} \\ &= \sum_{\eta=0}^{N+1}\sum_{j=1}^{5}\mathbf{A}^{(\tau\eta)\alpha_i\alpha_j}\boldsymbol{\pi}^{(\eta)\alpha_j} \end{aligned} \tag{35}$$

In the previous relation, the generalized constitutive matrix $\mathbf{A}^{(\tau\eta)\alpha_i\alpha_j}$ is introduced, which accounts for the multifield three-dimensional constitutive matrix, curvature effects, and kinematic model associated with an arbitrary $\tau,\eta = 0,\dots,N+1$ and $i,j = 1,\dots,5$. The arbitrary element $A_{rsnm\,(pq)}^{(\tau\eta)[fg]\,\alpha_i\alpha_j}$ with $r,s = \varepsilon,\phi,\mathrm{T}$ of matrix $\mathbf{A}^{(\tau\eta)\alpha_i\alpha_j}$ is evaluated according to Eqn. (35). By performing all matrix multiplications as detailed in Ref. [38], the following expression is obtained by setting the positions $\partial^0 F_\tau^{(k)\alpha_i}/\partial\zeta^0 = F_\tau^{(k)\alpha_i}$ and $\partial^0 F_\eta^{(k)\alpha_j}/\partial\zeta^0 = F_\eta^{(k)\alpha_j}$:

$$A_{rs\,nm\,(pq)}^{(\tau\eta)[fg]\,\alpha_i\alpha_j} = \sum_{k=1}^{l}\int_{\zeta_k}^{\zeta_{k+1}}\overline{\Upsilon}_{nm}^{(k)}\frac{\partial^f F_\tau^{(k)\alpha_i}}{\partial\zeta^f}\frac{\partial^g F_\eta^{(k)\alpha_j}}{\partial\zeta^g}\frac{H_1H_2}{H_1^pH_2^q}\,d\zeta \tag{36}$$

for $n,m = 1,\dots,13$, $p,q = 0,1,2$ and $f,g = 0,1$. Note that the quantity $\overline{\Upsilon}_{nm}^{(k)}$ refers to the arbitrary element of the rotated constitutive matrix $\overline{\boldsymbol{\Gamma}}^{(k)}$

from Eqn. (24). It is useful to express the generalized constitutive relation (35) using the representation of $\overline{\boldsymbol{\Gamma}}^{(k)}$ as given in Eqn. (24). To this end, the following sub-matrices are introduced [38]:

$$\mathbf{A}_{\varepsilon\varepsilon}^{(\tau\eta)\alpha_i\alpha_j} = \sum_{k=1}^{l}\int_{\zeta_k}^{\zeta_{k+1}}\left(\mathbf{Z}_1^{(k\tau)\alpha_i}\right)^T\overline{\boldsymbol{\Gamma}}_{\mathrm{C}}^{(k)}\mathbf{Z}_1^{(k\eta)\alpha_j}H_1H_2d\zeta = \left[\left(A_{\varepsilon\varepsilon nm(pq)}^{(\tau\eta)[fg]\alpha_i\alpha_j}\right)_{hs}\right]_{\substack{h=1,\dots,9\\ s=1,\dots,9}}$$

$$= \left[\begin{array}{cccccc|ccc}
A_{11(20)}^{(\tau\eta)[00]\alpha_i\alpha_j} & A_{12(11)}^{(\tau\eta)[00]\alpha_i\alpha_j} & A_{16(20)}^{(\tau\eta)[00]\alpha_i\alpha_j} & A_{16(11)}^{(\tau\eta)[00]\alpha_i\alpha_j} & A_{14(20)}^{(\tau\eta)[00]\alpha_i\alpha_j} & A_{15(11)}^{(\tau\eta)[00]\alpha_i\alpha_j} & A_{14(10)}^{(\tau\eta)[01]\alpha_i\alpha_j} & A_{15(10)}^{(\tau\eta)[01]\alpha_i\alpha_j} & A_{13(10)}^{(\tau\eta)[01]\alpha_i\alpha_j} \\
A_{12(11)}^{(\tau\eta)[00]\alpha_i\alpha_j} & A_{22(02)}^{(\tau\eta)[00]\alpha_i\alpha_j} & A_{26(11)}^{(\tau\eta)[00]\alpha_i\alpha_j} & A_{26(02)}^{(\tau\eta)[00]\alpha_i\alpha_j} & A_{24(11)}^{(\tau\eta)[00]\alpha_i\alpha_j} & A_{25(02)}^{(\tau\eta)[00]\alpha_i\alpha_j} & A_{24(01)}^{(\tau\eta)[01]\alpha_i\alpha_j} & A_{25(01)}^{(\tau\eta)[01]\alpha_i\alpha_j} & A_{23(01)}^{(\tau\eta)[01]\alpha_i\alpha_j} \\
A_{16(20)}^{(\tau\eta)[00]\alpha_i\alpha_j} & A_{26(11)}^{(\tau\eta)[00]\alpha_i\alpha_j} & A_{66(20)}^{(\tau\eta)[00]\alpha_i\alpha_j} & A_{66(11)}^{(\tau\eta)[00]\alpha_i\alpha_j} & A_{46(20)}^{(\tau\eta)[00]\alpha_i\alpha_j} & A_{56(11)}^{(\tau\eta)[00]\alpha_i\alpha_j} & A_{46(10)}^{(\tau\eta)[01]\alpha_i\alpha_j} & A_{56(10)}^{(\tau\eta)[01]\alpha_i\alpha_j} & A_{36(10)}^{(\tau\eta)[01]\alpha_i\alpha_j} \\
A_{16(11)}^{(\tau\eta)[00]\alpha_i\alpha_j} & A_{26(02)}^{(\tau\eta)[00]\alpha_i\alpha_j} & A_{66(11)}^{(\tau\eta)[00]\alpha_i\alpha_j} & A_{66(02)}^{(\tau\eta)[00]\alpha_i\alpha_j} & A_{46(11)}^{(\tau\eta)[00]\alpha_i\alpha_j} & A_{56(02)}^{(\tau\eta)[00]\alpha_i\alpha_j} & A_{46(01)}^{(\tau\eta)[01]\alpha_i\alpha_j} & A_{56(01)}^{(\tau\eta)[01]\alpha_i\alpha_j} & A_{36(01)}^{(\tau\eta)[01]\alpha_i\alpha_j} \\
A_{14(20)}^{(\tau\eta)[00]\alpha_i\alpha_j} & A_{24(11)}^{(\tau\eta)[00]\alpha_i\alpha_j} & A_{46(20)}^{(\tau\eta)[00]\alpha_i\alpha_j} & A_{46(11)}^{(\tau\eta)[00]\alpha_i\alpha_j} & A_{44(20)}^{(\tau\eta)[00]\alpha_i\alpha_j} & A_{45(11)}^{(\tau\eta)[00]\alpha_i\alpha_j} & A_{44(10)}^{(\tau\eta)[01]\alpha_i\alpha_j} & A_{45(10)}^{(\tau\eta)[01]\alpha_i\alpha_j} & A_{34(10)}^{(\tau\eta)[01]\alpha_i\alpha_j} \\
A_{15(11)}^{(\tau\eta)[00]\alpha_i\alpha_j} & A_{25(02)}^{(\tau\eta)[00]\alpha_i\alpha_j} & A_{56(11)}^{(\tau\eta)[00]\alpha_i\alpha_j} & A_{56(02)}^{(\tau\eta)[00]\alpha_i\alpha_j} & A_{45(11)}^{(\tau\eta)[00]\alpha_i\alpha_j} & A_{55(02)}^{(\tau\eta)[00]\alpha_i\alpha_j} & A_{45(01)}^{(\tau\eta)[01]\alpha_i\alpha_j} & A_{55(01)}^{(\tau\eta)[01]\alpha_i\alpha_j} & A_{35(01)}^{(\tau\eta)[01]\alpha_i\alpha_j} \\
\hline
A_{14(10)}^{(\tau\eta)[10]\alpha_i\alpha_j} & A_{24(01)}^{(\tau\eta)[10]\alpha_i\alpha_j} & A_{46(10)}^{(\tau\eta)[10]\alpha_i\alpha_j} & A_{46(01)}^{(\tau\eta)[10]\alpha_i\alpha_j} & A_{44(10)}^{(\tau\eta)[10]\alpha_i\alpha_j} & A_{45(01)}^{(\tau\eta)[10]\alpha_i\alpha_j} & A_{44(00)}^{(\tau\eta)[11]\alpha_i\alpha_j} & A_{45(00)}^{(\tau\eta)[11]\alpha_i\alpha_j} & A_{34(00)}^{(\tau\eta)[11]\alpha_i\alpha_j} \\
A_{15(10)}^{(\tau\eta)[10]\alpha_i\alpha_j} & A_{25(01)}^{(\tau\eta)[10]\alpha_i\alpha_j} & A_{56(10)}^{(\tau\eta)[10]\alpha_i\alpha_j} & A_{56(01)}^{(\tau\eta)[10]\alpha_i\alpha_j} & A_{45(10)}^{(\tau\eta)[10]\alpha_i\alpha_j} & A_{55(01)}^{(\tau\eta)[10]\alpha_i\alpha_j} & A_{45(00)}^{(\tau\eta)[11]\alpha_i\alpha_j} & A_{55(00)}^{(\tau\eta)[11]\alpha_i\alpha_j} & A_{35(00)}^{(\tau\eta)[11]\alpha_i\alpha_j} \\
A_{13(10)}^{(\tau\eta)[10]\alpha_i\alpha_j} & A_{23(01)}^{(\tau\eta)[10]\alpha_i\alpha_j} & A_{36(10)}^{(\tau\eta)[10]\alpha_i\alpha_j} & A_{36(01)}^{(\tau\eta)[10]\alpha_i\alpha_j} & A_{34(10)}^{(\tau\eta)[10]\alpha_i\alpha_j} & A_{35(01)}^{(\tau\eta)[10]\alpha_i\alpha_j} & A_{34(00)}^{(\tau\eta)[11]\alpha_i\alpha_j} & A_{35(00)}^{(\tau\eta)[11]\alpha_i\alpha_j} & A_{33(00)}^{(\tau\eta)[11]\alpha_i\alpha_j}
\end{array}\right]$$

$$\mathbf{A}_{\phi\phi}^{(\tau\eta)\alpha_i\alpha_j} = \sum_{k=1}^{l}\int_{\zeta_k}^{\zeta_{k+1}}\mathbf{Z}_2^{(k\tau)\alpha_i}\overline{\boldsymbol{\Gamma}}_{\mathrm{L}}^{(k)}\mathbf{Z}_2^{(k\eta)\alpha_j}H_1H_2d\zeta = \left[\left(A_{\phi\phi nm(pq)}^{(\tau\eta)[fg]\alpha_i\alpha_j}\right)_{hs}\right]_{\substack{h=1,2,3\\ s=1,2,3}} = \left[\begin{array}{cc|c}
L_{11(20)}^{(\tau\eta)[00]\alpha_i\alpha_j} & L_{12(11)}^{(\tau\eta)[00]\alpha_i\alpha_j} & L_{13(10)}^{(\tau\eta)[01]\alpha_i\alpha_j} \\
L_{12(11)}^{(\tau\eta)[00]\alpha_i\alpha_j} & L_{22(02)}^{(\tau\eta)[00]\alpha_i\alpha_j} & L_{23(01)}^{(\tau\eta)[01]\alpha_i\alpha_j} \\
\hline
L_{13(10)}^{(\tau\eta)[10]\alpha_i\alpha_j} & L_{23(01)}^{(\tau\eta)[10]\alpha_i\alpha_j} & L_{33(00)}^{(\tau\eta)[11]\alpha_i\alpha_j}
\end{array}\right]$$

$$\mathbf{A}_{\varepsilon\phi}^{(\tau\eta)\alpha_i\alpha_j} = -\sum_{k=1}^{l}\int_{\zeta_k}^{\zeta_{k+1}}\left(\mathbf{Z}_1^{(k\tau)\alpha_i}\right)^T\overline{\boldsymbol{\Gamma}}_{\mathrm{P}}^{(k)T}\mathbf{Z}_2^{(k\eta)\alpha_j}H_1H_2d\zeta = \left[\left(A_{\varepsilon\phi nm(pq)}^{(\tau\eta)[fg]\alpha_i\alpha_j}\right)_{hs}\right]_{\substack{h=1,\dots,9\\ s=1,2,3}}$$

$$= -\left[\begin{array}{cccccc|ccc}
P_{11(20)}^{(\tau\eta)[00]\alpha_i\alpha_j} & P_{12(11)}^{(\tau\eta)[00]\alpha_i\alpha_j} & P_{16(20)}^{(\tau\eta)[00]\alpha_i\alpha_j} & P_{16(11)}^{(\tau\eta)[00]\alpha_i\alpha_j} & P_{14(20)}^{(\tau\eta)[00]\alpha_i\alpha_j} & P_{15(11)}^{(\tau\eta)[00]\alpha_i\alpha_j} & P_{14(10)}^{(\tau\eta)[10]\alpha_i\alpha_j} & P_{15(10)}^{(\tau\eta)[10]\alpha_i\alpha_j} & P_{13(10)}^{(\tau\eta)[10]\alpha_i\alpha_j} \\
P_{21(11)}^{(\tau\eta)[00]\alpha_i\alpha_j} & P_{22(02)}^{(\tau\eta)[00]\alpha_i\alpha_j} & P_{26(11)}^{(\tau\eta)[00]\alpha_i\alpha_j} & P_{26(02)}^{(\tau\eta)[00]\alpha_i\alpha_j} & P_{24(11)}^{(\tau\eta)[00]\alpha_i\alpha_j} & P_{25(02)}^{(\tau\eta)[00]\alpha_i\alpha_j} & P_{24(01)}^{(\tau\eta)[10]\alpha_i\alpha_j} & P_{25(01)}^{(\tau\eta)[10]\alpha_i\alpha_j} & P_{23(01)}^{(\tau\eta)[10]\alpha_i\alpha_j} \\
\hline
P_{31(10)}^{(\tau\eta)[01]\alpha_i\alpha_j} & P_{32(01)}^{(\tau\eta)[01]\alpha_i\alpha_j} & P_{36(10)}^{(\tau\eta)[01]\alpha_i\alpha_j} & P_{36(01)}^{(\tau\eta)[01]\alpha_i\alpha_j} & P_{34(10)}^{(\tau\eta)[01]\alpha_i\alpha_j} & P_{35(01)}^{(\tau\eta)[01]\alpha_i\alpha_j} & P_{34(00)}^{(\tau\eta)[11]\alpha_i\alpha_j} & P_{35(00)}^{(\tau\eta)[11]\alpha_i\alpha_j} & P_{33(00)}^{(\tau\eta)[11]\alpha_i\alpha_j}
\end{array}\right]^T$$

$$\mathbf{A}_{\phi\varepsilon}^{(\tau\eta)\alpha_i\alpha_j} = \sum_{k=1}^{l}\int_{\zeta_k}^{\zeta_{k+1}}\mathbf{Z}_2^{(k\tau)\alpha_i}\overline{\boldsymbol{\Gamma}}_{\mathrm{P}}^{(k)}\mathbf{Z}_1^{(k\eta)\alpha_j}H_1H_2d\zeta = \left[\left(A_{\phi\varepsilon nm(pq)}^{(\tau\eta)[fg]\alpha_i\alpha_j}\right)_{hs}\right]_{\substack{h=1,2,3\\ s=1,\dots,9}}$$

$$= \left[\begin{array}{cccccc|ccc}
P_{11(20)}^{(\tau\eta)[00]\alpha_i\alpha_j} & P_{12(11)}^{(\tau\eta)[00]\alpha_i\alpha_j} & P_{16(20)}^{(\tau\eta)[00]\alpha_i\alpha_j} & P_{16(11)}^{(\tau\eta)[00]\alpha_i\alpha_j} & P_{14(20)}^{(\tau\eta)[00]\alpha_i\alpha_j} & P_{15(11)}^{(\tau\eta)[00]\alpha_i\alpha_j} & P_{14(10)}^{(\tau\eta)[01]\alpha_i\alpha_j} & P_{15(10)}^{(\tau\eta)[01]\alpha_i\alpha_j} & P_{13(10)}^{(\tau\eta)[01]\alpha_i\alpha_j} \\
P_{21(11)}^{(\tau\eta)[00]\alpha_i\alpha_j} & P_{22(02)}^{(\tau\eta)[00]\alpha_i\alpha_j} & P_{26(11)}^{(\tau\eta)[00]\alpha_i\alpha_j} & P_{26(02)}^{(\tau\eta)[00]\alpha_i\alpha_j} & P_{24(11)}^{(\tau\eta)[00]\alpha_i\alpha_j} & P_{25(02)}^{(\tau\eta)[00]\alpha_i\alpha_j} & P_{24(01)}^{(\tau\eta)[01]\alpha_i\alpha_j} & P_{25(01)}^{(\tau\eta)[01]\alpha_i\alpha_j} & P_{23(01)}^{(\tau\eta)[01]\alpha_i\alpha_j} \\
\hline
P_{31(10)}^{(\tau\eta)[10]\alpha_i\alpha_j} & P_{32(01)}^{(\tau\eta)[10]\alpha_i\alpha_j} & P_{36(10)}^{(\tau\eta)[10]\alpha_i\alpha_j} & P_{36(01)}^{(\tau\eta)[10]\alpha_i\alpha_j} & P_{34(10)}^{(\tau\eta)[10]\alpha_i\alpha_j} & P_{35(01)}^{(\tau\eta)[10]\alpha_i\alpha_j} & P_{34(00)}^{(\tau\eta)[11]\alpha_i\alpha_j} & P_{35(00)}^{(\tau\eta)[11]\alpha_i\alpha_j} & P_{33(00)}^{(\tau\eta)[11]\alpha_i\alpha_j}
\end{array}\right]$$

$$\mathbf{A}_{\varepsilon\mathrm{T}}^{(\tau\eta)\alpha_i\alpha_j} = -\left[\begin{array}{ccccccccc} Z_{11(10)}^{(\tau\eta)[00]\alpha_i\alpha_j} & Z_{22(01)}^{(\tau\eta)[00]\alpha_i\alpha_j} & Z_{12(10)}^{(\tau\eta)[00]\alpha_i\alpha_j} & Z_{12(01)}^{(\tau\eta)[00]\alpha_i\alpha_j} & Z_{13(10)}^{(\tau\eta)[00]\alpha_i\alpha_j} & Z_{23(01)}^{(\tau\eta)[00]\alpha_i\alpha_j} & Z_{13(00)}^{(\tau\eta)[10]\alpha_i\alpha_j} & Z_{23(00)}^{(\tau\eta)[10]\alpha_i\alpha_j} & Z_{33(00)}^{(\tau\eta)[10]\alpha_i\alpha_j} \end{array}\right]^T$$

$$\mathbf{A}_{\mathrm{T}\varepsilon}^{(\tau\eta)\alpha_i\alpha_j} = \left[\begin{array}{ccccccccc} Z_{11(10)}^{(\tau\eta)[00]\alpha_i\alpha_j} & Z_{22(01)}^{(\tau\eta)[00]\alpha_i\alpha_j} & Z_{12(10)}^{(\tau\eta)[00]\alpha_i\alpha_j} & Z_{12(01)}^{(\tau\eta)[00]\alpha_i\alpha_j} & Z_{13(10)}^{(\tau\eta)[00]\alpha_i\alpha_j} & Z_{23(01)}^{(\tau\eta)[00]\alpha_i\alpha_j} & Z_{13(00)}^{(\tau\eta)[01]\alpha_i\alpha_j} & Z_{23(00)}^{(\tau\eta)[01]\alpha_i\alpha_j} & Z_{33(00)}^{(\tau\eta)[01]\alpha_i\alpha_j} \end{array}\right]$$

$$\mathbf{A}_{\phi\mathrm{T}}^{(\tau\eta)\alpha_i\alpha_j} = \sum_{k=1}^{l}\int_{\zeta_k}^{\zeta_{k+1}}\mathbf{Z}_2^{(k\tau)\alpha_i}\overline{\boldsymbol{\Gamma}}_{\mathrm{o}}^{(k)T}F_\eta^{(k)\alpha_j}H_1H_2d\zeta = \left[\left(A_{\phi\mathrm{T}nm(pq)}^{(\tau\eta)[fg]\alpha_i\alpha_j}\right)_{hs}\right]_{\substack{h=1,2,3\\ s=1}} = \left[\begin{array}{ccc} O_{11(10)}^{(\tau\eta)[00]\alpha_i\alpha_j} & O_{22(01)}^{(\tau\eta)[00]\alpha_i\alpha_j} & O_{33(00)}^{(\tau\eta)[01]\alpha_i\alpha_j} \end{array}\right]^T$$

$$\mathbf{A}_{\mathrm{T}\phi}^{(\tau\eta)\alpha_i\alpha_j} = \sum_{k=1}^{l}\int_{\zeta_k}^{\zeta_{k+1}}F_\tau^{(k)\alpha_i}\overline{\boldsymbol{\Gamma}}_{\mathrm{o}}^{(k)}\mathbf{Z}_2^{(k\eta)\alpha_j}H_1H_2d\zeta = \left[\left(A_{\mathrm{T}\phi nm(pq)}^{(\tau\eta)[fg]\alpha_i\alpha_j}\right)_{hs}\right]_{\substack{h=1\\ s=1,2,3}} = \left[\begin{array}{ccc} O_{11(10)}^{(\tau\eta)[00]\alpha_i\alpha_j} & O_{22(01)}^{(\tau\eta)[00]\alpha_i\alpha_j} & O_{33(00)}^{(\tau\eta)[10]\alpha_i\alpha_j} \end{array}\right]$$

$$\mathbf{A}_{\mathrm{TT}}^{(\tau\eta)\alpha_i\alpha_j} = \sum_{k=1}^{l}\int_{\zeta_k}^{\zeta_{k+1}}F_\tau^{(k)\alpha_i}\overline{\Xi}_{11}^{(k)}F_\eta^{(k)\alpha_j}H_1H_2d\zeta = \left[\left(A_{\mathrm{TT}nm(pq)}^{(\tau\eta)[fg]\alpha_i\alpha_j}\right)_{hs}\right]_{\substack{h=1\\ s=1}} = C_{11(00)}^{(\tau\eta)[00]\alpha_i\alpha_j}$$

$$\mathbf{A}_{00}^{(\tau\eta)\alpha_i\alpha_j}=\left[\begin{array}{cc|c} K_{11(20)}^{(\tau\eta)[00]\alpha_i\alpha_j} & K_{12(11)}^{(\tau\eta)[00]\alpha_i\alpha_j} & K_{13(10)}^{(\tau\eta)[01]\alpha_i\alpha_j} \\ K_{12(11)}^{(\tau\eta)[00]\alpha_i\alpha_j} & K_{22(02)}^{(\tau\eta)[00]\alpha_i\alpha_j} & K_{23(01)}^{(\tau\eta)[01]\alpha_i\alpha_j} \\ \hline K_{13(10)}^{(\tau\eta)[10]\alpha_i\alpha_j} & K_{23(01)}^{(\tau\eta)[10]\alpha_i\alpha_j} & K_{33(00)}^{(\tau\eta)[11]\alpha_i\alpha_j} \end{array}\right] \tag{37}$$

An extended version of the matrices in Eqn. (37) can be found in Ref. [38]. The following expression is, thus, obtained for Eqn. (35):

$$\begin{bmatrix} \mathbf{S}^{(\tau)\alpha_i} \\ \mathbf{D}^{(\tau)\alpha_i} \\ E^{(\tau)\alpha_i} \\ \mathbf{H}^{(\tau)\alpha_i} \end{bmatrix}=\sum_{\eta=0}^{N+1}\sum_{j=1}^{5}\begin{bmatrix} \mathbf{A}_{\varepsilon\varepsilon}^{(\tau\eta)\alpha_i\alpha_j} & \mathbf{A}_{\varepsilon\phi}^{(\tau\eta)\alpha_i\alpha_j} & \mathbf{A}_{\varepsilon \mathrm{T}}^{(\tau\eta)\alpha_i\alpha_j} & \mathbf{0} \\ \mathbf{A}_{\phi\varepsilon}^{(\tau\eta)\alpha_i\alpha_j} & \mathbf{A}_{\phi\phi}^{(\tau\eta)\alpha_i\alpha_j} & \mathbf{A}_{\phi \mathrm{T}}^{(\tau\eta)\alpha_i\alpha_j} & \mathbf{0} \\ \mathbf{A}_{\mathrm{T}\varepsilon}^{(\tau\eta)\alpha_i\alpha_j} & \mathbf{A}_{\mathrm{T}\phi}^{(\tau\eta)\alpha_i\alpha_j} & \mathbf{A}_{\mathrm{TT}}^{(\tau\eta)\alpha_i\alpha_j} & \mathbf{0} \\ \mathbf{0} & \mathbf{0} & \mathbf{0} & \mathbf{A}_{\theta\theta}^{(\tau\eta)\alpha_i\alpha_j} \end{bmatrix}\begin{bmatrix} \boldsymbol{\varepsilon}^{(\eta)\alpha_j} \\ \mathscr{E}^{(\eta)\alpha_j} \\ \widehat{\Delta \mathrm{T}}^{(\eta)\alpha_j} \\ \boldsymbol{\theta}^{(\eta)\alpha_j} \end{bmatrix} \tag{38}$$

Finally, the generalized constitutive relation (35) is written in a useful form by expressing the generalized secondary variables in terms of the elements of vector $\boldsymbol{\delta}^{(\eta)}$ with $\eta = 0,...,N+1$, which are the unknown variables in the multifield formulation. Introducing in the higher-order constitutive relation (35) and the kinematic model of Eqn. (9), the following relation is obtained, presented in condensed form as:

$$\boldsymbol{\Sigma}^{(\tau)\alpha_i}=\sum_{\eta=0}^{N+1}\sum_{j=1}^{5}\mathbf{A}^{(\tau\eta)\alpha_i\alpha_j}\mathbf{D}_{\Omega}^{\alpha_j}\boldsymbol{\delta}^{(\eta)}=\sum_{\eta=0}^{N+1}\mathbf{O}^{(\tau\eta)\alpha_i}\boldsymbol{\delta}^{(\eta)} \tag{39}$$

The generalized higher-order balance equations for the coupled thermo-electro-mechanical case are derived from the Master Balance principle, as expressed by the following relation:

$$\int_{t_1}^{t_2}\delta \mathrm{E}\,dt=\int_{t_1}^{t_2}\left(\delta L_s+\delta L_{efk}+\delta L_{\mathrm{T}}-\delta \mathrm{Y}\right)dt=0 \tag{40}$$

for any time interval $[t_1,t_2]$ with $t_1<t_2$. More specifically, the virtual variation δY of the total energy of the system is the same as introduced in Eqn. (33). The terms δL_s and δL_{efk} refer to the virtual works associated with the multifield external actions from an external elastic foundation and from applied loads, respectively. It is assumed that external loads are applied to the top $(+)$ and bottom $(-)$ surfaces of the doubly-curved shell solid. These loads consist of mechanical forces $q_1^{(+)}$, $q_2^{(+)}$, $q_3^{(+)}$ and $q_1^{(-)}$, $q_2^{(-)}$, $q_3^{(-)}$, electrostatic fluxes $q_{\mathrm{D}}^{(-)}$, $q_{\mathrm{D}}^{(+)}$, and thermal fluxes $q_h^{(-)}$, $q_h^{(+)}$. Since these loads are generally distributed to the top and bottom surfaces, they are expressed as the product of a reference magnitude $\overline{q}_1^{(\pm)}$, $\overline{q}_2^{(\pm)}$, $\overline{q}_3^{(\pm)}$, $\overline{q}_{\mathrm{D}}^{(\pm)}$, $\overline{q}_h^{(\pm)}$ and a general surface distribution function $\widetilde{q}_1^{(\pm)}$, $\widetilde{q}_2^{(\pm)}$, $\widetilde{q}_3^{(\pm)}$, $\widetilde{q}_{\mathrm{D}}^{(\pm)}$, $\widetilde{q}_h^{(\pm)}$:

$$q_\alpha^{(\pm)}(s_1,s_2)=\overline{q}_\alpha^{(\pm)}\widetilde{q}_\alpha^{(\pm)}(s_1,s_2) \tag{41}$$

with $\alpha=1,2,3,\mathrm{D},h$.The virtual work δL_s can be computed as follows:

where $H_i^{(\pm)}=H_1^{(\pm)}H_2^{(\pm)}$ with $H_i^{(\pm)}=1\pm h/(2R_i)$ for $i=1,2$ are the geometry scaling parameters of the shell evaluated at $\zeta=h/2$ and $\zeta=-h/2$, respectively, and T_0 denotes the reference temperature. Note that the total thickness h is evaluated at each point of the two-dimensional physical domain $[\alpha_1^0,\alpha_1^1]\times[\alpha_2^0,\alpha_2^1]$ according to Eqn. (8), while the principal radius of curvature R_i along the $\alpha_i=\alpha_1,\alpha_2$ principal direction is introduced in Eqn. (4). The external actions induced by an elastic foundation depend on the displacement field variables $U_1^{(\pm)},U_2^{(\pm)},U_3^{(\pm)}$ at the top and bottom surfaces, respectively, according to the Winkler-Pasternak model:

$$\begin{aligned} q_{1efk}^{(\pm)}&=-k_{1f}^{(\pm)}U_1^{(\pm)} \\ q_{2efk}^{(\pm)}&=-k_{2f}^{(\pm)}U_2^{(\pm)} \\ q_{3efk}^{(\pm)}&=-k_{3f}^{(\pm)}U_3^{(\pm)}+G_f^{(\pm)}\nabla_{(\pm)}^2U_3^{(\pm)} \end{aligned} \tag{43}$$

In the previous relation, $k_{1f}^{(\pm)},k_{2f}^{(\pm)}$ and $k_{3f}^{(\pm)}$ denote the stiffness of linear elastic springs expressed in $[\mathrm{N/m^3}]$, while $G_f^{(\pm)}$ is defined in $[\mathrm{N/m^2}]$ and accounts for the shear properties of the foundation. The Laplacian operator $\nabla_{(\pm)}^2$ is computed in curvilinear principal coordinates α_1,α_2 by using the expression reported in [38]. The virtual work δL_{efk} associated with the foundation loads (43) is evaluated as:

$$\delta L_{efk}=\int_{\alpha_1}\int_{\alpha_2}\left(q_{1efk}^{(\pm)}\delta U_1^{(-)}+q_{2efk}^{(\pm)}\delta U_2^{(-)}+q_{3efk}^{(\pm)}\delta U_3^{(\pm)}\right)H_1^{(\pm)}H_2^{(\pm)}A_1A_2d\alpha_1d\alpha_2 \tag{44}$$

Introducing the kinematic model from Eqn. (9) into Eqn. (42) and Eqn. (44), the generalized external actions $\widetilde{q}_{1s}^{(\tau)}=q_{1efk}^{(\tau)}+q_1^{(\tau)}$, $\widetilde{q}_{2s}^{(\tau)}=q_{2efk}^{(\tau)}+q_2^{(\tau)}$, $\widetilde{q}_{3s}^{(\tau)}=q_{3efk}^{(\tau)}+q_3^{(\tau)}$, $q_{\mathrm{Ds}}^{(\tau)}=q_{\mathrm{D}}^{(\tau)}$, $q_{\mathrm{Ts}}^{(\tau)}=q_h^{(\tau)}$ are introduced to express the virtual works δL_s and δL_{efk} in terms of the generalized configuration variables. These quantities are evaluated at an arbitrary point (α_1,α_2) using the relations provided below:

$$\begin{aligned} \widetilde{q}_{1s}^{(\tau)}&=q_{1s}^{(-)}F_\tau^{(1)\alpha_1(-)}H_1^{(-)}H_2^{(-)}+q_{1s}^{(+)}F_\tau^{(l)\alpha_1(+)}H_1^{(+)}H_2^{(+)} \\ \widetilde{q}_{2s}^{(\tau)}&=q_{2s}^{(-)}F_\tau^{(1)\alpha_2(-)}H_1^{(-)}H_2^{(-)}+q_{2s}^{(+)}F_\tau^{(l)\alpha_2(+)}H_1^{(+)}H_2^{(+)} \\ \widetilde{q}_{3s}^{(\tau)}&=q_{3s}^{(-)}F_\tau^{(1)\alpha_3(-)}H_1^{(-)}H_2^{(-)}+q_{3s}^{(+)}F_\tau^{(l)\alpha_3(+)}H_1^{(+)}H_2^{(+)} \\ q_{\mathrm{Ds}}^{(\tau)}&=q_{\mathrm{Ds}}^{(-)}F_\tau^{(1)\alpha_4(-)}H_1^{(-)}H_2^{(-)}+q_{\mathrm{Ds}}^{(+)}F_\tau^{(l)\alpha_4(+)}H_1^{(+)}H_2^{(+)} \\ q_{\mathrm{Ts}}^{(\tau)}&=q_{\mathrm{Ts}}^{(-)}F_\tau^{(1)\alpha_5(-)}H_1^{(-)}H_2^{(-)}+q_{\mathrm{Ts}}^{(+)}F_\tau^{(l)\alpha_5(+)}H_1^{(+)}H_2^{(+)} \end{aligned} \tag{45}$$

where the terms $q_{1s}^{(+)},q_{2s}^{(+)},q_{3s}^{(+)},q_{\mathrm{Ds}}^{(+)},q_{\mathrm{Ts}}^{(+)}$ and $q_{1s}^{(-)},q_{2s}^{(-)},q_{3s}^{(-)},q_{\mathrm{Ds}}^{(-)},q_{\mathrm{Ts}}^{(-)}$ are the sum of the corresponding external surface loads and the actions from elastic foundation at the top and boto surfaces. Finally, the virtual work δL_{T} accounts for the energy contribution of the reference entropy of the system, denoted by $\overline{\eta}^{(k)}$ with $k=1,...,l$:

$$\delta L_{\mathrm{T}}=-\sum_{k=1}^{l}\int_{\zeta_k}^{\zeta_{k+1}}\int_{\alpha_1}\int_{\alpha_2}\overline{\eta}^{(k)}\delta\Delta\mathrm{T}^{(k)}H_1H_2A_1A_2d\alpha_1d\alpha_2d\zeta \tag{46}$$

$$\begin{aligned} &\delta L_s=\delta L_{es}+\delta L_{\phi s}+\delta L_{\mathrm{T}s}= \\ &=\int_{\alpha_1}\int_{\alpha_2}\left(\left(q_1^{(-)}\delta U_1^{(-)}+q_2^{(-)}\delta U_2^{(-)}+q_3^{(-)}\delta U_3^{(-)}+q_{\mathrm{D}}^{(-)}\delta\Delta\phi^{(-)}+\frac{q_h^{(-)}}{\mathrm{T}_0}\delta\Delta\mathrm{T}^{(-)}\right)H_1^{(-)}H_2^{(-)}+\right. \\ &\left.+\left(q_1^{(+)}\delta U_1^{(+)}+q_2^{(+)}\delta U_2^{(+)}+q_3^{(+)}\delta U_3^{(+)}+q_{\mathrm{D}}^{(+)}\delta\Delta\phi^{(+)}+\frac{q_h^{(+)}}{\mathrm{T}_0}\delta\Delta\mathrm{T}^{(+)}\right)H_1^{(+)}H_2^{(+)}\right)A_1A_2d\alpha_1d\alpha_2 \end{aligned} \tag{42}$$

In this work, it is assumed a thermodynamic equilibrium for the system, which means that the virtual work in Eqn. (46) is null.

Based on these definitions, all energetic contributions are substituted into Eqn. (40). Then, applying the integration-by-parts rule and performing some mathematical manipulations [38], the following multifield balance equations are derived for a thermo-electro-elastic doubly-curved shell, associated with an arbitrary $\tau = 0, \ldots, N+1$:

$$
\begin{aligned}
&\frac{1}{A_1}\frac{\partial N_1^{(\tau)\alpha_1}}{\partial \alpha_1} + \frac{N_1^{(\tau)\alpha_1}}{A_1A_2}\frac{\partial A_2}{\partial \alpha_1} + \frac{1}{A_2}\frac{\partial N_{21}^{(\tau)\alpha_1}}{\partial \alpha_2} + \frac{N_{21}^{(\tau)\alpha_1}}{A_1A_2}\frac{\partial A_1}{\partial \alpha_2} + \frac{N_{12}^{(\tau)\alpha_1}}{A_1A_2}\frac{\partial A_1}{\partial \alpha_2} \\
&- \frac{N_2^{(\tau)\alpha_1}}{A_1A_2}\frac{\partial A_2}{\partial \alpha_1} + \frac{T_1^{(\tau)\alpha_1}}{R_1} - P_1^{(\tau)\alpha_1} + q_{1s}^{(\tau)} = 0 \\
&\frac{1}{A_2}\frac{\partial N_2^{(\tau)\alpha_2}}{\partial \alpha_2} + \frac{N_2^{(\tau)\alpha_2}}{A_1A_2}\frac{\partial A_1}{\partial \alpha_2} + \frac{1}{A_1}\frac{\partial N_{12}^{(\tau)\alpha_2}}{\partial \alpha_1} + \frac{N_{12}^{(\tau)\alpha_2}}{A_1A_2}\frac{\partial A_2}{\partial \alpha_1} + \frac{N_{21}^{(\tau)\alpha_2}}{A_1A_2}\frac{\partial A_2}{\partial \alpha_1} \\
&- \frac{N_1^{(\tau)\alpha_2}}{A_1A_2}\frac{\partial A_1}{\partial \alpha_2} + \frac{T_2^{(\tau)\alpha_2}}{R_2} - P_2^{(\tau)\alpha_2} + q_{2s}^{(\tau)} = 0 \\
&\frac{1}{A_1}\frac{\partial T_1^{(\tau)\alpha_3}}{\partial \alpha_1} + \frac{T_1^{(\tau)\alpha_3}}{A_1A_2}\frac{\partial A_2}{\partial \alpha_1} + \frac{1}{A_2}\frac{\partial T_2^{(\tau)\alpha_3}}{\partial \alpha_2} + \frac{T_2^{(\tau)\alpha_3}}{A_1A_2}\frac{\partial A_1}{\partial \alpha_2} - \frac{N_1^{(\tau)\alpha_3}}{R_1} \\
&- \frac{N_2^{(\tau)\alpha_3}}{R_2} - S_3^{(\tau)\alpha_3} + q_{3s}^{(\tau)} = 0 \\
&\frac{1}{A_1}\frac{\partial D_1^{(\tau)\alpha_4}}{\partial \alpha_1} + \frac{D_1^{(\tau)\alpha_4}}{A_1A_2}\frac{\partial A_2}{\partial \alpha_1} + \frac{1}{A_2}\frac{\partial D_2^{(\tau)\alpha_4}}{\partial \alpha_2} + \frac{D_2^{(\tau)\alpha_4}}{A_1A_2}\frac{\partial A_1}{\partial \alpha_2} - D_3^{(\tau)\alpha_4} + q_{\mathrm{D}s}^{(\tau)} = 0 \\
&\frac{1}{A_1}\frac{\partial H_1^{(\tau)\alpha_5}}{\partial \alpha_1} + \frac{H_1^{(\tau)\alpha_5}}{A_1A_2}\frac{\partial A_2}{\partial \alpha_1} + \frac{1}{A_2}\frac{\partial H_2^{(\tau)\alpha_5}}{\partial \alpha_2} + \frac{H_2^{(\tau)\alpha_5}}{A_1A_2}\frac{\partial A_1}{\partial \alpha_2} - H_3^{(\tau)\alpha_5} + q_{\mathrm{T}s}^{(\tau)} = 0
\end{aligned} \tag{47}
$$

Using a compact matrix form, the previous relations can be expressed as follows:

$$
\sum_{i=1}^{5} \mathbf{D}_\Omega^{*\alpha_i} \Sigma^{(\tau)\alpha_i} + \mathbf{q}_s^{(\tau)} = \sum_{i=1}^{5} \mathbf{D}_\Omega^{*\alpha_i} \Sigma^{(\tau)\alpha_i} + \boldsymbol{q}_{efk}^{(\tau)} + \boldsymbol{q}^{(\tau)} = \mathbf{0} \tag{48}
$$

where $\boldsymbol{q}_{efk}^{(\tau)} = \begin{bmatrix} q_{1efk}^{(\tau)} & q_{2efk}^{(\tau)} & q_{3efk}^{(\tau)} & 0 & 0 \end{bmatrix}^T$ and $\boldsymbol{q}^{(\tau)} = \begin{bmatrix} q_1^{(\tau)} & q_2^{(\tau)} & q_3^{(\tau)} & q_{\mathrm{D}}^{(\tau)} & q_h^{(\tau)} \end{bmatrix}^T$ include the generalized multifield external actions (45) for $\tau = 0, \ldots, N+1$, while the balance operators $\mathbf{D}_\Omega^{*\alpha_i}$ with $i = 1, \ldots, 5$ assume the following form:

$$
\begin{aligned}
&\mathbf{D}_\Omega^{*\alpha_1} = \begin{bmatrix} \overline{\mathbf{D}}_\Omega^{*\alpha_1} & \mathbf{0} & 0 & \mathbf{0} \\ \mathbf{0} & \mathbf{0} & 0 & \mathbf{0} \\ \mathbf{0} & \mathbf{0} & 0 & \mathbf{0} \\ \mathbf{0} & \mathbf{0} & 0 & \mathbf{0} \\ \mathbf{0} & \mathbf{0} & 0 & \mathbf{0} \end{bmatrix}, \quad \mathbf{D}_\Omega^{*\alpha_2} = \begin{bmatrix} \mathbf{0} & \mathbf{0} & 0 & \mathbf{0} \\ \overline{\mathbf{D}}_\Omega^{*\alpha_2} & \mathbf{0} & 0 & \mathbf{0} \\ \mathbf{0} & \mathbf{0} & 0 & \mathbf{0} \\ \mathbf{0} & \mathbf{0} & 0 & \mathbf{0} \\ \mathbf{0} & \mathbf{0} & 0 & \mathbf{0} \end{bmatrix}, \quad \mathbf{D}_\Omega^{*\alpha_3} = \begin{bmatrix} \mathbf{0} & \mathbf{0} & 0 & \mathbf{0} \\ \mathbf{0} & \mathbf{0} & 0 & \mathbf{0} \\ \overline{\mathbf{D}}_\Omega^{*\alpha_3} & \mathbf{0} & 0 & \mathbf{0} \\ \mathbf{0} & \mathbf{0} & 0 & \mathbf{0} \\ \mathbf{0} & \mathbf{0} & 0 & \mathbf{0} \end{bmatrix}, \\
&\mathbf{D}_\Omega^{*\alpha_4} = \begin{bmatrix} \mathbf{0} & \mathbf{0} & 0 & \mathbf{0} \\ \mathbf{0} & \mathbf{0} & 0 & \mathbf{0} \\ \mathbf{0} & \mathbf{0} & 0 & \mathbf{0} \\ \mathbf{0} & \overline{\mathbf{D}}_\Omega^{*\alpha_4} & 0 & \mathbf{0} \\ \mathbf{0} & \mathbf{0} & 0 & \mathbf{0} \end{bmatrix}, \quad \mathbf{D}_\Omega^{*\alpha_5} = \begin{bmatrix} \mathbf{0} & \mathbf{0} & 0 & \mathbf{0} \\ \mathbf{0} & \mathbf{0} & 0 & \mathbf{0} \\ \mathbf{0} & \mathbf{0} & 0 & \mathbf{0} \\ \mathbf{0} & \mathbf{0} & 0 & \mathbf{0} \\ \mathbf{0} & \mathbf{0} & 0 & \overline{\mathbf{D}}_\Omega^{*\alpha_5} \end{bmatrix}
\end{aligned} \tag{49}
$$

with $\overline{\mathbf{D}}_\Omega^{*\alpha_1}, \overline{\mathbf{D}}_\Omega^{*\alpha_2}, \overline{\mathbf{D}}_\Omega^{*\alpha_3}, \overline{\mathbf{D}}_\Omega^{*\alpha_4}, \overline{\mathbf{D}}_\Omega^{*\alpha_5}$ are defined in curvilinear principal co-ordinates as follows:

$$
\begin{aligned}
\overline{\mathbf{D}}_\Omega^{*\alpha_1} &= \begin{bmatrix} \frac{1}{A_1}\frac{\partial}{\partial \alpha_1} + \frac{1}{A_1A_2}\frac{\partial A_2}{\partial \alpha_1} & -\frac{1}{A_1A_2}\frac{\partial A_2}{\partial \alpha_1} & \frac{1}{A_1A_2}\frac{\partial A_1}{\partial \alpha_2} & \frac{1}{A_2}\frac{\partial}{\partial \alpha_2} + \frac{1}{A_1A_2}\frac{\partial A_1}{\partial \alpha_2} & \frac{1}{R_1} & 0 & -1 & 0 & 0 \end{bmatrix} \\
\overline{\mathbf{D}}_\Omega^{*\alpha_2} &= \begin{bmatrix} -\frac{1}{A_1A_2}\frac{\partial A_1}{\partial \alpha_2} & \frac{1}{A_2}\frac{\partial}{\partial \alpha_2} + \frac{1}{A_1A_2}\frac{\partial A_1}{\partial \alpha_2} & \frac{1}{A_1}\frac{\partial}{\partial \alpha_1} + \frac{1}{A_1A_2}\frac{\partial A_2}{\partial \alpha_1} & \frac{1}{A_1A_2}\frac{\partial A_2}{\partial \alpha_1} & 0 & \frac{1}{R_2} & 0 & -1 & 0 \end{bmatrix} \\
\overline{\mathbf{D}}_\Omega^{*\alpha_3} &= \begin{bmatrix} -\frac{1}{R_1} & -\frac{1}{R_2} & 0 & 0 & \frac{1}{A_1}\frac{\partial}{\partial \alpha_1} + \frac{1}{A_1A_2}\frac{\partial A_2}{\partial \alpha_1} & \frac{1}{A_2}\frac{\partial}{\partial \alpha_2} + \frac{1}{A_1A_2}\frac{\partial A_1}{\partial \alpha_2} & 0 & 0 & -1 \end{bmatrix}
\end{aligned}
$$

$$
\overline{\mathbf{D}}_\Omega^{*\alpha_4} = \overline{\mathbf{D}}_\Omega^{*\alpha_5} = \begin{bmatrix} \frac{1}{A_1}\frac{\partial}{\partial \alpha_1} + \frac{1}{A_1A_2}\frac{\partial A_2}{\partial \alpha_1} & \frac{1}{A_2}\frac{\partial}{\partial \alpha_2} + \frac{1}{A_1A_2}\frac{\partial A_1}{\partial \alpha_2} & -1 \end{bmatrix} \tag{50}
$$

In the same way, by applying an integration-by-parts rule to the balance equations yields a set of expressions that are valid only at the boundaries of the two-dimensional physical domain $[\alpha_1^0, \alpha_1^1] \times [\alpha_2^0, \alpha_2^1]$ for any $\tau = 0, \ldots, N+1$. Thus, the natural boundary conditions at $\alpha_1 = \alpha_1^0$ or $\alpha_1 = \alpha_1^1$ are established:

$$
\begin{aligned}
N_1^{(\tau)\alpha_1} &= \overline{N}_1^{(\tau)\alpha_1} \quad \text{or} \quad u_1^{(\tau)} = \overline{u}_1^{(\tau)} \\
N_{12}^{(\tau)\alpha_2} &= \overline{N}_{12}^{(\tau)\alpha_2} \quad \text{or} \quad u_2^{(\tau)} = \overline{u}_2^{(\tau)} \\
T_1^{(\tau)\alpha_3} &= \overline{T}_1^{(\tau)\alpha_3} \quad \text{or} \quad u_3^{(\tau)} = \overline{u}_3^{(\tau)} \\
D_1^{(\tau)\alpha_4} &= \overline{D}_1^{(\tau)\alpha_4} \quad \text{or} \quad \phi^{(\tau)} = \overline{\phi}^{(\tau)} \\
H_1^{(\tau)\alpha_5} &= \overline{H}_1^{(\tau)\alpha_5} \quad \text{or} \quad \xi^{(\tau)} = \overline{\xi}^{(\tau)}
\end{aligned} \tag{51}
$$

On the other hand, the natural boundary conditions at $\alpha_2 = \alpha_2^0$ or $\alpha_2 =$

α_2^1 read as follows:

$$\begin{aligned}
&N_{21}^{(\tau)\alpha_1} = \overline{N}_{21}^{(\tau)\alpha_1} \quad \text{or} \quad u_1^{(\tau)} = \overline{u}_1^{(\tau)} \\
&N_{2}^{(\tau)\alpha_2} = \overline{N}_{2}^{(\tau)\alpha_2} \quad \text{or} \quad u_2^{(\tau)} = \overline{u}_2^{(\tau)} \\
&T_{2}^{(\tau)\alpha_3} = \overline{T}_{2}^{(\tau)\alpha_3} \quad \text{or} \quad u_3^{(\tau)} = \overline{u}_3^{(\tau)} \\
&D_{2}^{(\tau)\alpha_4} = \overline{D}_{2}^{(\tau)\alpha_4} \quad \text{or} \quad \phi^{(\tau)} = \overline{\phi}^{(\tau)} \\
&H_{2}^{(\tau)\alpha_5} = \overline{H}_{2}^{(\tau)\alpha_5} \quad \text{or} \quad \xi^{(\tau)} = \overline{\xi}^{(\tau)}
\end{aligned} \tag{52}$$

Note that the quantities $\overline{N}_1^{(\tau)\alpha_1}, \overline{N}_{12}^{(\tau)\alpha_2}, \overline{T}_1^{(\tau)\alpha_3}, \overline{D}_1^{(\tau)\alpha_4}, \overline{H}_1^{(\tau)\alpha_5}$ and $\overline{N}_{21}^{(\tau)\alpha_1}, \overline{N}_2^{(\tau)\alpha_2}, \overline{T}_2^{(\tau)\alpha_3}, \overline{D}_2^{(\tau)\alpha_4}, \overline{H}_2^{(\tau)\alpha_5}$, introduced in Eqn. (51) and Eqn. (52), represent the values of generalized secondary variables prescribed at the edges of the physical domain. In the same way, $\overline{u}_1^{(\tau)}, \overline{u}_2^{(\tau)}, \overline{u}_3^{(\tau)}, \overline{\phi}^{(\tau)}, \overline{\xi}^{(\tau)}$ are generalized configuration variables enforced at the boundaries of the structure. As a particular case, the Simply-supported (S) boundary condition is modelled using the following relations:

$$\begin{aligned}
&N_1^{(\tau)\alpha_1} = 0, \quad u_2^{(\tau)} = u_3^{(\tau)} = \phi^{(\tau)} = \xi^{(\tau)} = 0 \quad \text{at} \quad \alpha_1 = \alpha_1^0 \ \text{or} \ \alpha_1 = \alpha_1^1 \\
&N_2^{(\tau)\alpha_2} = 0, \quad u_1^{(\tau)} = u_3^{(\tau)} = \phi^{(\tau)} = \xi^{(\tau)} = 0 \quad \text{at} \quad \alpha_2 = \alpha_2^0 \ \text{or} \ \alpha_2 = \alpha_2^1
\end{aligned} \tag{53}$$

By substituting the generalized secondary variables vector with the higher-order constitutive relation from Eqn. (39), the final form of the fundamental governing equations for the present thermo-electro-elastic theory is derived, setting $\mathbf{L}^{(\tau\eta)}$ and $\mathbf{L}_f^{(\tau\eta)}$ for $\tau, \eta = 0, \ldots, N+1$ as the fundamental operators for the shell and the elastic foundation, respectively:

$$\sum_{\eta=0}^{N+1} \left(\mathbf{L}^{(\tau\eta)} - \mathbf{L}_f^{(\tau\eta)}\right)\boldsymbol{\delta}^{(\eta)} + \mathbf{q}^{(\tau)} = \mathbf{0} \tag{54}$$

In this way, the dependence of the fundamental relations on the unknown field variable vector $\boldsymbol{\delta}^{(\eta)}$ with $\eta = 0, \ldots, N+1$ is highlighted. The fundamental matrix $\mathbf{L}^{(\tau\eta)}$ and the elastic foundation matrix $\mathbf{L}_f^{(\tau\eta)}$ assume the following extended form:

$$\mathbf{L}^{(\tau\eta)} = \left[\begin{array}{ccc|c|c}
L_{11}^{(\tau\eta)\alpha_1\alpha_1} & L_{12}^{(\tau\eta)\alpha_1\alpha_2} & L_{13}^{(\tau\eta)\alpha_1\alpha_3} & L_{14}^{(\tau\eta)\alpha_1\alpha_4} & L_{15}^{(\tau\eta)\alpha_1\alpha_5} \\
L_{21}^{(\tau\eta)\alpha_2\alpha_1} & L_{22}^{(\tau\eta)\alpha_2\alpha_2} & L_{23}^{(\tau\eta)\alpha_2\alpha_3} & L_{24}^{(\tau\eta)\alpha_2\alpha_4} & L_{25}^{(\tau\eta)\alpha_2\alpha_5} \\
L_{31}^{(\tau\eta)\alpha_3\alpha_1} & L_{32}^{(\tau\eta)\alpha_3\alpha_2} & L_{33}^{(\tau\eta)\alpha_3\alpha_3} & L_{34}^{(\tau\eta)\alpha_3\alpha_4} & L_{35}^{(\tau\eta)\alpha_3\alpha_5} \\
L_{41}^{(\tau\eta)\alpha_4\alpha_1} & L_{42}^{(\tau\eta)\alpha_4\alpha_2} & L_{43}^{(\tau\eta)\alpha_4\alpha_3} & L_{44}^{(\tau\eta)\alpha_4\alpha_4} & L_{45}^{(\tau\eta)\alpha_4\alpha_5} \\
L_{51}^{(\tau\eta)\alpha_5\alpha_1} & L_{52}^{(\tau\eta)\alpha_5\alpha_2} & L_{53}^{(\tau\eta)\alpha_5\alpha_3} & L_{54}^{(\tau\eta)\alpha_5\alpha_4} & L_{55}^{(\tau\eta)\alpha_5\alpha_5}
\end{array}\right], \quad \mathbf{L}_f^{(\tau\eta)} = \left[\begin{array}{ccc|c|c}
L_{fm1}^{(\tau\eta)\alpha_1\alpha_1} & 0 & 0 & 0 & 0 \\
0 & L_{fm2}^{(\tau\eta)\alpha_2\alpha_2} & 0 & 0 & 0 \\
0 & 0 & L_{fm3}^{(\tau\eta)\alpha_3\alpha_3} & 0 & 0 \\
0 & 0 & 0 & 0 & 0 \\
0 & 0 & 0 & 0 & 0
\end{array}\right] \tag{55}$$

The elements $L_{ij}^{(\tau\eta)\alpha_i\alpha_j}$ with $i, j = 1, \ldots, 5$ of the fundamental operator $\mathbf{L}^{(\tau\eta)}$ are evaluated as follows [38]:

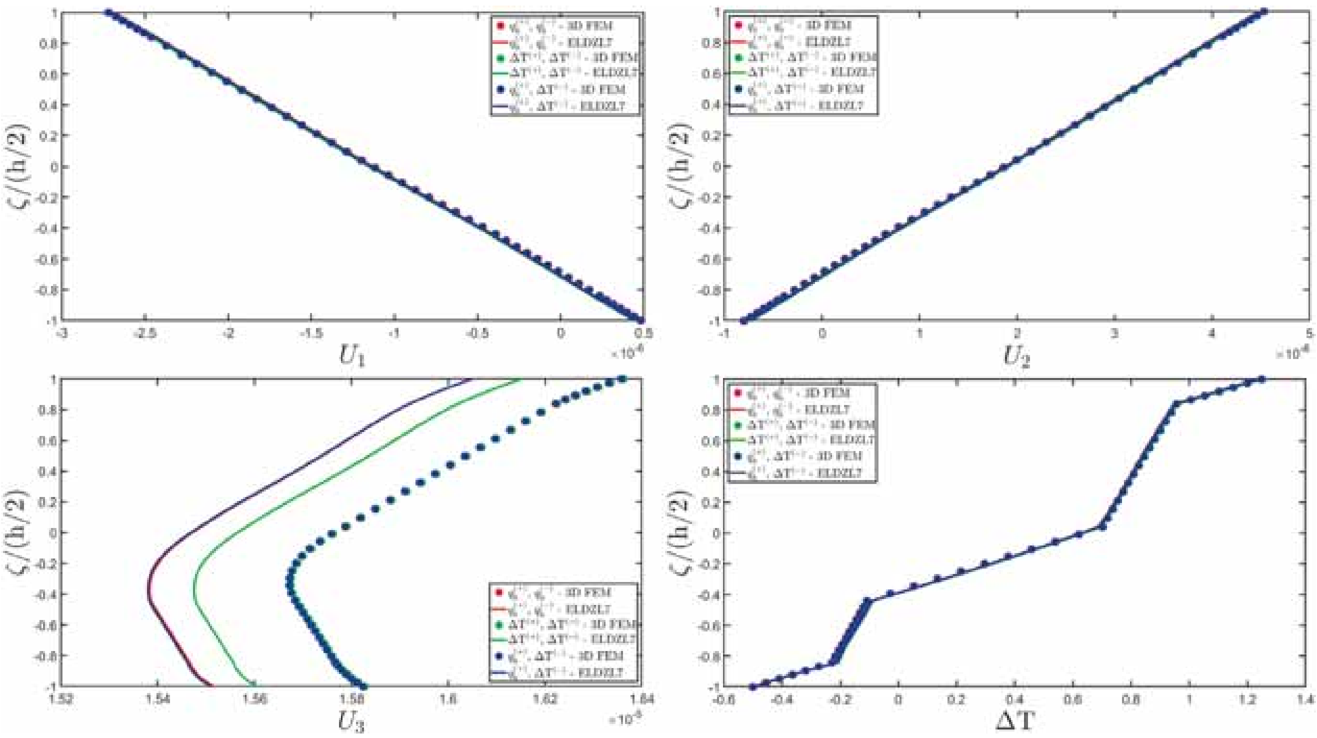

Fig. 2. Thermo-mechanical analysis of a laminated rectangular plate subjected to various sinusoidal thermal loading conditions with $\widetilde{N} = \widetilde{M} = 1$. Representation of the distributions along the thickness direction of the displacement field components U_1, U_2, U_3 and of the temperature variation ΔT with respect to the zero-stress reference configuration, expressed in [m] and [K], respectively. Thickness plots are provided for the point located at $(0.25L_1, 0.75L_2)$ within the two-dimensional physical domain.

$$\mathbf{L}^{(\tau\eta)} = \begin{bmatrix} \overline{\mathbf{D}}_{\Omega}^{*\alpha_1} \mathbf{A}_{\varepsilon\varepsilon}^{(\tau\eta)\alpha_1\alpha_1} \overline{\mathbf{D}}_{\Omega}^{\alpha_1} & \overline{\mathbf{D}}_{\Omega}^{*\alpha_1} \mathbf{A}_{\varepsilon\varepsilon}^{(\tau\eta)\alpha_1\alpha_2} \overline{\mathbf{D}}_{\Omega}^{\alpha_2} & \overline{\mathbf{D}}_{\Omega}^{*\alpha_1} \mathbf{A}_{\varepsilon\varepsilon}^{(\tau\eta)\alpha_1\alpha_3} \overline{\mathbf{D}}_{\Omega}^{\alpha_3} & | & \overline{\mathbf{D}}_{\Omega}^{*\alpha_1} \mathbf{A}_{\varepsilon\phi}^{(\tau\eta)\alpha_1\alpha_4} \overline{\mathbf{D}}_{\Omega}^{\alpha_4} & | & \overline{\mathbf{D}}_{\Omega}^{*\alpha_1} \mathbf{A}_{\varepsilon\mathrm{T}}^{(\tau\eta)\alpha_1\alpha_5} \overline{\mathbf{D}}_{\Omega}^{\alpha_5} \\ \overline{\mathbf{D}}_{\Omega}^{*\alpha_2} \mathbf{A}_{\varepsilon\varepsilon}^{(\tau\eta)\alpha_2\alpha_1} \overline{\mathbf{D}}_{\Omega}^{\alpha_1} & \overline{\mathbf{D}}_{\Omega}^{*\alpha_2} \mathbf{A}_{\varepsilon\varepsilon}^{(\tau\eta)\alpha_2\alpha_2} \overline{\mathbf{D}}_{\Omega}^{\alpha_2} & \overline{\mathbf{D}}_{\Omega}^{*\alpha_2} \mathbf{A}_{\varepsilon\varepsilon}^{(\tau\eta)\alpha_2\alpha_3} \overline{\mathbf{D}}_{\Omega}^{\alpha_3} & | & \overline{\mathbf{D}}_{\Omega}^{*\alpha_2} \mathbf{A}_{\varepsilon\phi}^{(\tau\eta)\alpha_2\alpha_4} \overline{\mathbf{D}}_{\Omega}^{\alpha_4} & | & \overline{\mathbf{D}}_{\Omega}^{*\alpha_2} \mathbf{A}_{\varepsilon\mathrm{T}}^{(\tau\eta)\alpha_2\alpha_5} \overline{\mathbf{D}}_{\Omega}^{\alpha_5} \\ \overline{\mathbf{D}}_{\Omega}^{*\alpha_3} \mathbf{A}_{\varepsilon\varepsilon}^{(\tau\eta)\alpha_3\alpha_1} \overline{\mathbf{D}}_{\Omega}^{\alpha_1} & \overline{\mathbf{D}}_{\Omega}^{*\alpha_3} \mathbf{A}_{\varepsilon\varepsilon}^{(\tau\eta)\alpha_3\alpha_2} \overline{\mathbf{D}}_{\Omega}^{\alpha_2} & \overline{\mathbf{D}}_{\Omega}^{*\alpha_3} \mathbf{A}_{\varepsilon\varepsilon}^{(\tau\eta)\alpha_3\alpha_3} \overline{\mathbf{D}}_{\Omega}^{\alpha_3} & | & \overline{\mathbf{D}}_{\Omega}^{*\alpha_3} \mathbf{A}_{\varepsilon\phi}^{(\tau\eta)\alpha_3\alpha_4} \overline{\mathbf{D}}_{\Omega}^{\alpha_4} & | & \overline{\mathbf{D}}_{\Omega}^{*\alpha_3} \mathbf{A}_{\varepsilon\mathrm{T}}^{(\tau\eta)\alpha_3\alpha_5} \overline{\mathbf{D}}_{\Omega}^{\alpha_5} \\ \overline{\mathbf{D}}_{\Omega}^{*\alpha_4} \mathbf{A}_{\phi\varepsilon}^{(\tau\eta)\alpha_4\alpha_1} \overline{\mathbf{D}}_{\Omega}^{\alpha_1} & \overline{\mathbf{D}}_{\Omega}^{*\alpha_4} \mathbf{A}_{\phi\varepsilon}^{(\tau\eta)\alpha_4\alpha_2} \overline{\mathbf{D}}_{\Omega}^{\alpha_2} & \overline{\mathbf{D}}_{\Omega}^{*\alpha_4} \mathbf{A}_{\phi\varepsilon}^{(\tau\eta)\alpha_4\alpha_3} \overline{\mathbf{D}}_{\Omega}^{\alpha_3} & | & \overline{\mathbf{D}}_{\Omega}^{*\alpha_4} \mathbf{A}_{\phi\phi}^{(\tau\eta)\alpha_4\alpha_4} \overline{\mathbf{D}}_{\Omega}^{\alpha_4} & | & \overline{\mathbf{D}}_{\Omega}^{*\alpha_4} \mathbf{A}_{\phi\mathrm{T}}^{(\tau\eta)\alpha_4\alpha_5} \overline{\mathbf{D}}_{\Omega}^{\alpha_5} \\ 0 & 0 & 0 & | & 0 & | & \overline{\mathbf{D}}_{\Omega}^{*\alpha_5} \mathbf{A}_{\theta\theta}^{(\tau\eta)\alpha_5\alpha_5} \overline{\mathbf{D}}_{\Omega}^{\alpha_5} \end{bmatrix} \tag{56}$$

Employing the curvilinear parametrization of the shell, defined by the curvilinear abscissa $s_i = s_1, s_2$ in Eqn. (5), the unknown variables are expanded using the trigonometric Fourier series as follows:

$$\begin{aligned} u_1^{(\tau)}(s_1,s_2) &= \sum_{n=1}^{\widetilde{N}} \sum_{m=1}^{\widetilde{M}} \mathrm{U}_{1nm}^{(\tau)} \cos\left(\frac{n\pi}{L_1}s_1\right) \sin\left(\frac{m\pi}{L_2}s_2\right) \\ u_2^{(\tau)}(s_1,s_2) &= \sum_{n=1}^{\widetilde{N}} \sum_{m=1}^{\widetilde{M}} \mathrm{U}_{2nm}^{(\tau)} \sin\left(\frac{n\pi}{L_1}s_1\right) \cos\left(\frac{m\pi}{L_2}s_2\right) \\ u_3^{(\tau)}(s_1,s_2) &= \sum_{n=1}^{\widetilde{N}} \sum_{m=1}^{\widetilde{M}} \mathrm{U}_{3nm}^{(\tau)} \sin\left(\frac{n\pi}{L_1}s_1\right) \sin\left(\frac{m\pi}{L_2}s_2\right) \\ \phi^{(\tau)}(s_1,s_2) &= \sum_{n=1}^{\widetilde{N}} \sum_{m=1}^{\widetilde{M}} \Phi_{nm}^{(\tau)} \sin\left(\frac{n\pi}{L_1}s_1\right) \sin\left(\frac{m\pi}{L_2}s_2\right) \\ \xi^{(\tau)}(s_1,s_2) &= \sum_{n=1}^{\widetilde{N}} \sum_{m=1}^{\widetilde{M}} \Xi_{nm}^{(\tau)} \sin\left(\frac{n\pi}{L_1}s_1\right) \sin\left(\frac{m\pi}{L_2}s_2\right) \end{aligned} \tag{57}$$

where $\widetilde{N} = \widetilde{M} = +\infty$. In this way, the differential equations system (54) is reduced to an algebraic linear system, with the unknown variables arranged in the vector $\boldsymbol{U}_{nm}^{(\tau)} = \begin{bmatrix} \mathrm{U}_{1nm}^{(\tau)} & \mathrm{U}_{2nm}^{(\tau)} & \mathrm{U}_{3nm}^{(\tau)} & \Phi_{nm}^{(\tau)} & \Xi_{nm}^{(\tau)} \end{bmatrix}^T$ for each $\tau = 0, \ldots, N+1$ and n, m. In the same way, the following expressions are assumed for the generalized surface actions of Eqn. (45):

$$\begin{aligned} q_1^{(\tau)}(s_1,s_2) &= \sum_{n=1}^{\widetilde{N}} \sum_{m=1}^{\widetilde{M}} Q_{1snm}^{(\tau)} \cos\left(\frac{n\pi}{L_1}s_1\right) \sin\left(\frac{m\pi}{L_2}s_2\right) \\ q_2^{(\tau)}(s_1,s_2) &= \sum_{n=1}^{\widetilde{N}} \sum_{m=1}^{\widetilde{M}} Q_{2snm}^{(\tau)} \sin\left(\frac{n\pi}{L_1}s_1\right) \cos\left(\frac{m\pi}{L_2}s_2\right) \\ q_3^{(\tau)}(s_1,s_2) &= \sum_{n=1}^{\widetilde{N}} \sum_{m=1}^{\widetilde{M}} Q_{3snm}^{(\tau)} \sin\left(\frac{n\pi}{L_1}s_1\right) \sin\left(\frac{m\pi}{L_2}s_2\right) \\ q_{\mathrm{D}}^{(\tau)}(s_1,s_2) &= \sum_{n=1}^{\widetilde{N}} \sum_{m=1}^{\widetilde{M}} Q_{\mathrm{D}snm}^{(\tau)} \sin\left(\frac{n\pi}{L_1}s_1\right) \sin\left(\frac{m\pi}{L_2}s_2\right) \\ q_h^{(\tau)}(s_1,s_2) &= \sum_{n=1}^{\widetilde{N}} \sum_{m=1}^{\widetilde{M}} Q_{\mathrm{T}snm}^{(\tau)} \sin\left(\frac{n\pi}{L_1}s_1\right) \sin\left(\frac{m\pi}{L_2}s_2\right) \end{aligned} \tag{58}$$

The coefficients $Q_{\alpha snm}^{(\tau)}$ with $\alpha = 1, 2, 3, \mathrm{D}, \mathrm{T}$ are computed using the relation reported below and are conveniently arranged in vector $\mathbf{Q}_{snm}^{(\tau)} = \begin{bmatrix} Q_{1snm}^{(\tau)} & Q_{2snm}^{(\tau)} & Q_{3snm}^{(\tau)} & Q_{\mathrm{D}snm}^{(\tau)} & Q_{\mathrm{T}snm}^{(\tau)} \end{bmatrix}^T$ for each wave number n, m,:

$$\begin{aligned} Q_{1snm}^{(\tau)} &= Q_{1snm}^{(-)} F_\tau^{(1)\alpha_1(-)} H_1^{(-)} H_2^{(-)} + Q_{1snm}^{(+)} F_\tau^{(l)\alpha_1(+)} H_1^{(+)} H_2^{(+)} \\ Q_{2snm}^{(\tau)} &= Q_{2snm}^{(-)} F_\tau^{(1)\alpha_2(-)} H_1^{(-)} H_2^{(-)} + Q_{2snm}^{(+)} F_\tau^{(l)\alpha_2(+)} H_1^{(+)} H_2^{(+)} \\ Q_{3snm}^{(\tau)} &= Q_{3snm}^{(-)} F_\tau^{(1)\alpha_3(-)} H_1^{(-)} H_2^{(-)} + Q_{3snm}^{(+)} F_\tau^{(l)\alpha_3(+)} H_1^{(+)} H_2^{(+)} \\ Q_{\mathrm{D}snm}^{(\tau)} &= Q_{\mathrm{D}snm}^{(-)} F_\tau^{(1)\alpha_4(-)} H_1^{(-)} H_2^{(-)} + Q_{\mathrm{D}snm}^{(+)} F_\tau^{(l)\alpha_4(+)} H_1^{(+)} H_2^{(+)} \\ Q_{\mathrm{T}snm}^{(\tau)} &= Q_{\mathrm{T}snm}^{(-)} F_\tau^{(1)\alpha_5(-)} H_1^{(-)} H_2^{(-)} + Q_{\mathrm{T}snm}^{(+)} F_\tau^{(l)\alpha_5(+)} H_1^{(+)} H_2^{(+)} \end{aligned} \tag{59}$$

Here, $Q_{\alpha snm}^{(-)}$ and $Q_{\alpha snm}^{(+)}$ with $\alpha = 1, 2, 3, \mathrm{D}, \mathrm{T}$ represent the magnitudes of the generalized surface actions applied at the top and bottom sides of the panel, respectively.

A closed-form semi-analytical Navier solution can be derived only for geometries with uniform Lamé parameters $A_i = A_1, A_2$ and constant principal radii of curvature $R_i = R_1, R_2$ throughout the entire physical domain. In other words, the differential relations from Eqn. (6) are assumed. In addition, the following material assumption must be adopted:

$$\begin{aligned} \overline{\boldsymbol{\Gamma}}_{\mathrm{C}}^{(k)} &= \begin{bmatrix} \overline{C}_{11}^{(k)} & \overline{C}_{12}^{(k)} & 0 & 0 & 0 & \overline{C}_{13}^{(k)} \\ \overline{C}_{12}^{(k)} & \overline{C}_{22}^{(k)} & 0 & 0 & 0 & \overline{C}_{23}^{(k)} \\ 0 & 0 & \overline{C}_{66}^{(k)} & 0 & 0 & 0 \\ 0 & 0 & 0 & \overline{C}_{44}^{(k)} & 0 & 0 \\ 0 & 0 & 0 & 0 & \overline{C}_{55}^{(k)} & 0 \\ \overline{C}_{13}^{(k)} & \overline{C}_{23}^{(k)} & 0 & 0 & 0 & \overline{C}_{33}^{(k)} \end{bmatrix}, \quad \overline{\boldsymbol{\Gamma}}_{\mathrm{L}}^{(k)} \\ &= \begin{bmatrix} \overline{l}_{11}^{(k)} & 0 & 0 \\ 0 & \overline{l}_{22}^{(k)} & 0 \\ 0 & 0 & \overline{l}_{33}^{(k)} \end{bmatrix}, \quad \overline{\boldsymbol{\Gamma}}_{\mathrm{K}}^{(k)} = \begin{bmatrix} \overline{k}_{11}^{(k)} & 0 & 0 \\ 0 & \overline{k}_{22}^{(k)} & 0 \\ 0 & 0 & \overline{k}_{33}^{(k)} \end{bmatrix} \overline{\boldsymbol{\Gamma}}_{\mathrm{P}}^{(k)} \\ &= \begin{bmatrix} 0 & 0 & 0 & \overline{p}_{14}^{(k)} & 0 & 0 \\ 0 & 0 & 0 & 0 & \overline{p}_{25}^{(k)} & 0 \\ \overline{p}_{31}^{(k)} & \overline{p}_{32}^{(k)} & 0 & 0 & 0 & \overline{p}_{33}^{(k)} \end{bmatrix} \overline{\boldsymbol{\Gamma}}_{\mathrm{z}}^{(k)} \\ &= \begin{bmatrix} \overline{z}_{11}^{(k)} & \overline{z}_{22}^{(k)} & 0 & 0 & 0 & \overline{z}_{33}^{(k)} \end{bmatrix}, \quad \overline{\boldsymbol{\Gamma}}_{\mathrm{TT}}^{(k)} = \begin{bmatrix} \overline{\xi}_{11}^{(k)} \end{bmatrix} \end{aligned} \tag{60}$$

As can be seen, the selected material behavior depends on the cross-ply lamination schemes. More specifically, it is assumed that an arbitrary $k-$th layer of the stacking sequence is orthotropic, with the material orientation angle $\vartheta^{(k)}$ equal to 0 or $\pm\pi/2$. Based on the geometry assumptions (6), together with the kinematic (57), loading (58), and material (60) assumptions, the differential system (54) is reduced to a linear algebraic system with an infinite number of terms, which is presented below in compact form [38]:

$$\sum_{n=1}^{\widetilde{N}} \sum_{m=1}^{\widetilde{M}} \left(\sum_{\eta=0}^{N+1} \left(\widetilde{\mathbf{L}}_{nm}^{(\tau\eta)} - \widetilde{\mathbf{L}}_{fnm}^{(\tau\eta)} \right) \boldsymbol{U}_{nm}^{(\eta)} + \mathbf{Q}_{snm}^{(\tau)} \right) = \mathbf{0} \tag{61}$$

with $\widetilde{N} = \widetilde{M} = +\infty$. Semi-analytical solutions are obtained by assigning real values to parameters $\widetilde{N}, \widetilde{M}$. The semi-analytical matrices $\widetilde{\mathbf{L}}_{nm}^{(\tau\eta)}$ and $\widetilde{\mathbf{L}}_{fnm}^{(\tau\eta)}$ take the following extended form for any n, m:

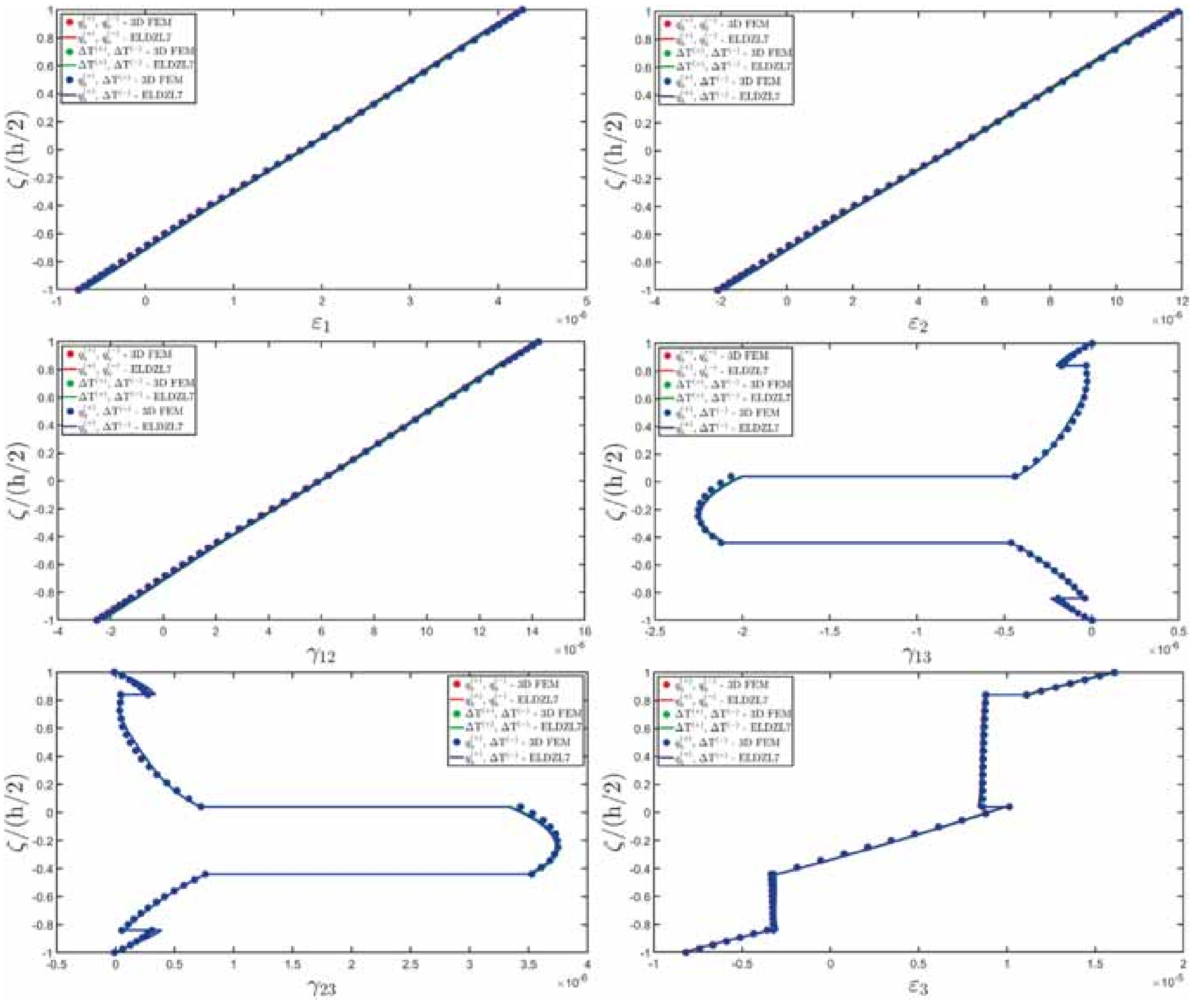

Fig. 3. Thermo-mechanical analysis of a laminated rectangular plate subjected to various sinusoidal thermal loading conditions with $\widetilde{N} = \widetilde{M} = 1$. Representation of the distributions along the thickness direction of the components of the three-dimensional strain vector $\boldsymbol{\varepsilon}(\alpha_1, \alpha_2, \zeta)$, expressed in $[\mathrm{m/m}]$. Thickness plots are provided for the point located at $(0.25L_1, 0.75L_2)$ within the two-dimensional physical domain.

$$\widetilde{\mathbf{L}}_{nm}^{(\tau\eta)} = \left[\begin{array}{ccc|c|c} \widetilde{L}_{11nm}^{(\tau\eta)\alpha_1\alpha_1} & \widetilde{L}_{12nm}^{(\tau\eta)\alpha_1\alpha_2} & \widetilde{L}_{13nm}^{(\tau\eta)\alpha_1\alpha_3} & \widetilde{L}_{14nm}^{(\tau\eta)\alpha_1\alpha_4} & \widetilde{L}_{15nm}^{(\tau\eta)\alpha_1\alpha_5} \\ \widetilde{L}_{21nm}^{(\tau\eta)\alpha_2\alpha_1} & \widetilde{L}_{22nm}^{(\tau\eta)\alpha_2\alpha_2} & \widetilde{L}_{23nm}^{(\tau\eta)\alpha_2\alpha_3} & \widetilde{L}_{24nm}^{(\tau\eta)\alpha_2\alpha_4} & \widetilde{L}_{25nm}^{(\tau\eta)\alpha_2\alpha_5} \\ \widetilde{L}_{31nm}^{(\tau\eta)\alpha_3\alpha_1} & \widetilde{L}_{32nm}^{(\tau\eta)\alpha_3\alpha_2} & \widetilde{L}_{33nm}^{(\tau\eta)\alpha_3\alpha_3} & \widetilde{L}_{34nm}^{(\tau\eta)\alpha_3\alpha_4} & \widetilde{L}_{35nm}^{(\tau\eta)\alpha_3\alpha_5} \\ \widetilde{L}_{41nm}^{(\tau\eta)\alpha_4\alpha_1} & \widetilde{L}_{42nm}^{(\tau\eta)\alpha_4\alpha_2} & \widetilde{L}_{43nm}^{(\tau\eta)\alpha_4\alpha_3} & \widetilde{L}_{44nm}^{(\tau\eta)\alpha_4\alpha_4} & \widetilde{L}_{45nm}^{(\tau\eta)\alpha_4\alpha_5} \\ \widetilde{L}_{51nm}^{(\tau\eta)\alpha_5\alpha_1} & \widetilde{L}_{52nm}^{(\tau\eta)\alpha_5\alpha_2} & \widetilde{L}_{53nm}^{(\tau\eta)\alpha_5\alpha_3} & \widetilde{L}_{54nm}^{(\tau\eta)\alpha_5\alpha_4} & \widetilde{L}_{55nm}^{(\tau\eta)\alpha_5\alpha_5} \end{array}\right], \quad \widetilde{\mathbf{L}}_{fnm}^{(\tau\eta)} = \left[\begin{array}{ccc|c|c} \widetilde{L}_{11fnm}^{(\tau\eta)\alpha_1\alpha_1} & 0 & 0 & 0 & 0 \\ 0 & \widetilde{L}_{22fnm}^{(\tau\eta)\alpha_2\alpha_2} & 0 & 0 & 0 \\ 0 & 0 & \widetilde{L}_{33fnm}^{(\tau\eta)\alpha_3\alpha_3} & 0 & 0 \\ 0 & 0 & 0 & 0 & 0 \\ 0 & 0 & 0 & 0 & 0 \end{array}\right] \tag{62}$$

In Appendix II, the reader can find the complete expression for elements $\widetilde{L}_{ijnm}^{(\tau\eta)\alpha_i\alpha_j}$ with $i,j = 1, \ldots, 5$ of the matrix $\widetilde{\mathbf{L}}_{nm}^{(\tau\eta)}$ and $\widetilde{L}_{\beta\beta nm}^{(\tau\eta)\alpha_\beta\alpha_\beta}$ with $\beta = 1,2,3$ of the matrix $\widetilde{\mathbf{L}}_{fnm}^{(\tau\eta)}$, as detailed in Eqn. (62).

3. Generalized differential Quadrature method

In this section we present the main basics of the GDQ method, as here adopted to compute the partial derivatives of geometric and mechanical quantities. One key aspect of the numerical procedure consists on the definition of a rectangular computational grid, from the two-dimensional physical domain. To this end, the following distribution of I_Q sample points is adopted [81], corresponding to the reference interval $[-1, 1]$:

$$\overline{x}_i = -\cos\left(\frac{i-1}{I_Q - 1}\pi\right) \tag{63}$$

The following coordinate transformation is employed to discretize an arbitrary one-dimensional definition domain $[a, b]$:

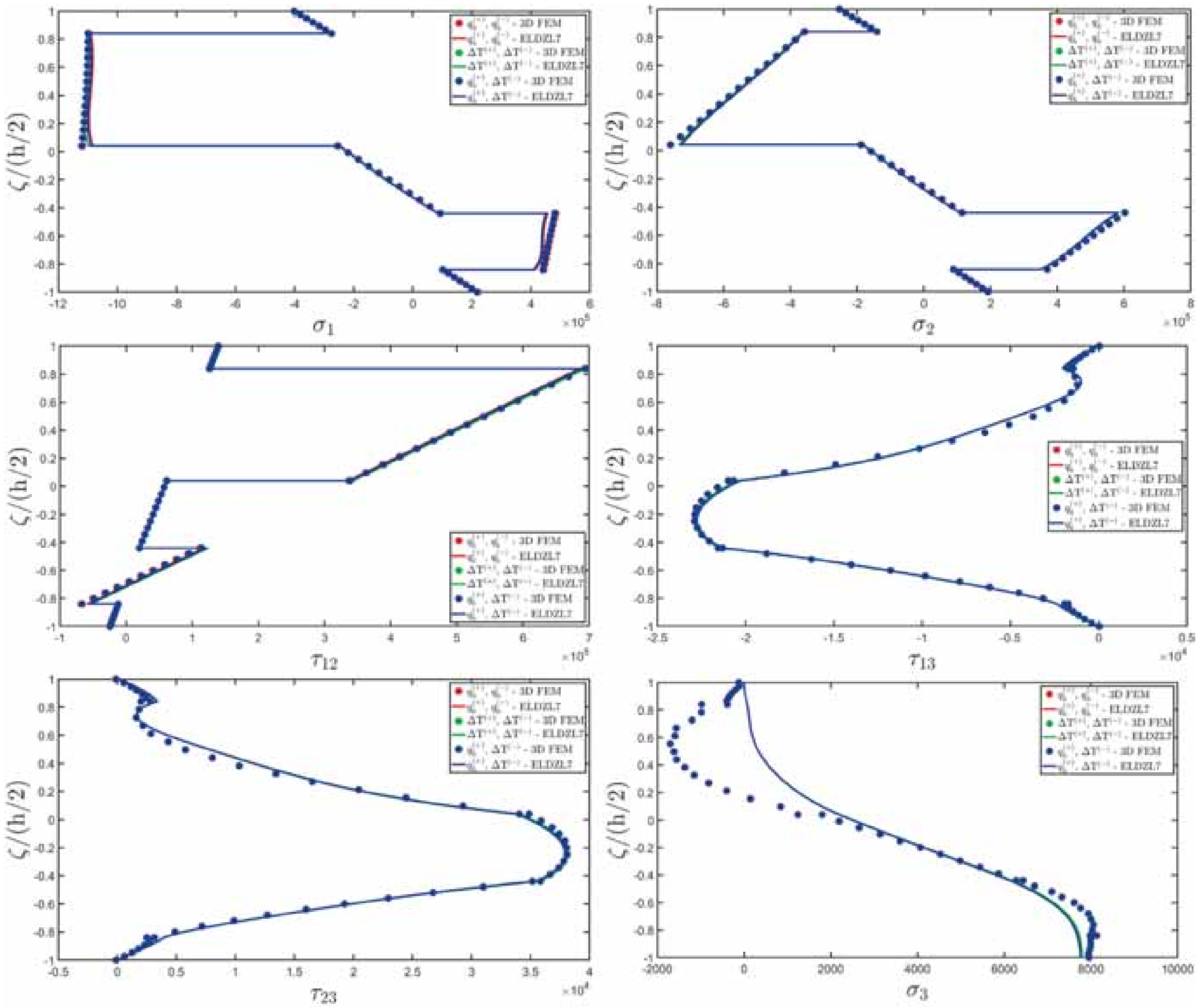

Fig. 4. Thermo-mechanical analysis of a laminated rectangular plate subjected to various sinusoidal thermal loading conditions with $\widetilde{N} = \widetilde{M} = 1$. Representation of the distributions along the thickness direction of the components of the three-dimensional stress vector $\boldsymbol{\sigma}(\alpha_1, \alpha_2, \zeta)$, expressed in $[\mathrm{N/m^2}]$. Thickness plots are provided for the point located at $(0.25L_1, 0.75L_2)$ within the two-dimensional physical domain.

$$x_i = \frac{x_{I_Q} - x_1}{\bar{x}_{I_Q} - \bar{x}_1}(\bar{x}_i - \bar{x}_1) + x_1 \tag{64}$$

Following the GDQ method, an arbitrary n–th order derivative of a function $f = f(x)$ with $x \in [a, b]$ is evaluated at a discrete point x_i, with $i = 1, \ldots, I_Q$ using the following expression [81]:

$$f^{(n)}(x_i) = \left.\frac{\partial^n f(x)}{\partial x^n}\right|_{x=x_i} \cong \sum_{j=1}^{I_Q} \varsigma_{ij}^{(n)} f(x_j) \tag{65}$$

Here, $f(x_j)$ represents the value of the function at the j–th point of the grid for $j = 1, \ldots, I_Q$, while $\varsigma_{ij}^{(n)}$ with $i, j = 1, \ldots, I_Q$ are the quadrature coefficients for the n–th order derivative, which are recursively computed as follows:

$$\begin{aligned} &\varsigma_{ij}^{(1)} = \frac{\mathscr{L}^{(1)}(x_i)}{(x_i - x_j)\mathscr{L}^{(1)}(x_j)}, \quad \varsigma_{ij}^{(n)} = n\left(\varsigma_{ij}^{(1)}\varsigma_{ii}^{(n-1)} - \frac{\varsigma_{ij}^{(n-1)}}{x_i - x_j}\right) && i \neq j \\ &\varsigma_{ii}^{(n)} = -\sum\nolimits_{j=1,\ j\neq i}^{I_Q} \varsigma_{ij}^{(n)} && i = j \end{aligned} \tag{66}$$

Note that in the previous relation, the position $\varsigma_{ij}^{(0)} = \delta_{ij}$ is adopted, where δ_{ij} for $i, j = 1, \ldots, I_Q$ is the Kronecker-delta operator. On the other hand, $\mathscr{L}^{(1)}(x_i)$ and $\mathscr{L}^{(1)}(x_j)$ are the first-order derivatives of the Lagrange interpolating polynomials at two arbitrary discrete points x_i and x_j, respectively. The GDQ coefficients (66) are arranged in the matrix $\varsigma^{(n)}$ of size $I_Q \times I_Q$. If the sample points are distributed according to Eqn. (63), the GDQ coefficients, denoted by $\widetilde{\varsigma}_{ij}^{(n)}$, must be transformed from the interval $[-1, 1]$ to $[a, b]$ using the coordinate transformation given in Eqn. (64). This gets to the following relation [81]:

$$\varsigma_{ij}^{(n)} = \left(\frac{\bar{x}_{I_Q} - \bar{x}_1}{x_{I_Q} - x_1}\right)^n \widetilde{\varsigma}_{ij}^{(n)} \tag{67}$$

Numerical integrations required for computing the generalized stiffness coefficients $A_{rsnm\ (pq)}^{(\tau\eta)[fg]\ \alpha_i\alpha_j}$ of Eqn. (36) are performed with the T-GIQ method. For an arbitrary function $f = f(x)$ with $x \in [a, b]$, the following quadrature relation is used:

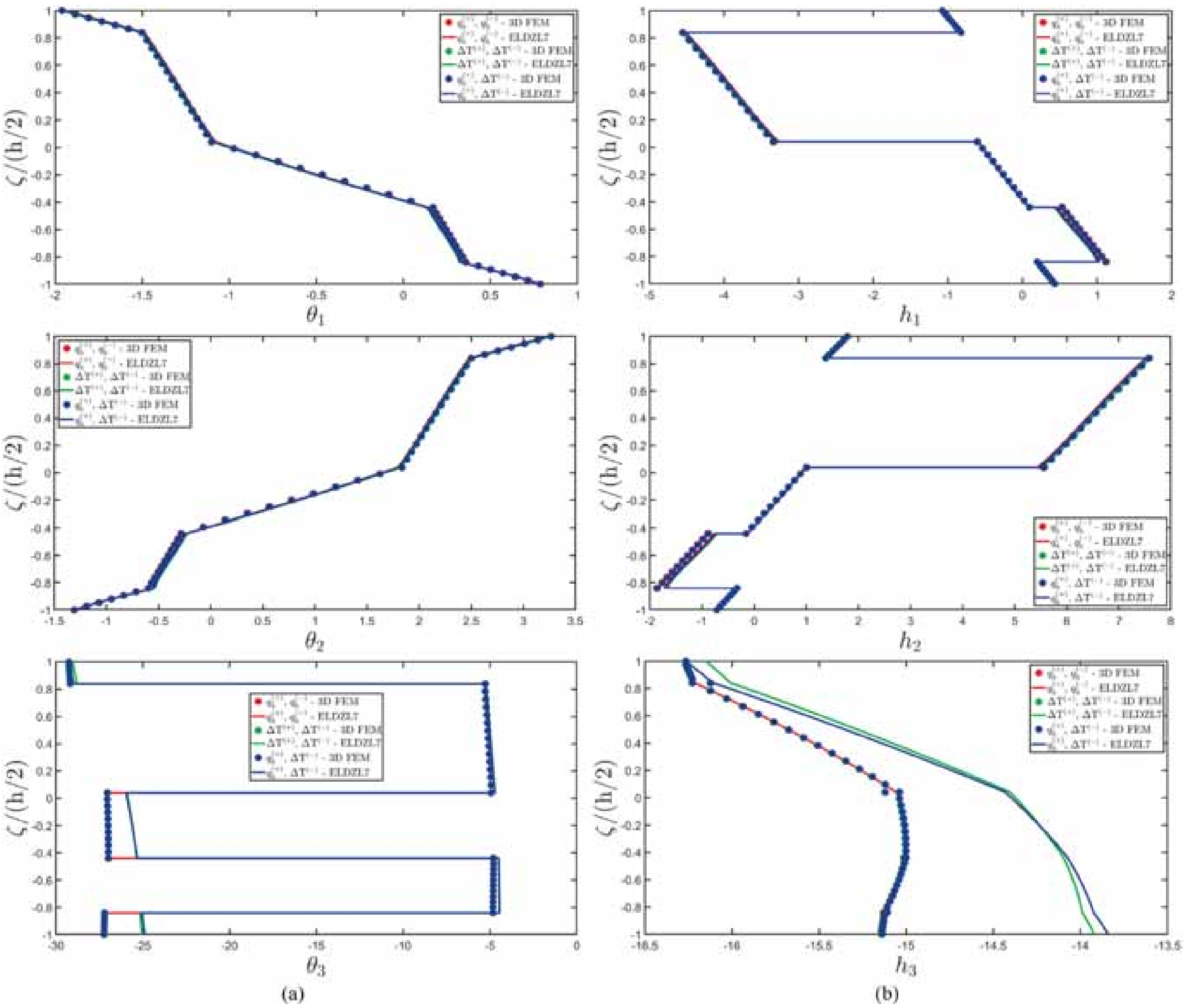

Fig. 5. Thermo-mechanical analysis of a laminated rectangular plate subjected to various sinusoidal thermal loading conditions with $\widetilde{N} = \widetilde{M} = 1$. Representation of the distributions along the thickness direction of the components of the three-dimensional temperature gradient vector $\boldsymbol{\theta}(\alpha_1, \alpha_2, \zeta)$ (a), expressed in $[\mathrm{K/m}]$ and of the thermal flux vector $\boldsymbol{h}(\alpha_1, \alpha_2, \zeta)$ (b), expressed in $[\mathrm{J/m}^2]$. Thickness plots are provided for the point located at $(0.25L_1, 0.75L_2)$ within the two-dimensional physical domain.

$$\int_{x_i}^{x_j} f(x)dx = \int_{x_i}^{\frac{x_j+x_i}{2}} f(x)dx - \int_{x_j}^{\frac{x_j+x_i}{2}} f(x)dx = \sum_{k=1}^{I_Q} w_k^{ij} f(x_k) \tag{68}$$

where the integration interval is defined so that $[x_i, x_j] \subseteq [a, b]$, and w_k^{ij} with $k = 1, \ldots, I_Q$ are the T-GIQ coefficients. By expanding function f through the Taylor's series of $m-$th order near the lower and upper bounds of the intervals, Eqn. (68) can be expressed as follows [81]:

$$\begin{aligned}\int_{x_i}^{x_j} f(x)dx &= \sum_{r=0}^{m-1} \frac{(x_j - x_i)^{r+1}}{2^{r+1}(r+1)!} \left.\frac{d^r f}{dx^r}\right|_{x_i} - \sum_{r=0}^{m-1} \frac{(x_i - x_j)^{r+1}}{2^{r+1}(r+1)!} \left.\frac{d^r f}{dx^r}\right|_{x_j} \\ &= \sum_{r=0}^{m-1} \frac{(x_j - x_i)^{r+1}}{2^{r+1}(r+1)!} \left(\left.\frac{d^r f}{dx^r}\right|_{x_i} + (-1)^{r+2} \left.\frac{d^r f}{dx^r}\right|_{x_j} \right)\end{aligned} \tag{69}$$

By applying the GDQ rule (65) to discretize the $r-$th order derivative of the function f, with $r = 0, \ldots, m-1$, the previous relation takes the following form, and it enables the definition of the T-GIQ weighting coefficients w_k^{ij}:

$$\begin{aligned}\int_{x_i}^{x_j} f(x)dx &= \sum_{r=0}^{m-1} \frac{(x_j - x_i)^{r+1}}{2^{r+1}(r+1)!} \sum_{k=1}^{I_Q} \varsigma_{ik}^{(r)} f(x_k) - \sum_{r=0}^{m-1} \frac{(x_i - x_j)^{r+1}}{2^{r+1}(r+1)!} \sum_{k=1}^{I_Q} \varsigma_{jk}^{(r)} f(x_k) = \\ &= \sum_{k=1}^{I_Q} \left(\sum_{r=0}^{m-1} \left(\frac{(x_j - x_i)^{r+1}}{2^{r+1}(r+1)!} \varsigma_{ik}^{(r)} + \frac{(x_i - x_j)^{r+1}}{2^{r+1}(r+1)!} \varsigma_{jk}^{(r)} \right) \right) f(x_k) = \\ &= \sum_{k=1}^{I_Q} \left(\sum_{r=0}^{m-1} \frac{(x_j - x_i)^{r+1}}{2^{r+1}(r+1)!} \left(\varsigma_{ik}^{(r)} + (-1)^{r+2} \varsigma_{jk}^{(r)} \right) \right) f(x_k) = \sum_{k=1}^{I_Q} w_k^{ij} f(x_k)\end{aligned} \tag{70}$$

4. Recovery of primary and secondary variables

An effective procedure for recovering the three-dimensional response of a doubly-curved shell panel is outlined, starting from the two-dimensional solution of the fundamental equations (54), which are derived from the semi-analytical Navier procedure (61). The main issue consists of defining a discrete grid along the thickness direction of the shell, spanning from the bottom to the top side of the structure. To this

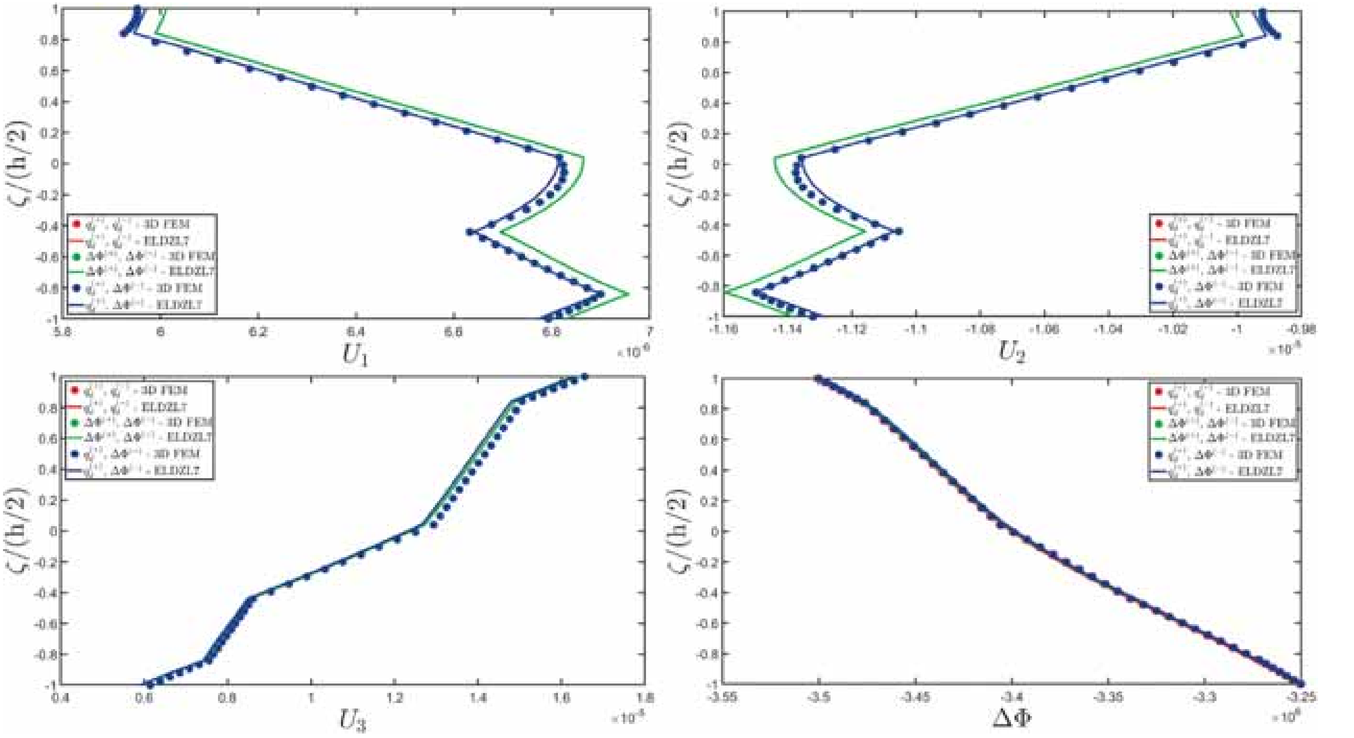

Fig. 6. Electro-mechanical analysis of a laminated rectangular plate subjected to various sinusoidal thermal loading conditions with $\widetilde{N} = \widetilde{M} = 1$. Representation of the distributions along the thickness direction of the displacement field components U_1, U_2, U_3 and of the electric potential variation $\Delta\phi$ with respect to the zero-stress reference configuration, expressed in [m] and [V], respectively. Thickness plots are provided for the point located at $(0.25L_1, 0.75L_2)$ within the two-dimensional physical domain.

end, a non-uniform grid is identified within each k−th lamina of the stacking sequence, as already introduced in Eqn. (64) with I_T sample points. Each lamina is characterized by the closed interval $[\zeta_k, \zeta_{k+1}]$, where ζ_k and ζ_{k+1} refer to the extremities of the lamina, as specified in Eqn. (8). A vector $\boldsymbol{\zeta}^{(k)} = \left[\zeta_1^{(k)} \ \cdots \ \zeta_{\widetilde{m}}^{(k)} \ \cdots \ \zeta_{I_T}^{(k)}\right]^T$ of size $I_T \times 1$ is used to collect these grid points. Since the structure consists of l superimposed laminae, an assembly procedure is employed to form the vector $\boldsymbol{\zeta} = \left[\boldsymbol{\zeta}^{(1)T} \ \cdots \ \boldsymbol{\zeta}^{(k)T} \ \cdots \ \boldsymbol{\zeta}^{(l)T}\right]$ of size $lI_T \times 1$ where each element is denoted by ζ_m with $m = (k-1)I_T + \widetilde{m}$ representing the $\widetilde{m}$−th grid point in the k−th lamina [61]. It should be noted that in the vector $\boldsymbol{\zeta}$, the sampling points $\zeta_{I_T}^{(k)} = \zeta_{kI_T}$ and $\zeta_1^{(k+1)} = \zeta_{(k+1)1}$ for $k = 1, \ldots, l-1$ are located at the same height, corresponding to the interface between adjacent laminae in the stacking sequence. At this point, Eqn. (9) is used to derive the three-dimensional configuration variables at point $(s_{1i}, s_{2j}, \zeta_m)$ with $i = 1,\ldots,I_N$, $j = 1,\ldots,I_M$ and $m = 1,\ldots,lI_T$, which are assembled into the vector $\boldsymbol{\Delta}_{(ijm)}^{(k)}$:

$$\boldsymbol{\Delta}_{(ijm)}^{(k)} = \sum_{\tau=0}^{N+1} \mathbf{F}_{\tau(m)}^{(k)} \boldsymbol{\delta}_{(ij)}^{(\tau)} \tag{71}$$

Here, the vector $\mathbf{F}_{\tau(m)}^{(k)}$ contains the values of the thickness functions set (9) at the height ζ_m, while the vector $\boldsymbol{\delta}_{(ij)}^{(\tau)}$ accounts for the generalized configuration variables associated with an arbitrary τ−th kinematic expansion order for point (s_{1i}, s_{2j}) in the physical domain. In the same way, Eqn. (21) is used to compute the three-dimensional primary variables by expressing the vector $\boldsymbol{\pi}^{(\tau)\alpha_i}$ in terms of $\boldsymbol{\delta}_{(ij)}^{(\tau)}$:

$$\boldsymbol{\pi}_{(ijm)}^{(k)} = \sum_{\tau=0}^{N+1} \sum_{i=1}^{5} \mathbf{Z}_{(ijm)}^{(k\tau)\alpha_i} \boldsymbol{\pi}_{(ij)}^{(\tau)\alpha_i} \tag{72}$$

where $\mathbf{Z}_{(ijm)}^{(k\tau)\alpha_i}$ is the discrete version of the operator $\mathbf{Z}^{(k\tau)\alpha_i}$ from Eqn. (21). The three-dimensional strain components of Eqn. (72) are then used to compute in-plane three-dimensional secondary variables using the constitutive relation given in Eqn. (24):

$$\begin{aligned}
\sigma_{1(ijm)}^{(k)} &= \overline{C}_{11(ijm)}^{(k)} \varepsilon_{1(ijm)}^{(k)} + \overline{C}_{12(ijm)}^{(k)} \varepsilon_{2(ijm)}^{(k)} + \overline{C}_{13(ijm)}^{(k)} \varepsilon_{3(ijm)}^{(k)} - \overline{p}_{31(ijm)}^{(k)} \mathscr{E}_{3(ijm)}^{(k)} \\
&\quad - \overline{z}_{11(ijm)}^{(k)} \widehat{\Delta\mathrm{T}}_{(ijm)}^{(k)} \sigma_{2(ijm)}^{(k)} \\
&= \overline{C}_{12(ijm)}^{(k)} \varepsilon_{1(ijm)}^{(k)} + \overline{C}_{22(ijm)}^{(k)} \varepsilon_{2(ijm)}^{(k)} + \overline{C}_{23(ijm)}^{(k)} \varepsilon_{3(ijm)}^{(k)} - \overline{p}_{32(ijm)}^{(k)} \mathscr{E}_{3(ijm)}^{(k)} \\
&\quad - \overline{z}_{22(ijm)}^{(k)} \widehat{\Delta\mathrm{T}}_{(ijm)}^{(k)} \tau_{12(ijm)}^{(k)} \\
&= \overline{C}_{66(ijm)}^{(k)} \gamma_{12(ijm)}^{(k)} \mathscr{D}_{1(ijm)}^{(k)} = \overline{p}_{14(ijm)}^{(k)} \gamma_{13(ijm)}^{(k)} + \overline{l}_{11(ijm)}^{(k)} \mathscr{E}_{1(ijm)}^{(k)} \mathscr{D}_{2(ijm)}^{(k)} \\
&= \overline{p}_{25(ijm)}^{(k)} \gamma_{23(ijm)}^{(k)} + \overline{l}_{22(ijm)}^{(k)} \mathscr{E}_{2(ijm)}^{(k)} h_{1(ijm)}^{(k)} = \overline{k}_{11(ijm)}^{(k)} \theta_{1(ijm)}^{(k)} h_{2(ijm)}^{(k)} \\
&= \overline{k}_{22(ijm)}^{(k)} \theta_{2(ijm)}^{(k)}
\end{aligned} \tag{73}$$

The out-of-plane shear stresses $\tau_{13}^{(k)}$ and $\tau_{23}^{(k)}$ are obtained from the three-dimensional equilibrium equations expressed in curvilinear principal coordinates, where $\sigma_1^{(k)}, \sigma_2^{(k)}$ and $\tau_{12}^{(k)}$ are derived from Eqn. (73) [38]:

$$\begin{aligned}
&\frac{\partial \tau_{13}^{(k)}}{\partial \zeta} + \left(\frac{2}{R_1+\zeta} + \frac{1}{R_2+\zeta}\right)\tau_{13}^{(k)} = -\frac{1}{A_1(1+\zeta/R_1)}\frac{\partial \sigma_1^{(k)}}{\partial \alpha_1} + \\
&+\frac{\sigma_2^{(k)} - \sigma_1^{(k)}}{A_1A_2(1+\zeta/R_2)}\frac{\partial A_2}{\partial \alpha_1} - \frac{1}{A_2(1+\zeta/R_2)}\frac{\partial \tau_{12}^{(k)}}{\partial \alpha_2} - \frac{2\tau_{12}^{(k)}}{A_1A_2(1+\zeta/R_1)}\frac{\partial A_1}{\partial \alpha_2} \\
&\frac{\partial \tau_{23}^{(k)}}{\partial \zeta} + \left(\frac{1}{R_1+\zeta} + \frac{2}{R_2+\zeta}\right)\tau_{23}^{(k)} = -\frac{1}{A_2(1+\zeta/R_2)}\frac{\partial \sigma_2^{(k)}}{\partial \alpha_2} + \\
&+\frac{\sigma_1^{(k)} - \sigma_2^{(k)}}{A_1A_2(1+\zeta/R_1)}\frac{\partial A_1}{\partial \alpha_2} - \frac{1}{A_1(1+\zeta/R_1)}\frac{\partial \tau_{12}^{(k)}}{\partial \alpha_1} - \frac{2\tau_{12}^{(k)}}{A_1A_2(1+\zeta/R_2)}\frac{\partial A_2}{\partial \alpha_1}
\end{aligned} \tag{74}$$

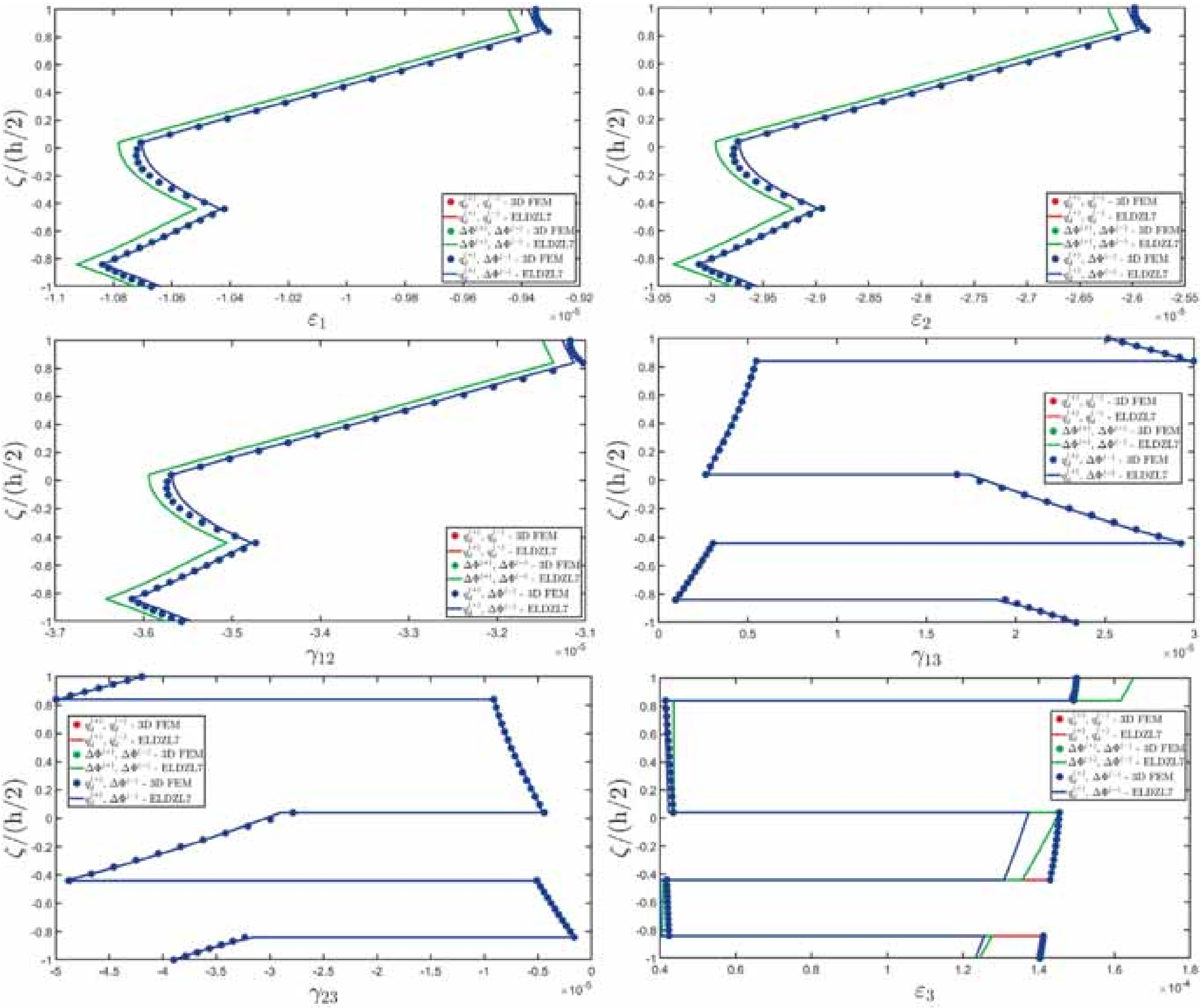

Fig. 7. Electro-mechanical analysis of a laminated rectangular plate subjected to various sinusoidal thermal loading conditions with $\widetilde{N} = \widetilde{M} = 1$. Representation of the distributions along the thickness direction of the components of the three-dimensional strain vector $\boldsymbol{\varepsilon}(\alpha_1, \alpha_2, \zeta)$, expressed in [m/m]. Thickness plots are provided for the point located at $(0.25L_1, 0.75L_2)$ within the two-dimensional physical domain.

The partial derivatives with respect to α_1, α_2 of both three-dimensional stress components and Lamé parameters are computed numerically using the GDQ method. The solution of the first-order differential equations (74) is derived for any $k = 1, ..., l$ using the boundary conditions provided below:

$$k = 1 \ \Rightarrow \ \begin{cases} \overline{\tau}_{13(ij1)}^{(1)} = q_{1(ij)}^{(-)} \\ \overline{\tau}_{23(ij1)}^{(1)} = q_{2(ij)}^{(-)} \end{cases}, \quad k \neq 1 \ \Rightarrow \ \begin{cases} \overline{\tau}_{13(ij((k-1)I_T+1))}^{(k)} = \overline{\tau}_{13(ij((k-1)I_T))}^{(k-1)} \\ \overline{\tau}_{23(ij((k-1)I_T+1))}^{(k)} = \overline{\tau}_{23(ij((k-1)I_T))}^{(k-1)} \end{cases} \tag{75}$$

As can be observed, when $k = 1$ is considered, the previous relation represents the equilibrium condition under external in-plane loads applied at the bottom surface, while interlaminar stress compatibility is addressed for $k = 2, ..., l$. The solution to Eqn. (74) using Eqn. (75) is denoted by $\overline{\tau}_{13}^{(k)}$ and $\overline{\tau}_{23}^{(k)}$. The loading compatibility conditions at the top surface are then enforced through the following relations [79]:

$$\begin{aligned} \tau_{13(ijm)}^{(k)} &= \overline{\tau}_{13(ijm)}^{(k)} + \frac{q_{1(ij)}^{(+)} - \overline{\tau}_{13(ij(lI_T))}^{(l)}}{h} \left(\zeta_m + \frac{h}{2} \right) \\ \tau_{23(ijm)}^{(k)} &= \overline{\tau}_{23(ijm)}^{(k)} + \frac{q_{2(ij)}^{(+)} - \overline{\tau}_{23(ij(lI_T))}^{(l)}}{h} \left(\zeta_m + \frac{h}{2} \right) \end{aligned} \tag{76}$$

for any $i = 1, ..., I_N$ and $j = 1, ..., I_M$ and $m = 1, ..., lI_T$. In the same way, the actual distribution of out-of-plane normal stress $\sigma_3^{(k)}$, electric flux $\mathscr{D}_3^{(k)}$, and thermal flux $h_3^{(k)}$ is derived from the three-dimensional balance equations along the thickness direction:

$$\begin{aligned} &\frac{\partial \sigma_3^{(k)}}{\partial \zeta} + \sigma_3^{(k)} \left(\frac{1}{R_1 + \zeta} + \frac{1}{R_2 + \zeta} \right) = -\frac{1}{A_1(1+\zeta/R_1)} \frac{\partial \tau_{13}^{(k)}}{\partial \alpha_1} - \frac{\tau_{13}^{(k)}}{A_1 A_2 (1+\zeta/R_2)} \frac{\partial A_2}{\partial \alpha_1} + \\ &\quad - \frac{1}{A_2(1+\zeta/R_2)} \frac{\partial \tau_{23}^{(k)}}{\partial \alpha_2} - \frac{\tau_{23}^{(k)}}{A_1 A_2 (1+\zeta/R_1)} \frac{\partial A_1}{\partial \alpha_2} + \frac{\sigma_1^{(k)}}{R_1 + \zeta} + \frac{\sigma_2^{(k)}}{R_2 + \zeta} \end{aligned}$$

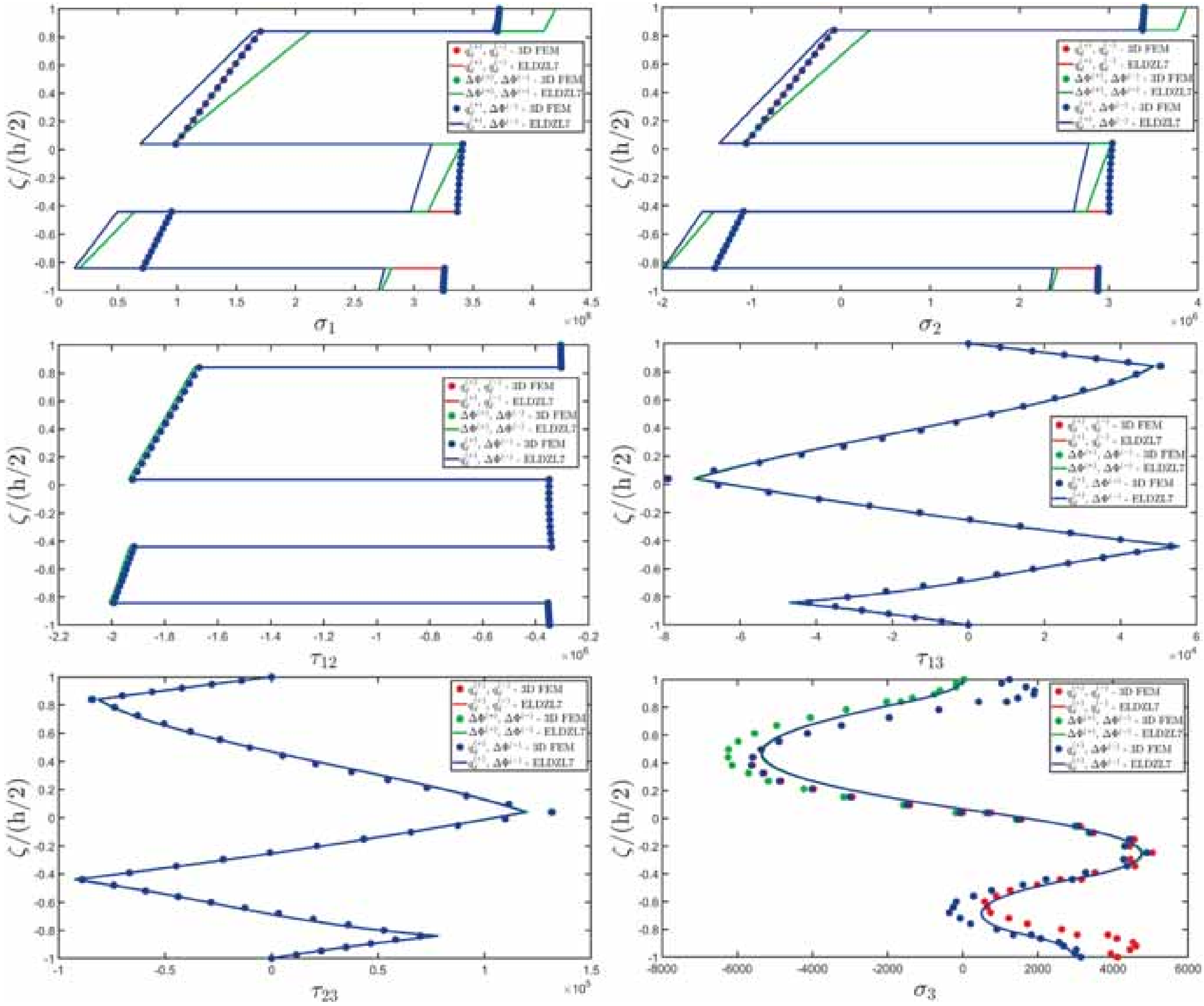

Fig. 8. Electro-mechanical analysis of a laminated rectangular plate subjected to various sinusoidal thermal loading conditions with $\widetilde{N} = \widetilde{M} = 1$. Representation of the distributions along the thickness direction of the components of the three-dimensional stress vector $\boldsymbol{\sigma}(\alpha_1, \alpha_2, \zeta)$, expressed in $[\mathrm{N/m^2}]$. Thickness plots are provided for the point located at $(0.25L_1, 0.75L_2)$ within the two-dimensional physical domain.

$$\begin{aligned}
&\frac{\partial \mathscr{D}_3^{(k)}}{\partial \zeta} + \mathscr{D}_3^{(k)}\left(\frac{1}{R_1+\zeta}+\frac{1}{R_2+\zeta}\right) = -\frac{1}{A_1(1+\zeta/R_1)}\frac{\partial \mathscr{D}_1^{(k)}}{\partial \alpha_1} \\
&\quad - \frac{\mathscr{D}_1^{(k)}}{A_1A_2(1+\zeta/R_2)}\frac{\partial A_2}{\partial \alpha_1} + \quad -\frac{1}{A_2(1+\zeta/R_2)}\frac{\partial \mathscr{D}_2^{(k)}}{\partial \alpha_2} \\
&\quad - \frac{\mathscr{D}_2^{(k)}}{A_1A_2(1+\zeta/R_1)}\frac{\partial A_1}{\partial \alpha_2} \\
&\frac{\partial h_3^{(k)}}{\partial \zeta} + h_3^{(k)}\left(\frac{1}{R_1+\zeta}+\frac{1}{R_2+\zeta}\right) = -\frac{1}{A_1(1+\zeta/R_1)}\frac{\partial h_1^{(k)}}{\partial \alpha_1} \\
&\quad - \frac{h_1^{(k)}}{A_1A_2(1+\zeta/R_2)}\frac{\partial A_2}{\partial \alpha_1} + \quad -\frac{1}{A_2(1+\zeta/R_2)}\frac{\partial h_2^{(k)}}{\partial \alpha_2} \\
&\quad - \frac{h_2^{(k)}}{A_1A_2(1+\zeta/R_1)}\frac{\partial A_1}{\partial \alpha_2}
\end{aligned} \tag{77}$$

It should be noted that in the previous equation, the quantities $\mathscr{D}_1^{(k)}$, $\mathscr{D}_2^{(k)}$ and $h_1^{(k)}, h_2^{(k)}$ are derived from the constitutive relation (73), while $\tau_{13}^{(k)}, \tau_{23}^{(k)}$ come from Eqn. (76). A particular solution to Eqn. (77), denoted by $\overline{\sigma}_3^{(k)}, \overline{\mathscr{D}}_3^{(k)}$ and $\overline{h}_3^{(k)}$, is obtained by applying the following boundary conditions, which represent the external loads at the bottom surface ($k = 1$) and the secondary variables balance at each interface between adjacent layers ($k \neq 1$) [35]:

$$\begin{aligned}
k = 1 \;\Rightarrow\; &\begin{cases} \overline{\sigma}_{3(ij1)}^{(1)} = q_{3(ij)}^{(-)} \\ \overline{\mathscr{D}}_{3(ij1)}^{(1)} = q_{\mathrm{D}(ij)}^{(-)} \\ h_{3(ij1)}^{(1)} = q_{h(ij)}^{(-)} \end{cases} \qquad k \\
\neq 1 \;\Rightarrow\; &\begin{cases} \overline{\sigma}_{3(ij((k-1)I_T+1))}^{(k)} = \overline{\sigma}_{3(ij((k-1)I_T))}^{(k-1)} \\ \overline{\mathscr{D}}_{3(ij((k-1)I_T+1))}^{(k)} = \overline{\mathscr{D}}_{3(ij((k-1)I_T))}^{(k-1)} \\ h_{3(ij((k-1)I_T+1))}^{(k)} = h_{3(ij((k-1)I_T))}^{(k-1)} \end{cases}
\end{aligned} \tag{78}$$

The final profiles of secondary variables $\sigma_3^{(k)}, \mathscr{D}_3^{(k)}$ and $h_3^{(k)}$ are obtained by applying the multifield loading conditions at the top surface:

$$\sigma_{3(ijm)}^{(k)} = \overline{\sigma}_{3(ijm)}^{(k)} + \frac{q_{3(ij)}^{(+)} - \overline{\sigma}_{3(ij(lI_T))}^{(l)}}{h}\left(\zeta_m + \frac{h}{2}\right)$$

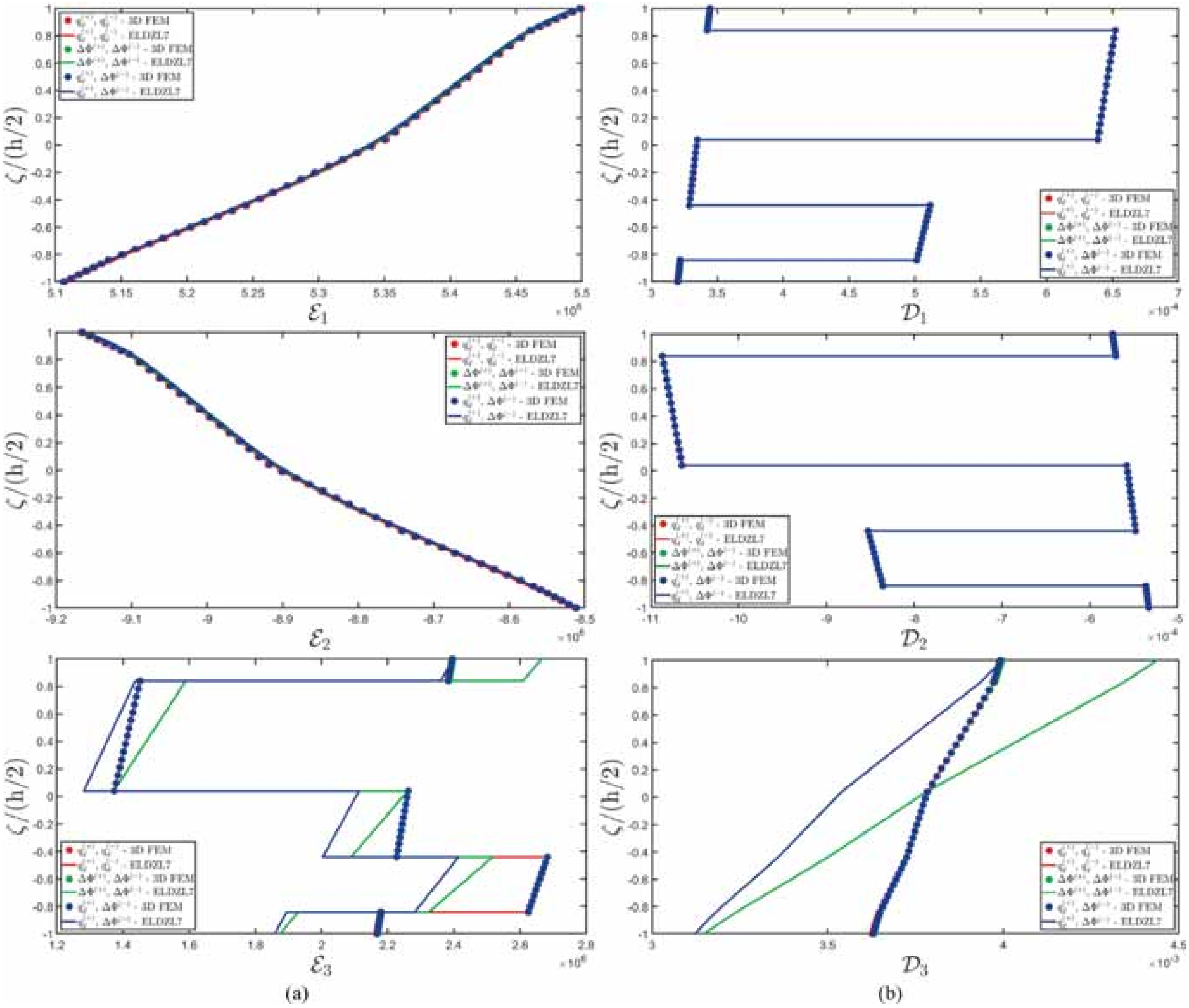

Fig. 9. Electro-mechanical analysis of a laminated rectangular plate subjected to various sinusoidal thermal loading conditions with $\widetilde{N} = \widetilde{M} = 1$. Representation of the distributions along the thickness direction of the components of the three-dimensional electrostatic field vector $\mathscr{E}(\alpha_1, \alpha_2, \zeta)$ (a), expressed in $[\mathrm{V/m}]$ and of the electric flux vector $\mathscr{D}(\alpha_1, \alpha_2, \zeta)$ (b), expressed in $[\mathrm{C/m^2}]$. Thickness plots are provided for the point located at $(0.25L_1, 0.75L_2)$ within the two-dimensional physical domain.

$$\mathscr{D}^{(k)}_{3(ijm)} = \overline{\mathscr{D}}^{(k)}_{3(ijm)} + \frac{q^{(+)}_{\mathrm{D}(ij)} - \overline{\mathscr{D}}^{(l)}_{3(ij(l\,I_T))}}{h}\left(\zeta_m + \frac{h}{2}\right)$$

$$\overline{h}^{(k)}_{3(ijm)} = \overline{h}^{(k)}_{3(ijm)} + \frac{q^{(+)}_{h(ij)} - \overline{h}^{(l)}_{3(ij(l\,I_T))}}{h}\left(\zeta_m + \frac{h}{2}\right) \tag{79}$$

The recovered profile of out-of-plane primary variables $\boldsymbol{x}^{(k)}_{(ijm)} = \left[\gamma^{(k)}_{13(ijm)} \quad \gamma^{(k)}_{23(ijm)} \quad \varepsilon^{(k)}_{3(ijm)} \quad \mathscr{E}^{(k)}_{3(ijm)} \quad h^{(k)}_{3(ijm)}\right]^T$ is derived from the inverse of the three-dimensional constitutive relation given in Eqn. (24), thus resulting in an algebraic linear system [35]:

$$\boldsymbol{A}^{(k)}_{(ijm)}\boldsymbol{x}^{(k)}_{(ijm)} = \boldsymbol{B}^{(k)}_{(ijm)} \tag{80}$$

where matrix $\boldsymbol{A}^{(k)}_{(ijm)}$ contains the three-dimensional constitutive coefficients, while vector $\boldsymbol{B}^{(k)}_{(ijm)}$ depends on three-dimensional primary variables. Further details can be found in Ref. [35].

5. Applications and results

In this section, the present higher-order theory is applied in some numerical examples involving various laminated panels with fully coupled thermo-electro-mechanical properties, and subjected to different external loads, including thermal loads, charge distributions, and mechanical surface pressures. The multifield response is reported in terms of through-the-thickness distribution of configuration, primary, and secondary variables at a fixed point of the two-dimensional physical

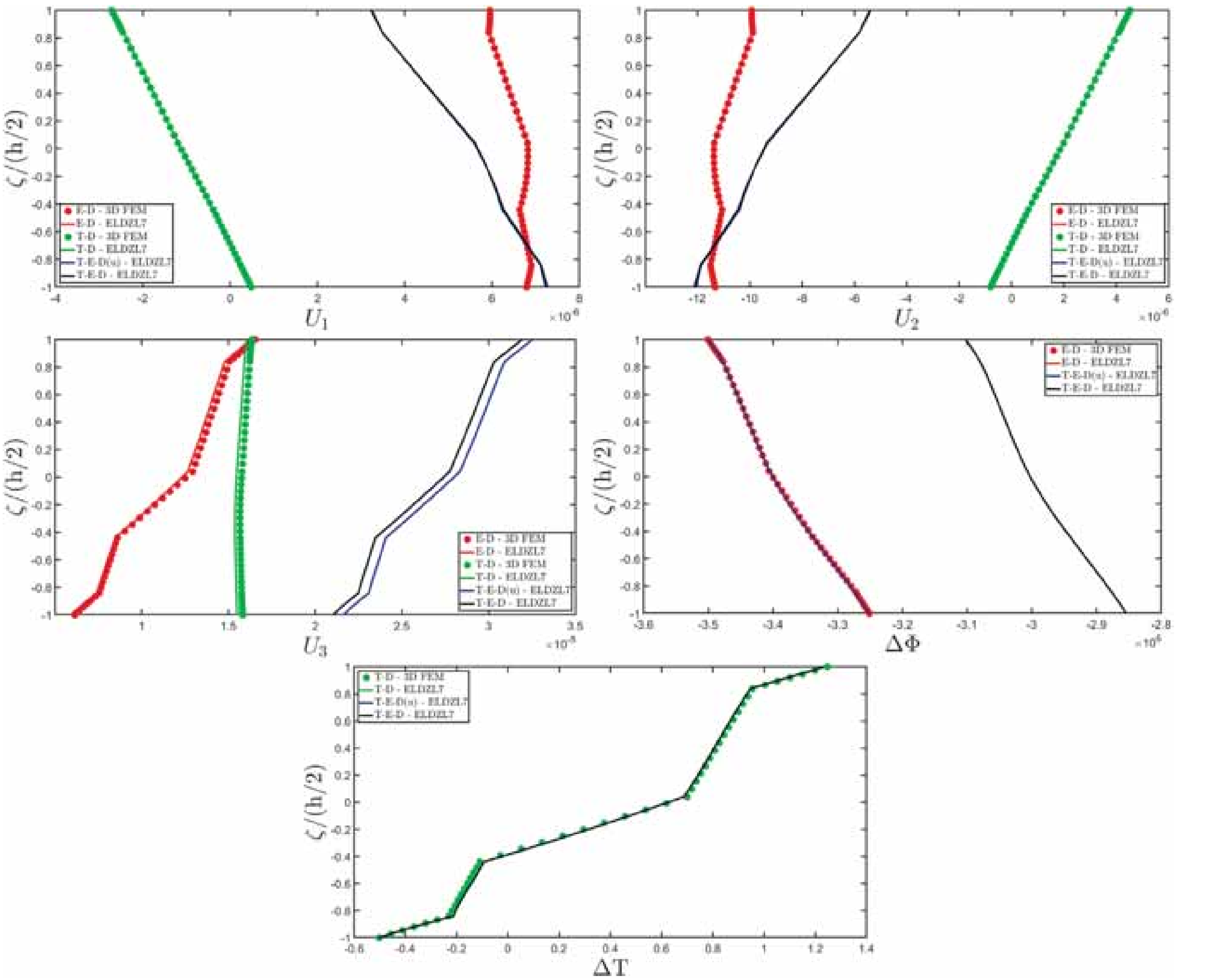

Fig. 10. Thermo-electro-mechanical analysis of a laminated rectangular plate subjected to various sinusoidal thermal and electric loading conditions with $\widetilde{N} = \widetilde{M} = 1$. Representation of the distributions along the thickness direction of the configuration variables of the problem, namely the displacement field components U_1, U_2, U_3 expressed in [m], the electric potential variation $\Delta\phi$ and the temperature variation ΔT with respect to the zero-stress reference configuration, expressed in [V] and [K], respectively. Thickness plots are provided for the point located at $(0.25L_1, 0.75L_2)$ within the two-dimensional physical domain.

domain. For each case, some simulations are performed for validation purposes, comparing the model results to three-dimensional predictions from classical finite elements. Novel coupling effects are investigated, demonstrating the advantages of the present semi-analytical formulation over the existing multifield tools in terms of accuracy and computational efficiency.

Each layer of the stacking sequence consists of a multiphase electro-thermo-elastic composite made of a cobalt ferrite matrix (m) with aligned cylindrical fibers of barium titanate (f), oriented along the thickness direction.

The homogenized material properties of an arbitrary layer are obtained for a given volume fraction of each constituent V_f, V_m, by using the analytical expressions provided in Appendix I, based on the application of the Mori-Tanaka's approach. The cobalt ferrite ($CoFe_2O_4$) matrix is characterized by a density $\rho^{(k)} = 5300\,\mathrm{kg/m^3}$ and specific heat $c_p^{(k)} = 377.36\,\mathrm{J/kgK}$. In addition, the thermo-electro-mechanical properties are listed below:

$$\boldsymbol{\Gamma}_{\mathrm{C}}^{(k)} = \begin{bmatrix} C_{11}^{(k)} & C_{12}^{(k)} & C_{16}^{(k)} & C_{14}^{(k)} & C_{15}^{(k)} & C_{13}^{(k)} \\ C_{12}^{(k)} & C_{22}^{(k)} & C_{26}^{(k)} & C_{24}^{(k)} & C_{25}^{(k)} & C_{23}^{(k)} \\ C_{16}^{(k)} & C_{26}^{(k)} & C_{66}^{(k)} & C_{46}^{(k)} & C_{56}^{(k)} & C_{36}^{(k)} \\ C_{14}^{(k)} & C_{24}^{(k)} & C_{46}^{(k)} & C_{44}^{(k)} & C_{45}^{(k)} & C_{34}^{(k)} \\ C_{15}^{(k)} & C_{25}^{(k)} & C_{56}^{(k)} & C_{45}^{(k)} & C_{55}^{(k)} & C_{35}^{(k)} \\ C_{13}^{(k)} & C_{23}^{(k)} & C_{36}^{(k)} & C_{34}^{(k)} & C_{35}^{(k)} & C_{33}^{(k)} \end{bmatrix} = \begin{bmatrix} 286 & 173 & 0 & 0 & 0 & 170.5 \\ 173 & 286 & 0 & 0 & 0 & 170.5 \\ 0 & 0 & 56.5 & 0 & 0 & 0 \\ 0 & 0 & 0 & 45.3 & 0 & 0 \\ 0 & 0 & 0 & 0 & 45.3 & 0 \\ 170.5 & 170.5 & 0 & 0 & 0 & 269.5 \end{bmatrix} \times 10^9 \frac{\mathrm{N}}{\mathrm{m}^2}$$

$$\boldsymbol{\Gamma}_{\mathrm{L}}^{(k)} = \begin{bmatrix} l_{11}^{(k)} & l_{12}^{(k)} & l_{13}^{(k)} \\ l_{21}^{(k)} & l_{22}^{(k)} & l_{23}^{(k)} \\ l_{31}^{(k)} & l_{32}^{(k)} & l_{33}^{(k)} \end{bmatrix} = \begin{bmatrix} 8 & 0 & 0 \\ 0 & 8 & 0 \\ 0 & 0 & 9.3 \end{bmatrix} \times 10^{-11} \frac{\mathrm{C}^2}{\mathrm{N\,m}^2}$$

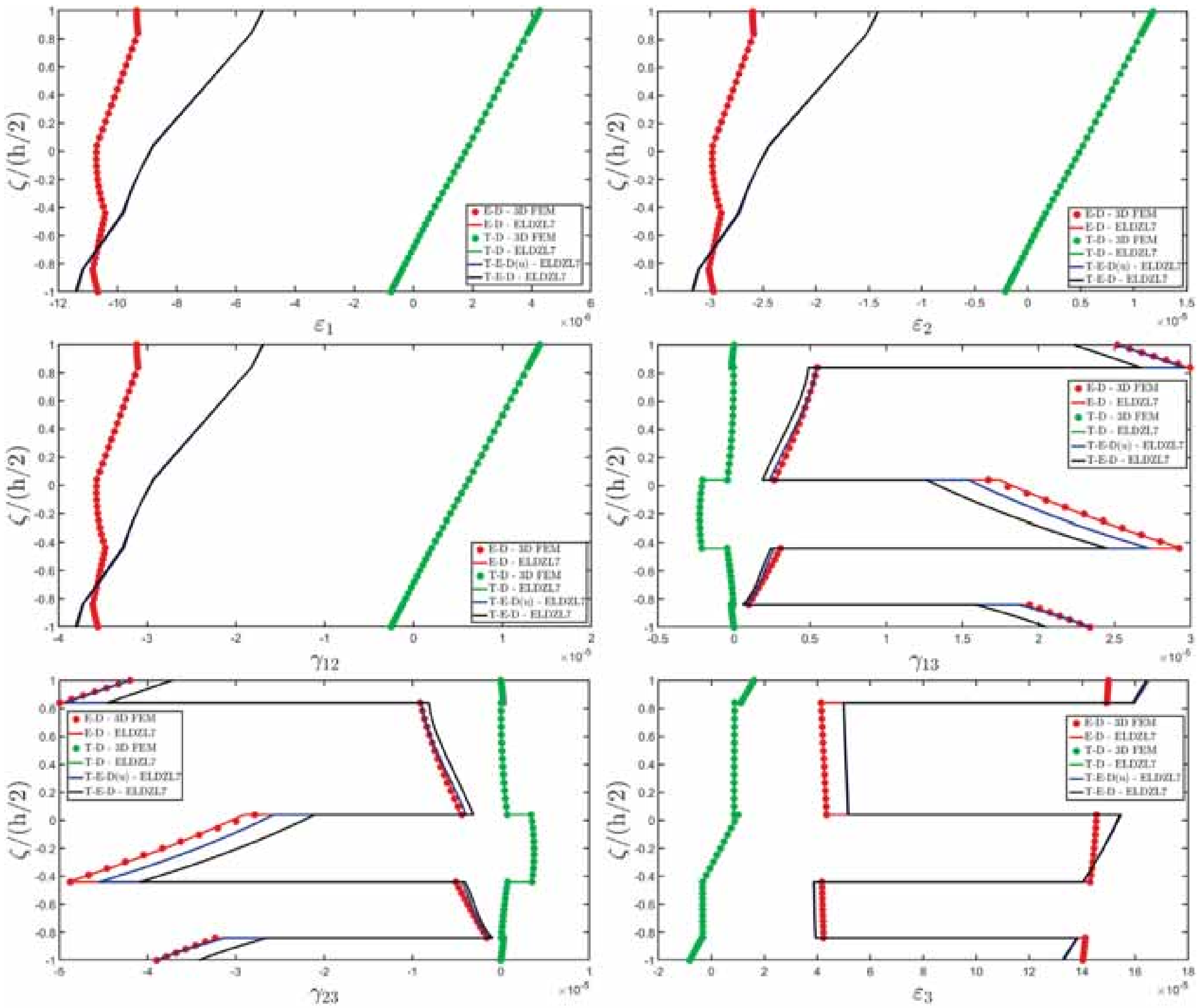

Fig. 11. Thermo-electro-mechanical analysis of a laminated rectangular plate subjected to various sinusoidal thermal and electric loading conditions with $\widetilde{N} = \widetilde{M} = 1$. Representation of the distributions along the thickness direction of the components of the three-dimensional strain vector $\boldsymbol{\varepsilon}(\alpha_1, \alpha_2, \zeta)$, expressed in [m/m]. Thickness plots are provided for the point located at $(0.25L_1, 0.75L_2)$ within the two-dimensional physical domain.

$$\boldsymbol{\Gamma}_{\mathrm{P}}^{(k)} = \begin{bmatrix} p_{11}^{(k)} & p_{12}^{(k)} & p_{16}^{(k)} & p_{14}^{(k)} & p_{15}^{(k)} & p_{13}^{(k)} \\ p_{21}^{(k)} & p_{22}^{(k)} & p_{26}^{(k)} & p_{24}^{(k)} & p_{25}^{(k)} & p_{23}^{(k)} \\ p_{31}^{(k)} & p_{32}^{(k)} & p_{36}^{(k)} & p_{34}^{(k)} & p_{35}^{(k)} & p_{33}^{(k)} \end{bmatrix} = \begin{bmatrix} 0 & 0 & 0 & 0 & 0 & 0 \\ 0 & 0 & 0 & 0 & 0 & 0 \\ 0 & 0 & 0 & 0 & 0 & 0 \end{bmatrix} \frac{\mathrm{C}}{\mathrm{m}^2}$$

$$\overline{\boldsymbol{\Gamma}}_{\mathrm{a}}^{(k)} = \begin{bmatrix} a_{11}^{(k)} & a_{22}^{(k)} & a_{12}^{(k)} & a_{13}^{(k)} & a_{23}^{(k)} & a_{33}^{(k)} \end{bmatrix}^T = \begin{bmatrix} 10 & 10 & 0 & 0 & 0 & 5 \end{bmatrix}^T \times 10^{-6} \frac{1}{\mathrm{K}}$$

$$\boldsymbol{\Gamma}_{\mathrm{K}}^{(k)} = \begin{bmatrix} k_{11}^{(k)} & k_{12}^{(k)} & k_{13}^{(k)} \\ k_{21}^{(k)} & k_{22}^{(k)} & k_{23}^{(k)} \\ k_{31}^{(k)} & k_{32}^{(k)} & k_{33}^{(k)} \end{bmatrix} = \begin{bmatrix} 3.2 & 0 & 0 \\ 0 & 3.2 & 0 \\ 0 & 0 & 3.2 \end{bmatrix} \frac{\mathrm{J}}{\mathrm{m\,K}}$$

$$\boldsymbol{\Gamma}_{\mathrm{o}}^{(k)} = \begin{bmatrix} o_{11}^{(k)} & o_{22}^{(k)} & o_{33}^{(k)} \end{bmatrix} = \begin{bmatrix} 0 & 0 & 0 \end{bmatrix} \frac{\mathrm{C}}{\mathrm{m}^2\mathrm{K}} \tag{81}$$

On the other hand, the constitutive relation (26) for **barium titanate** ($BaTiO_3$) with density $\rho^{(k)} = 5800\,\mathrm{kg/m^3}$ and specific heat $c_p^{(k)} = 550.62\,\mathrm{J/kgK}$, is written by assuming the following expression for the constitutive matrices:

$$\boldsymbol{\Gamma}_{\mathrm{C}}^{(k)} = \begin{bmatrix} C_{11}^{(k)} & C_{12}^{(k)} & C_{16}^{(k)} & C_{14}^{(k)} & C_{15}^{(k)} & C_{13}^{(k)} \\ C_{12}^{(k)} & C_{22}^{(k)} & C_{26}^{(k)} & C_{24}^{(k)} & C_{25}^{(k)} & C_{23}^{(k)} \\ C_{16}^{(k)} & C_{26}^{(k)} & C_{66}^{(k)} & C_{46}^{(k)} & C_{56}^{(k)} & C_{36}^{(k)} \\ C_{14}^{(k)} & C_{24}^{(k)} & C_{46}^{(k)} & C_{44}^{(k)} & C_{45}^{(k)} & C_{34}^{(k)} \\ C_{15}^{(k)} & C_{25}^{(k)} & C_{56}^{(k)} & C_{45}^{(k)} & C_{55}^{(k)} & C_{35}^{(k)} \\ C_{13}^{(k)} & C_{23}^{(k)} & C_{36}^{(k)} & C_{34}^{(k)} & C_{35}^{(k)} & C_{33}^{(k)} \end{bmatrix}$$

$$= \begin{bmatrix} 166 & 77 & 0 & 0 & 0 & 78 \\ 77 & 166 & 0 & 0 & 0 & 78 \\ 0 & 0 & 44.5 & 0 & 0 & 0 \\ 0 & 0 & 0 & 43 & 0 & 0 \\ 0 & 0 & 0 & 0 & 43 & 0 \\ 78 & 78 & 0 & 0 & 0 & 162 \end{bmatrix} \times 10^9 \frac{\mathrm{N}}{\mathrm{m}^2}$$

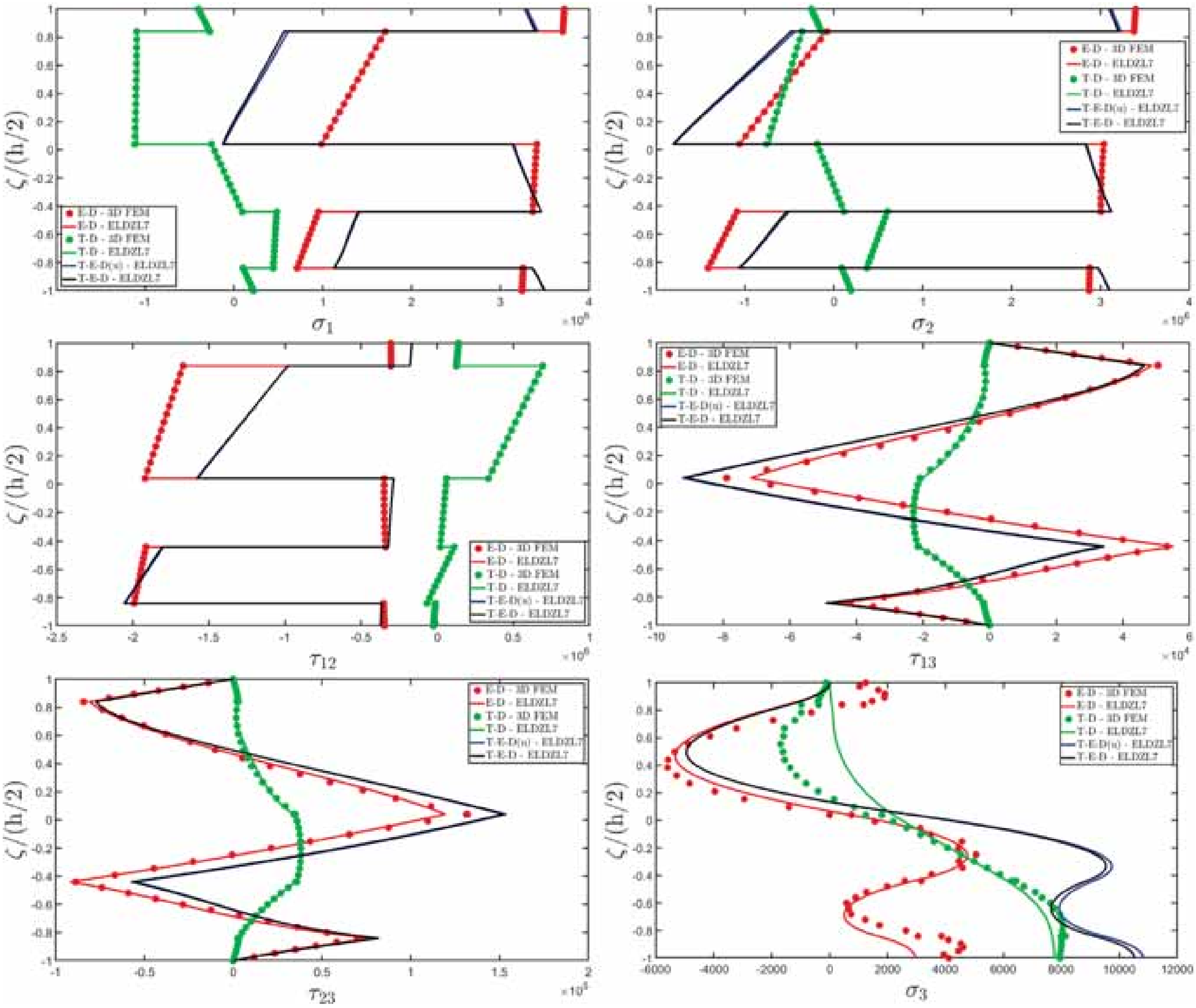

Fig. 12. Thermo-electro-mechanical analysis of a laminated rectangular plate subjected to various sinusoidal thermal and electric loading conditions with $\widetilde{N} = \widetilde{M} = 1$. Representation of the distributions along the thickness direction of the components of the three-dimensional stress vector $\boldsymbol{\sigma}(\alpha_1, \alpha_2, \zeta)$, expressed in $\left[\mathrm{N/m^2}\right]$. Thickness plots are provided for the point located at $(0.25L_1, 0.75L_2)$ within the two-dimensional physical domain.

$$\boldsymbol{\Gamma}_{\mathrm{L}}^{(k)} = \begin{bmatrix} l_{11}^{(k)} & l_{12}^{(k)} & l_{13}^{(k)} \\ l_{21}^{(k)} & l_{22}^{(k)} & l_{23}^{(k)} \\ l_{31}^{(k)} & l_{32}^{(k)} & l_{33}^{(k)} \end{bmatrix} = \begin{bmatrix} 1.12 & 0 & 0 \\ 0 & 1.12 & 0 \\ 0 & 0 & 1.26 \end{bmatrix} \cdot 10^{-8} \ \frac{\mathrm{C}^2}{\mathrm{N\,m^2}}$$

$$\boldsymbol{\Gamma}_{\mathrm{P}}^{(k)} = \begin{bmatrix} p_{11}^{(k)} & p_{12}^{(k)} & p_{16}^{(k)} & p_{14}^{(k)} & p_{15}^{(k)} & p_{13}^{(k)} \\ p_{21}^{(k)} & p_{22}^{(k)} & p_{26}^{(k)} & p_{24}^{(k)} & p_{25}^{(k)} & p_{23}^{(k)} \\ p_{31}^{(k)} & p_{32}^{(k)} & p_{36}^{(k)} & p_{34}^{(k)} & p_{35}^{(k)} & p_{33}^{(k)} \end{bmatrix} = \begin{bmatrix} 0 & 0 & 0 & 11.6 & 0 & 0 \\ 0 & 0 & 0 & 0 & 11.6 & 0 \\ -4.4 & -4.4 & 0 & 0 & 0 & 18.6 \end{bmatrix} \frac{\mathrm{C}}{\mathrm{m^2}}$$

$$\overline{\boldsymbol{\Gamma}}_{\mathrm{a}}^{(k)} = \begin{bmatrix} a_{11}^{(k)} & a_{22}^{(k)} & a_{12}^{(k)} & a_{13}^{(k)} & a_{23}^{(k)} & a_{33}^{(k)} \end{bmatrix}^T = \begin{bmatrix} 15.6 & 15.6 & 0 & 0 & 0 & 6.4 \end{bmatrix}^T \times 10^{-6} \frac{1}{\mathrm{K}}$$

$$\boldsymbol{\Gamma}_{\mathrm{K}}^{(k)} = \begin{bmatrix} k_{11}^{(k)} & k_{12}^{(k)} & k_{13}^{(k)} \\ k_{21}^{(k)} & k_{22}^{(k)} & k_{23}^{(k)} \\ k_{31}^{(k)} & k_{32}^{(k)} & k_{33}^{(k)} \end{bmatrix} = \begin{bmatrix} 2.5 & 0 & 0 \\ 0 & 2.5 & 0 \\ 0 & 0 & 2.5 \end{bmatrix} \frac{\mathrm{J}}{\mathrm{m\,K}}$$

$$\boldsymbol{\Gamma}_{\mathrm{o}}^{(k)} = \begin{bmatrix} o_{11}^{(k)} & o_{22}^{(k)} & o_{33}^{(k)} \end{bmatrix} = \begin{bmatrix} 0 & 0 & 2 \end{bmatrix} \times 10^{-4} \frac{\mathrm{C}}{\mathrm{m^2K}} \tag{82}$$

Three different laminates are here studied, namely, a rectangular plate, a cylindrical panel, and a spherical structure. For each case, the model is validated for various loading conditions, where different physical aspects are here examined in coupled form. For all examples, the lamination schemes are derived by combining three different materials, denoted by ETE-1, ETE-2 and ETE-3, for a volume fraction of cylindrical fibers equal to $V_f = 0.6$, $V_f = 0.2$, and $V_f = 0.1$, respectively. To identify the coupling orders between the involved physical phenomena, a specific nomenclature is introduced. More specifically, letter “D” refers to the mechanical elasticity, “T” is used for thermal conduction problems, and “E” refers to electricity. In this way, E-D simulations address

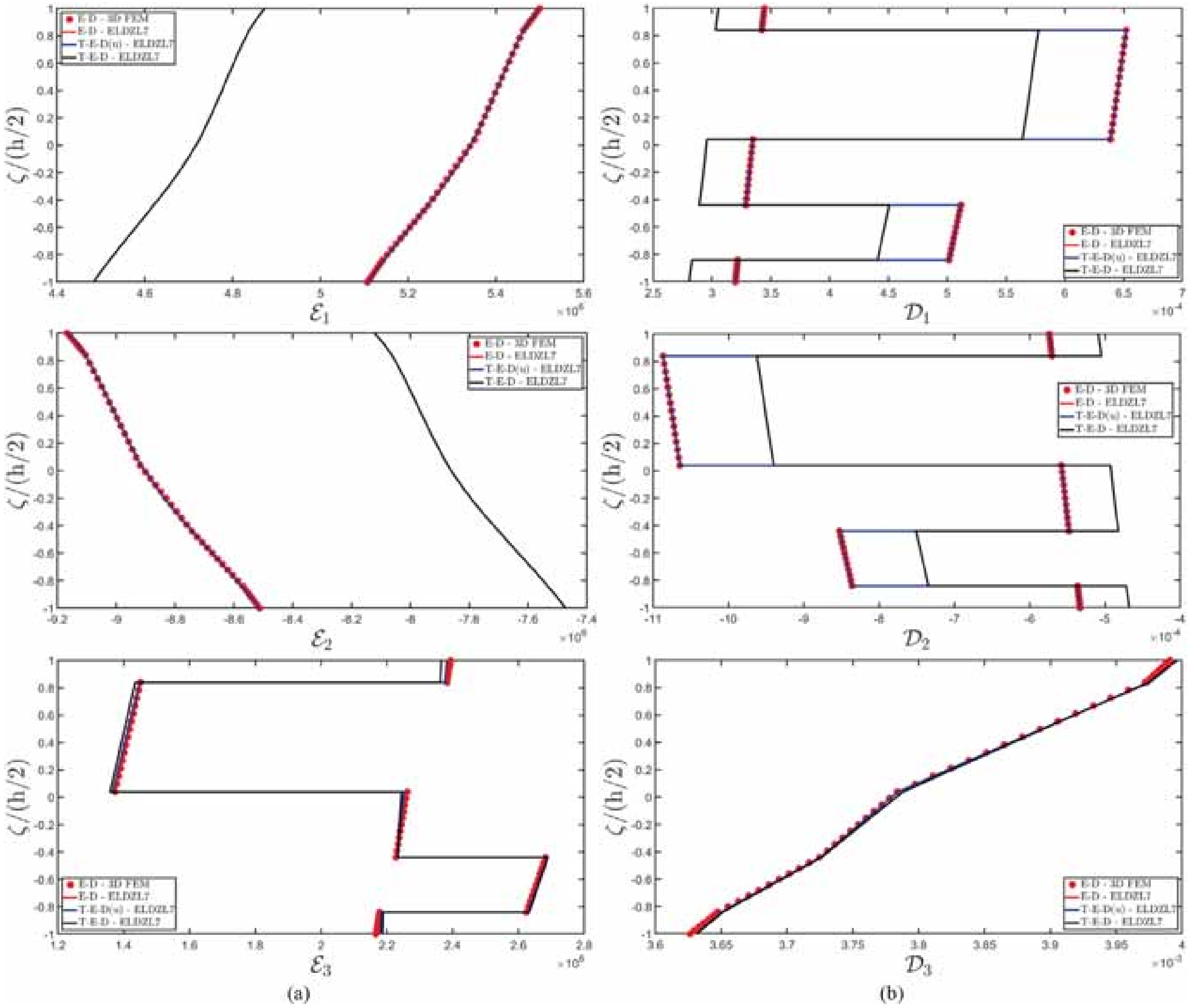

Fig. 13. Electro-thermo-mechanical analysis of a laminated rectangular plate subjected to various sinusoidal thermal loading conditions with $\widetilde{N} = \widetilde{M} = 1$. Representation of the distributions along the thickness direction of the components of the three-dimensional electrostatic field vector $\mathscr{E}(\alpha_1, \alpha_2, \zeta)$ (a), expressed in $[\mathrm{V/m}]$ and of the electric flux vector $\mathscr{D}(\alpha_1, \alpha_2, \zeta)$ (b), expressed in $[\mathrm{C/m^2}]$. Thickness plots are provided for the point located at $(0.25L_1, 0.75L_2)$ within the two-dimensional physical domain.

an electro-mechanical coupling, T-D simulations cover thermo-mechanical problems, and T-E-D considers a full coupling between thermal, electric, and mechanical physics.

In the first example, a laminated rectangular plate is studied under SSSS boundary conditions. The structure consists of five layers with thickness $h_2 = h_5 = 0.01\,\mathrm{m}$, $h_2 = 0.025\,\mathrm{m}$, $h_3 = 0.03\,\mathrm{m}$ and $h_4 = 0.05\,\mathrm{m}$, while the geometric dimensions are $L_1 = 2.00\,\mathrm{m}$ and $L_2 = 1.20\,\mathrm{m}$. Referring to Eqn. (1), the reference surface equation is written as follows:

$$\boldsymbol{r}(s_1, s_2) = s_1\boldsymbol{e}_1 - s_2\boldsymbol{e}_2 \tag{83}$$

setting $\alpha_1 = s_1 \in [0, L_1]$ and $\alpha_2 = s_2 \in [0, L_2]$. The adopted lamination scheme is (ETE - 1/ETE - 3/ETE - 1/ETE - 2/ETE - 1), while the material reference system for each lamina coincides with the geometry reference system, namely (0 / 0 / 0 / 0 / 0). The panel rests on an elastic Winkler-type foundation with stiffness $k_{3f}^{(-)} = 5 \times 10^8\,\mathrm{N/m^3}$, and it is subjected to sinusoidal distributions with $n = m = 1$ of thermal and electric loads at the top and bottom surfaces, defined by Eqn. (41) as follows:

$$\widetilde{q}_\alpha^{(\pm)}(s_1, s_2) = \sin\left(\frac{n\pi}{L_1}s_1\right)\sin\left(\frac{m\pi}{L_2}s_2\right) \tag{84}$$

with $\alpha = h$. The results of the simulations, evaluated at $(0.25L_1, 0.75L_2)$ within the physical domain, are reported in Figs. 2-5 for thermo-mechanical simulations. Figs. 6-9 present the results of electro-mechanical numerical investigations at the same point. Finally, the thermo-electro-mechanical coupling is examined in Figs. 10-14.

The first set of simulations evaluates the response of the plate to sinusoidal thermal fluxes applied at the top and bottom sides with magnitudes $\overline{q}_h^{(+)} = -32.5347\,\mathrm{J/m^2}$ and $\overline{q}_h^{(-)} = -30.2820\,\mathrm{J/m^2}$. The results, derived using the ELDZL7 higher-order kinematic model, are validated against three-dimensional finite element predictions for 664689 DOFs, while using C3D20T brick elements. As shown in Fig. 2, the structure exhibits some linear distributions for the in-plane displacement components, while a more complex profile is observed for deflection U_3. The deflection of the structure, indeed, must be studied using higher-order theories rather than classical approaches like the FSDT. Furthermore, the through-the-thickness temperature distribution shows an abrupt

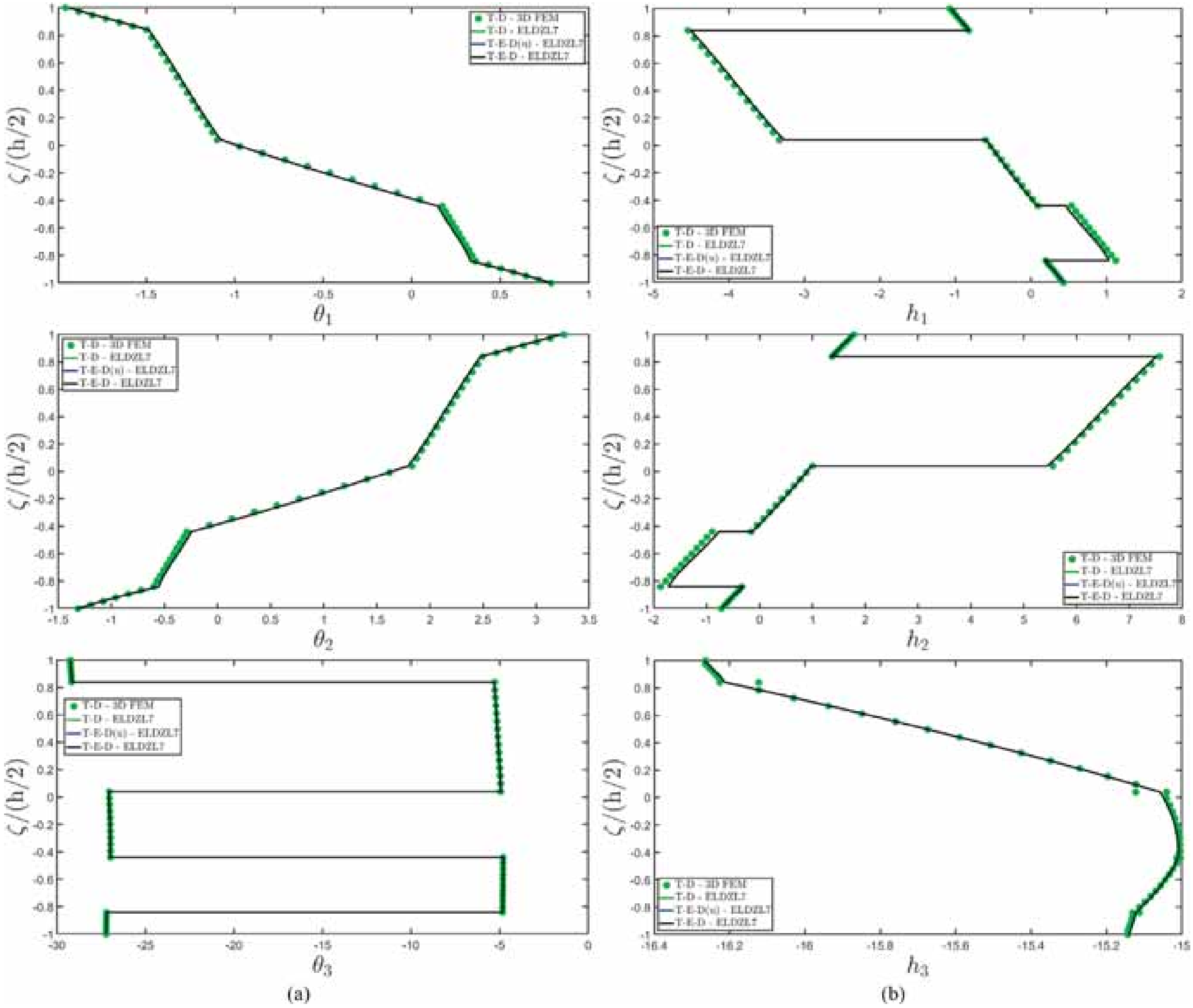

Fig. 14. Thermo-electro-mechanical analysis of a laminated rectangular plate subjected to various sinusoidal thermal loading conditions with $\widetilde{N} = \widetilde{M} = 1$. Representation of the distributions along the thickness direction of the components of the three-dimensional temperature gradient vector $\boldsymbol{\theta}(\alpha_1, \alpha_2, \zeta)$ (a), expressed in $[\mathrm{K/m}]$ and of the thermal flux vector $\boldsymbol{h}(\alpha_1, \alpha_2, \zeta)$ (b), expressed in $[\mathrm{J/m^2}]$. Thickness plots are provided for the point located at $(0.25L_1, 0.75L_2)$ within the two-dimensional physical domain.

variation in inclination due to different thermal properties of adjacent laminae. As a consequence, zigzag theories are essential to obtain accurate results. As far as the three-dimensional strain components is concerned, complex deformation distributions are found for the out-of-plane strains, especially distortions, as shown in Fig. 3. The strain distribution ε_3, indicates that stretching of the laminate varies among different laminae, with a uniform behavior for laminates with higher out-of-plane stiffness values. Fig. 4 presents the through-the-thickness distribution of each three-dimensional stress component. Note that these mechanical secondary variables are not induced by external pressures but are consequences of a thermal expansion within the solid. Fig. 5 shows the results for thermal primary and secondary variables. The present coupled multifield model matches successfully the reference numerical solution for both in-plane and out-of-plane components, employing a reduced computational effort due to the two-dimensional analytical solution and the GDQ-based recovery procedure.

Once the model is validated, a similar simulation is repeated by applying a sinusoidal distribution (84) of temperature variation at the top and bottom surfaces, with magnitudes $\overline{\Delta \mathrm{T}}^{(+)} = 2.5\,\mathrm{K}$ and $\overline{\Delta \mathrm{T}}^{(-)} = -1\,\mathrm{K}$, according to the following relation:

$$\Delta \mathrm{T}^{(\pm)}(s_1, s_2) = \overline{\Delta \mathrm{T}}^{(\pm)} \widetilde{q}_h^{(\pm)}(s_1, s_2) \tag{85}$$

Even in this case, the numerical predictions match well FEM-based results, as shown in Figs. 2-5. However, Fig. 5 indicates that the out-of-plane thermal flux component derived with the analytical theory is inaccurate. This discrepancy arises because the recovery procedure, here used to solve the balance equations, relies on the value obtained from the constitutive relation (24) when no arbitrary external flux values are available. Similar results are observed in the third simulation, where a sinusoidal flux of magnitude $\overline{q}_h^{(+)} = -32.5347\,\mathrm{J/m^2}$ is applied to the top surface and a prescribed value ($\overline{\Delta \mathrm{T}}^{(-)} = -1\,\mathrm{K}$) is assumed at the bottom side. The higher-order analytical model predicts accurately the thermal flux distribution in the out-of-plane direction near the top surface, but deviates from FEM-based results at the bottom surface. For this reason, the ELW approach proves to be a valuable tool for predicting the mechanical response and temperature distributions in laminated panels with prescribed values of configuration variables. However, alternative methods are necessary for an accurate definition of the out-of-plane thermal flux distributions, unless arbitrary flux values are applied to

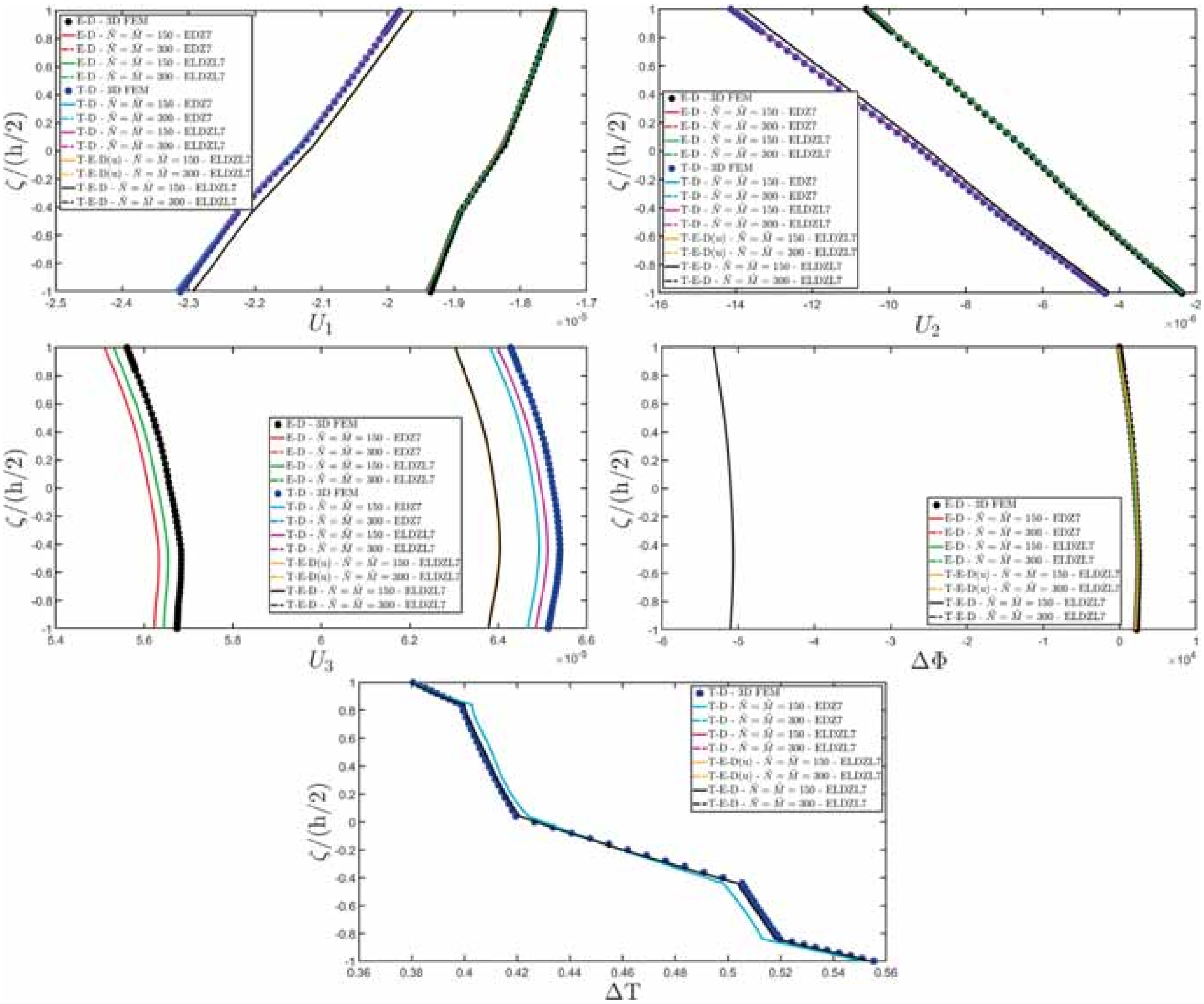

Fig. 15. Thermo-electro-mechanical analysis of a cylindrical panel under mechanical, electric, and thermal loads with various distributions. Through-the-thickness distribution of displacement field components U_1, U_2, U_3, electric potential variation $\Delta\phi$ and temperature variation ΔT expressed in [m], [V] and [K], respectively, evaluated for different values of $\widetilde{N}, \widetilde{M}$. Semi-analytical solution is derived at $(0.75L_1, 0.25L_2)$ within the two-dimensional physical domain.

the structure.

At this point, some validations are performed on the same plate to evaluate the electro-mechanical coupling. Using the same approach as in the previous simulations, a sinusoidal distribution of charge density is applied to the top and bottom sides of the same plate of the previous example, following Eqn. (41) with $\alpha = \mathrm{D}$, assuming $\overline{q}_{\mathrm{D}}^{(+)} = 0.0080\,\mathrm{C/m^2}$ and $\overline{q}_{\mathrm{D}}^{(-)} = 0.0073\,\mathrm{C/m^2}$. A reference solution is computed using a three-dimensional finite element model, developed with commercial software and employing C3D20E parabolic brick elements with piezoelectric properties. The 3D FEM-based model is characterized by 1986684 DOFs. The results form an electro-mechanical analysis, derived from the ELDZL7 higher-order theory, are presented in Figs. 6-9. Differently from the thermo-mechanical case, Fig. 6 demonstrates that the application of electric loads induces a complex zigzag profile in the displacement field components, characterized by a combination of linear and parabolic segments throughout the entire thickness. Moreover, the electric potential distribution exhibits a typical zigzag pattern. These observations are consistent with the three-dimensional strain components shown in Fig. 7, which match perfectly the reference solution. The stretching effects are more evident in this case compared to the previous analysis, as can be seen from the ε_3 profile. The through-the-thickness distributions of three-dimensional stress components are shown in Fig. 8. Based on these plots, each lamina of the plate exhibits different stress values, while respecting the stress compatibility conditions at each interface. In addition, the presence of an elastic foundation at the bottom surface induces some out-of-plane normal stresses, which are accurately predicted by the analytical model. Finally, Fig. 9 reports the electric potential gradient components and the components of the electric flux vector at $(0.25L_1, 0.75L_2)$. Also in this case, the results from the higher-order formulation match quite well those ones obtained from FEM. A similar electro-mechanical simulation is, then, performed by applying a sinusoidal distribution of electric potential to the top and bottom surfaces of the plate. More specifically, the electric potential distribution is prescribed at both external skins of the structure with magnitudes $\overline{\Delta\phi}^{(+)} = -7 \times 10^6\,\mathrm{V}$ and $\overline{\Delta\phi}^{(-)} = -6.5 \times 10^6\,\mathrm{V}$ employing the same distribution of Eqn. (84) with $\alpha = \mathrm{D}$:

$$\Delta\phi^{(\pm)}(s_1, s_2) = \overline{\Delta\phi}^{(\pm)}\widetilde{q}_{\mathrm{D}}^{(\pm)}(s_1, s_2) \tag{86}$$

The results are calculated at the same points as in the previous simulation, and they are presented in Figs. 6-9. Unlike the previous case, a slight discrepancy is now observed, especially for profiles of the in-plane displacement field and in-plane strain field. Different ε_3 profiles are

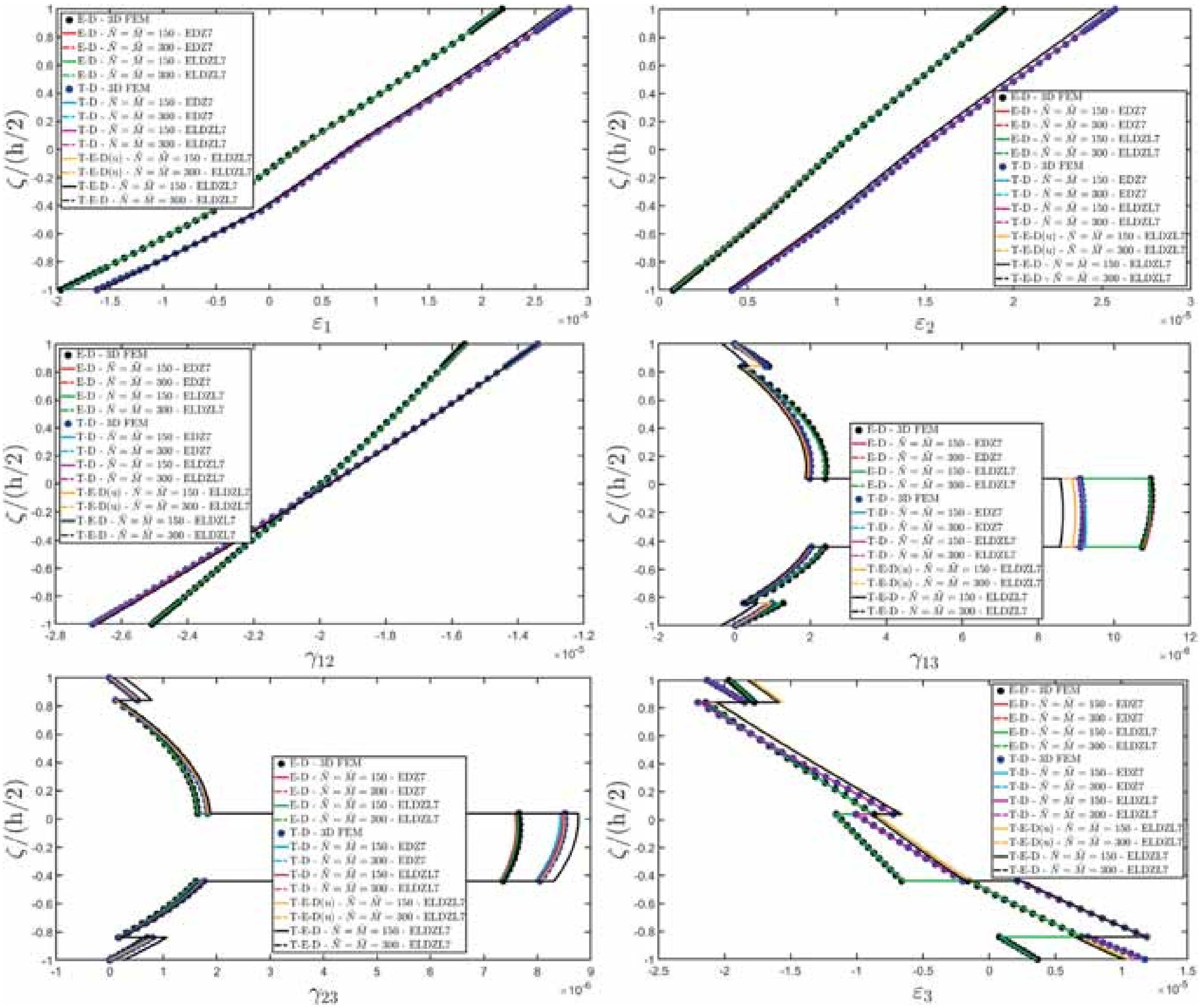

Fig. 16. Thermo-electro-mechanical analysis of a cylindrical panel under mechanical, electric, and thermal loads with various distributions. Through-the-thickness distribution of the elements of the three-dimensional strain vector $\boldsymbol{\varepsilon}(\alpha_1, \alpha_2, \zeta)$, expressed in $[\mathrm{m/m}]$, evaluated for different values of $\widetilde{N}, \widetilde{M}$. Semi-analytical solution is derived at $(0.75L_1, 0.25L_2)$ within the two-dimensional physical domain.

obtained for the first, third and the fifth laminae. Regarding the stress components shown in Fig. 8, the higher-order analytical formulation yields different profiles for σ_1 and σ_2 compared to the previous simulation, whereas FEM predictions lead to the same stress distribution. The remaining stress components are always the same. This discrepancy may be related to the variations observed in the out-of-plane electric field and electric flux distributions illustrated in Fig. 9. In this case, indeed, the analytical predictions deviate from the numerical results. For the last electric loading condition of the plate, where a sinusoidal distribution of electric flux with magnitude $\overline{q}_{\mathrm{D}}^{(+)} = 0.0080\,\mathrm{C/m^2}$ is applied at the top surface, and a sinusoidal dispersion of electric voltage with magnitude $\overline{\Delta\phi}^{(-)} = -6.5 \times 10^6\,\mathrm{V}$ is applied at the bottom surface, similar results are presented in Figs. 6-9. The results are calculated for a point located at $(0.25L_1, 0.75L_2)$ within the physical domain. Here, a behavior similar to the previous case is observed, with a minimal deviation from 3D FEM-based results. However, the analytical model achieves a higher level of accuracy in the distribution of electric field and electric flux in the thickness direction, as shown in Fig. 9. Here, the recovery procedure accounts for a prescribed value of electric flux at the top surface. At $\zeta = -h/2$, the procedure relies on the three-dimensional constitutive relation. As a consequence, the analytical results agree with the finite elements at the top surface, and a different profile is obtained at the bottom side.

In the final simulation performed on the rectangular plate, we analyze the effect of fully coupling between thermal and electric field. The results, presented in Figs. 10-14, are evaluated at $(0.25L_1, 0.75L_2)$ and show the distribution of configuration, primary, and secondary variables along the thickness direction under the influence of sinusoidal thermal and electric fluxes. The magnitudes applied at the top and bottom surfaces are $\overline{q}_h^{(+)} = -32.5347\,\mathrm{J/m^2}$, $\overline{q}_h^{(-)} = -30.2820\,\mathrm{J/m^2}$, $\overline{q}_{\mathrm{D}}^{(+)} = 0.0080\,\mathrm{C/m^2}$ and $\overline{q}_{\mathrm{D}}^{(-)} = 0.0073\,\mathrm{C/m^2}$. For completeness, we discuss, also, about the results of thermo-mechanical and electro-mechanical coupled fields derived in the previous examples. In addition, two further sets of results are provided, accounting for T-E-D(u) and T-E-D simulations. More specifically, the latter considers the full coupling among thermal, electric, and mechanical fields, including the effects of pyroelectric coupling. On the other hand, in T-E-D(u) uncoupled thermo-electro-mechanical simulations pyroelectric effects is not considered by setting the vector to a null value, namely $\overline{\boldsymbol{\Gamma}}_{\mathrm{o}}^{(k)} = [0 \quad 0 \quad 0]$ for $k = 1, \ldots, l$. The figures illustrate how the inclusion or exclusion of pyroelectric coupling affects the overall response of the plate. In the T-E-

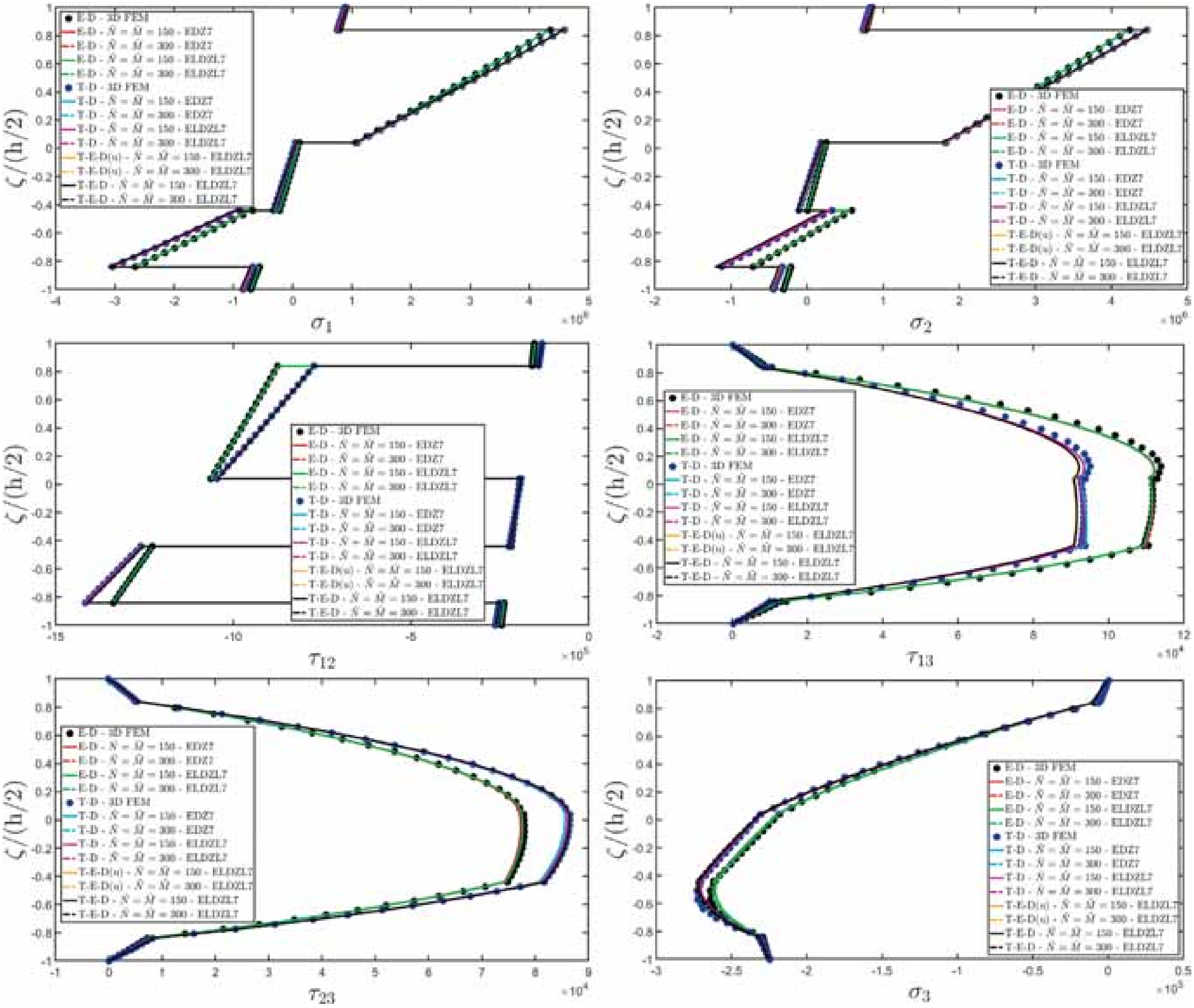

Fig. 17. Thermo-electro-mechanical analysis of a cylindrical panel under mechanical, electric, and thermal loads with various distributions. Through-the-thickness distribution of the elements of the three-dimensional stress vector $\boldsymbol{\sigma}(\alpha_1, \alpha_2, \zeta)$, expressed in $[\mathrm{N/m^2}]$, evaluated for different values of $\widetilde{N}, \widetilde{M}$. Semi-analytical solution is derived at $(0.75L_1, 0.25L_2)$ within the two-dimensional physical domain.

D(u) simulations, the results exhibit a characteristic zigzag behavior for all configuration variables, as shown in Fig. 10. This zigzag pattern reflects the combined influence of both of T-D and E-D profiles, which results in the algebraic sum of uncoupled simulations. However, when considering fully coupled T-E-D simulations, the distributions of in-plane displacement components, electric potential and temperature variation align closely with those obtained in uncoupled simulations. The difference is found for U_3 vertical deflection, which shows a translated profile. This translation highlights the impact of pyroelectric coefficients on the vertical deflection of the panel, demonstrating how fully coupling fields can affect the structural response. From Fig. 11, it is evident that the in-plane strain components are not affected by pyroelectric coupling. These strains, indeed, are solely influenced by the contributions from piezoelectric effects and thermal expansion. On the other hand, out-of-plane strain components display different profiles when pyroelectric coupling is included, thus showing its impact on distortions γ_{13} and γ_{23}. Note that the through-the-thickness profile of T-E-D(u) simulations are the sum of the T-D and E-D profiles. Fig. 12, instead, shows that the three-dimensional stress components are unaffected by pyroelectric coupling. However, a slight difference can be found in σ_3 distribution, especially near the bottom surface. This aspect can be clarified by noting that an external pressure is present due to the external elastic foundation, which depends on the U_3 displacement field component. Indeed, there is a slight deviation among the U_3 response from T-E-D simulations and that one obtained from T-E-D(u) simulations, thus resulting in different values of external pressures applied at $\zeta = -h/2$. Finally, Fig. 13 shows the results for electric field and electric flux components, while Fig. 14 presents the temperature gradient and thermal flux vectors. It is important to note that the thermal field and fluxes are not influenced by the presence of an electric field within the solid. Indeed, the curves obtained from T-E-D(u) and T-E-D simulations match those ones from T-D simulations. In the same way, the electric response of the panel is not affected by the thermal expansion, as the electric field and flux components for the E-D case are identical to those obtained from T-E-D(u). On the other hand, for a fully coupled T-E-D simulation, a different profile in the electric field and electric flux components is observed compared to the E-D simulation. This is particularly evident along the in-plane directions.

Next example involves a laminated circular cylinder. The reference surface equation accounts for s_1 as curvature direction, while s_2 corresponds to the straight direction of the panel:

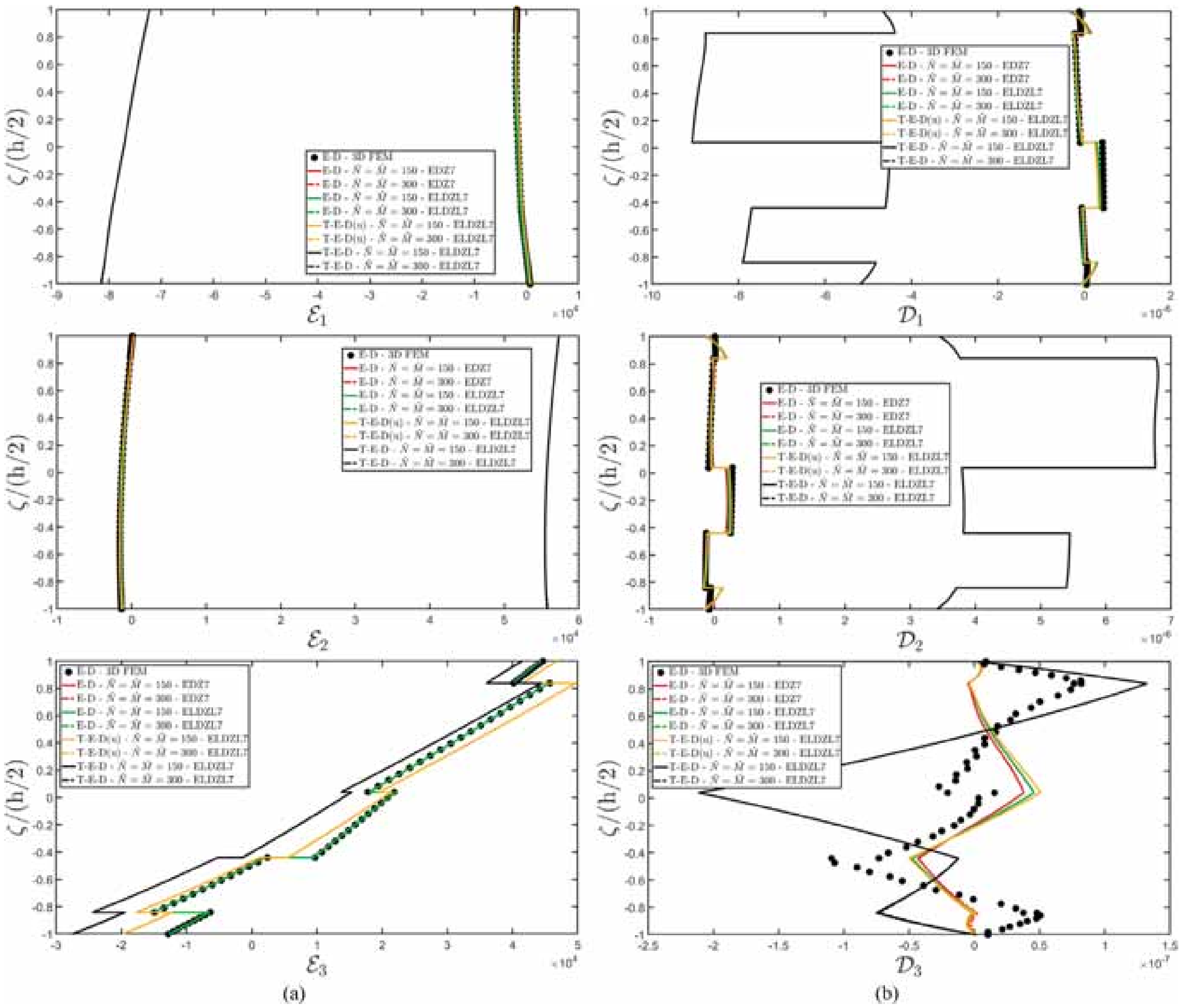

Fig. 18. Thermo-electro-mechanical analysis of a cylindrical panel under mechanical, electric, and thermal loads with various distributions. Through-the-thickness distribution of the elements of the three-dimensional electrostatic field vector $\mathscr{E}(\alpha_1, \alpha_2, \zeta)$ (a) and of the electric flux vector $\mathscr{D}(\alpha_1, \alpha_2, \zeta)$ (b), expressed in $[\mathrm{V/m}]$ and $[\mathrm{C/m^2}]$, respectively, evaluated for different values of $\widetilde{N}, \widetilde{M}$. Semi-analytical solution is derived at $(0.75L_1, 0.25L_2)$ within the two-dimensional physical domain.

$$\boldsymbol{r}(s_1, s_2) = \boldsymbol{r}(\varphi, y) = R_1 \cos\varphi\, \boldsymbol{e}_1 - y\, \boldsymbol{e}_2 + R_1 \sin\varphi\, \boldsymbol{e}_3 \tag{87}$$

Here, $R_1 = R = 0.8\,\mathrm{m}$ denotes the radius of the cylinder, while $L_2 = 2\,\mathrm{m}$ represents the height of the panel. The physical domain of Eqn. (87) is defined with $[\alpha_1^0, \alpha_1^1] \times [\alpha_2^0, \alpha_2^1] = [-\pi/2, \pi/6] \times [0, L_2]$. The lamination scheme is the same as in the rectangular plate, with a total thickness $h = 0.11\,\mathrm{m}$. The multifield response is evaluated at $(0.75L_1, 0.25L_2)$ for various loading conditions and interactions between the involved physical problems, as illustrated in Figs. 15-19. The structure is subjected to the external mechanical pressure, along with thermal and electric loads. More specifically, an external mechanical pressure with a hydrostatic distribution of magnitude $\overline{q}_3^{(-)} = 3 \times 10^5\,\mathrm{N/m^2}$ is applied to the bottom surface in all simulations:

$$q_3^{(-)}(s_1, s_2) = \overline{q}_3^{(-)} \frac{s_1}{L_1} \tag{88}$$

The following expression is assumed for the semi-analytical coefficients $Q_{3nm}^{(-)}$ for an arbitrary $n = 1, \ldots, \widetilde{N}$ and $m = 1, \ldots, \widetilde{M}$ in Eqn. (58):

$$Q_{3nm}^{(-)} = -\frac{4\overline{q}_3^{(-)}}{\pi^2 nm} \cos(n\pi)(1 - \cos(m\pi)) \tag{89}$$

On the other hand, electric loads are applied to the top and bottom surfaces using a hydrostatic distribution along the straight direction:

$$q_{\mathrm{D}}^{(\pm)}(s_1, s_2) = \overline{q}_{\mathrm{D}}^{(\pm)} \frac{s_2}{L_2} \tag{90}$$

where $\overline{q}_{\mathrm{D}}^{(+)} = 8 \times 10^{-9}\,\mathrm{C/m^2}$ and $\overline{q}_{\mathrm{D}}^{(-)} = 7 \times 10^{-9}\,\mathrm{C/m^2}$ are the corresponding load magnitudes. The following expression is, therefore, adopted for coefficients $Q_{\mathrm{D}nm}^{(+)}, Q_{\mathrm{D}nm}^{(-)}$ in the trigonometric Fourier expansion of Eqn. (90):

$$Q_{\mathrm{D}nm}^{(\pm)} = -\frac{4\overline{q}_{\mathrm{D}}^{(\pm)}}{\pi^2 nm} (1 - \cos(n\pi)) \cos(m\pi) \tag{91}$$

Furthermore, uniformly distributed thermal loads with magnitudes $\overline{q}_h^{(+)} = 1\,\mathrm{J/m^2}$ and $\overline{q}_h^{(-)} = 2\,\mathrm{J/m^2}$ are applied to the cylinder:

$$q_h^{(\pm)}(s_1, s_2) = \overline{q}_h^{(\pm)} \tag{92}$$

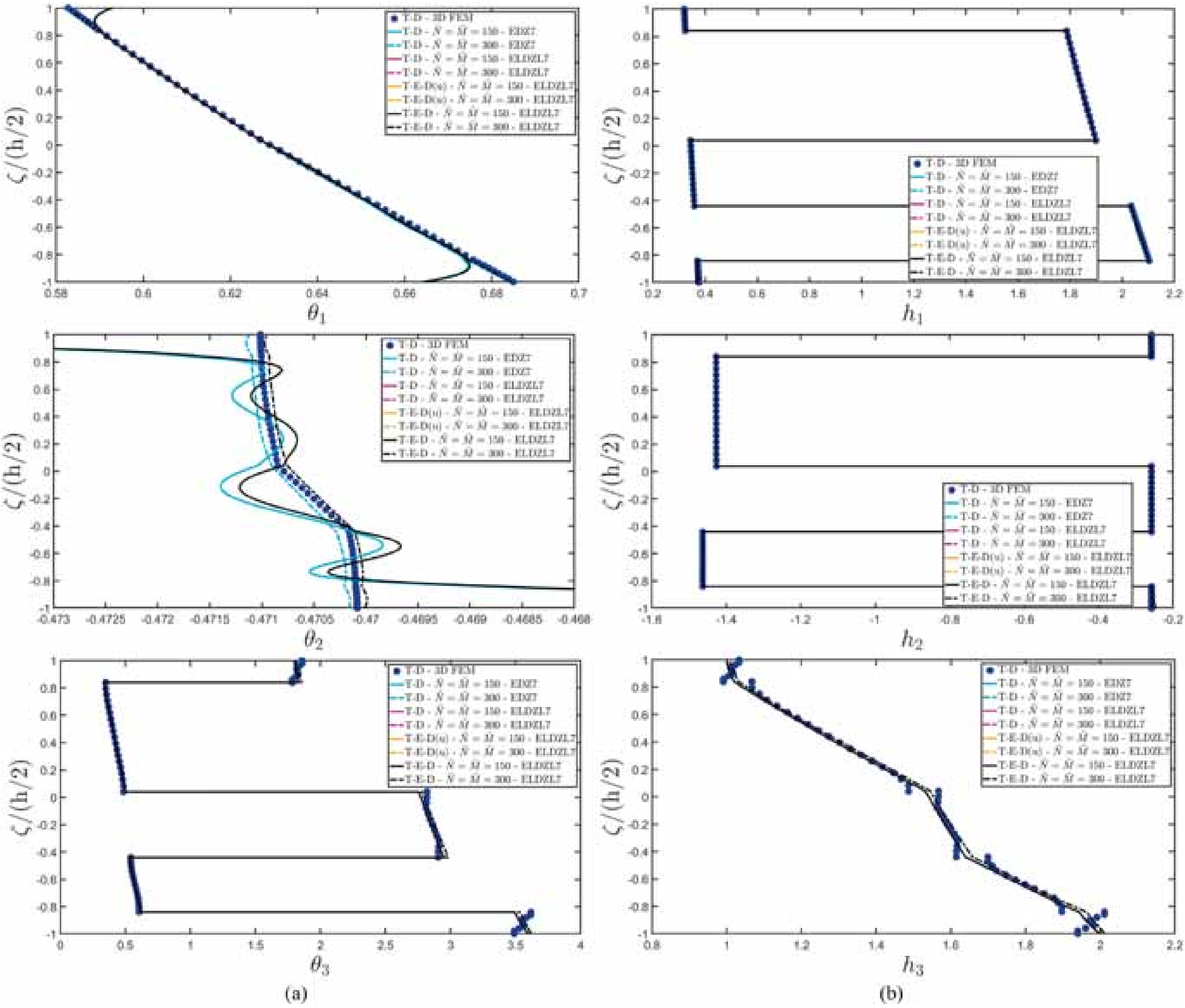

Fig. 19. Thermo-electro-mechanical analysis of a cylindrical panel under mechanical, electric, and thermal loads with various distributions. Through-the-thickness distribution of the elements of the three-dimensional temperature gradient vector $\boldsymbol{\theta}(\alpha_1, \alpha_2, \zeta)$ (a) and of the thermal flux vector $\boldsymbol{h}(\alpha_1, \alpha_2, \zeta)$ (b), expressed in $[\mathrm{K/m}]$ and $[\mathrm{J/m^2}]$, respectively, evaluated for different values of $\widetilde{N}, \widetilde{M}$. Semi-analytical solution is derived at $(0.75L_1, 0.25L_2)$ within the two-dimensional physical domain.

The trigonometric expansion coefficients $Q_{hnm}^{(+)}, Q_{hnm}^{(-)}$ used in Eqn. (58) for the expansion in Eqn. (92) are evaluated for any $n = 1, \ldots, \widetilde{N}$ and $m = 1, \ldots, \widetilde{M}$ as follows:

$$Q_{hnm}^{(\pm)} = \frac{4\overline{q}_h^{(\pm)}}{\pi^2 nm}(1 - \cos(n\pi))(1 - \cos(m\pi)) \tag{93}$$

The first set of simulations accounts for the electro-mechanical response of the panel under mechanical load (88) and electric fluxes. A finite element E-D model is developed to provide a three-dimensional reference solution, consisting of 2735180 DOFs. A semi-analytical solution is evaluated using the present formulation with different numbers $\widetilde{N}, \widetilde{M}$ of expansion terms. The simulations are conducted with both ELW and ESL theories. In this load case, classical ESL thickness functions are adopted because the loading conditions applied fluxes, with no values for configuration variables at the top and bottom surfaces. Then, the thermo-mechanical problem is solved for the same structure, and the results are also derived from a 3D FEM model, as well as with ELW and ESL formulations. As shown in Fig. 15, for $\widetilde{N} = \widetilde{M} = 300$, the numerical predictions for the displacement field components and electric potential are very similar to those ones from 3D FEM analysis. Moreover, the zigzag behavior is particularly evident in the T-D displacement field components, and a piecewise linear profile is observed for the temperature variation, while the electric potential shows a smoother distribution. Similar observations can be repeated for three-dimensional strain components reported in Fig. 16. In particular, in-plane strains $\varepsilon_1, \varepsilon_2$ exhibit a linear profile along the entire thickness of the cylinder, while ε_3 shows a piecewise linear distribution in both E-D and T-D simulations. In any case, as the number of semi-analytical terms increases, the results converge. Fig. 17 shows the thickness plots of the three-dimensional stress components. Referring to E-D simulations, the results match well the reference solution, and the loading conditions are accurately satisfied through the equilibrium-based recovery procedure. In addition, the T-D semi-analytical model demonstrates more rapid convergence of results with increasing terms $\widetilde{N}, \widetilde{M}$. When solving T-E-D (u) and T-E-D problems, it is observed that pyroelectric contributions are negligible in the overall mechanical response of the laminate compared to the T-D and E-D numerical predictions, except for the vertical deflection U_3. The three-dimensional strain components are only slightly influenced in some layers for the out-of-plane distortions, while

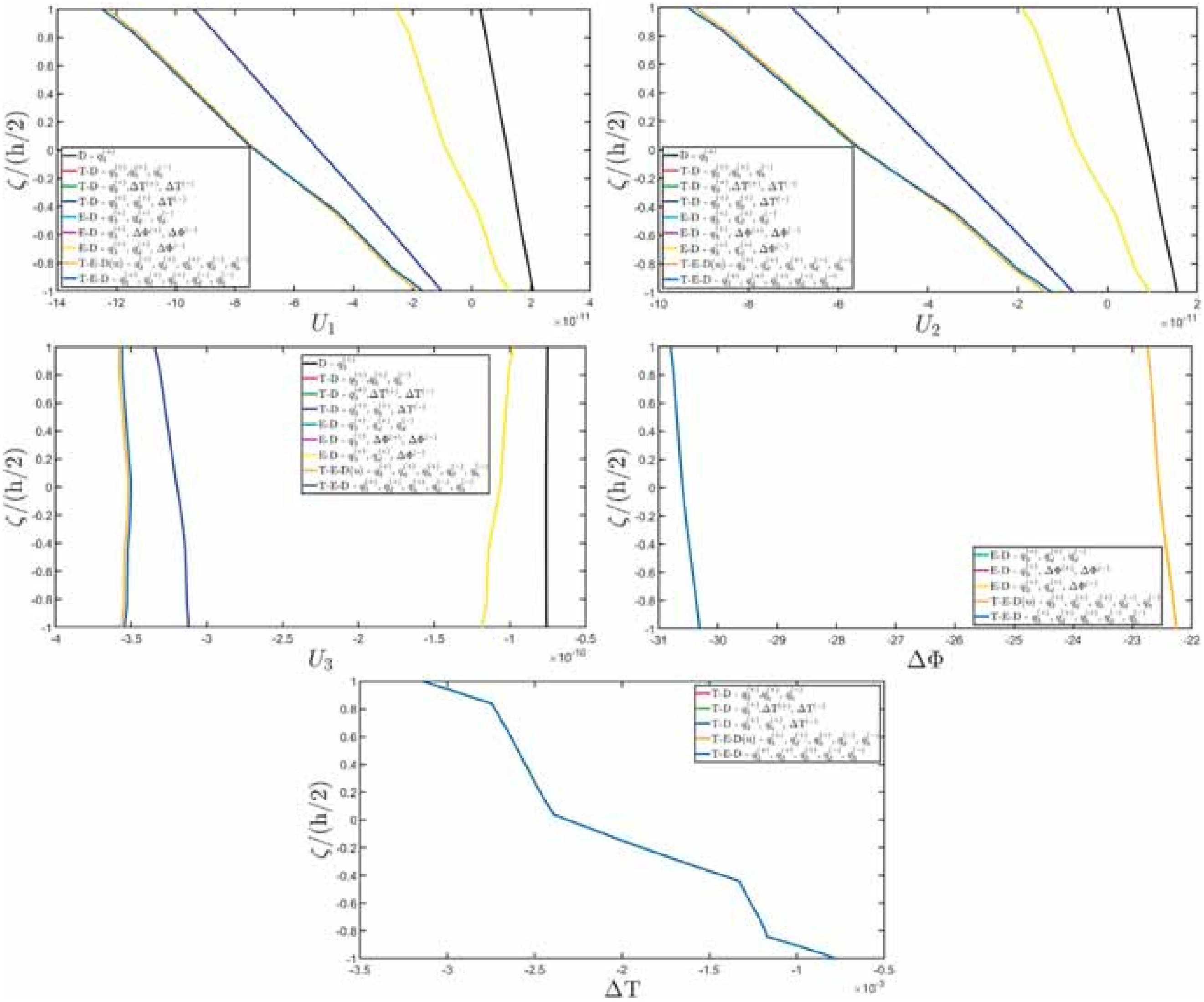

Fig. 20. Thermo-electro-mechanical analysis of a laminated spherical panel under mechanical, electric, and thermal loads with sinusoidal distribution. Through-the-thickness distribution of displacement field components U_1, U_2, U_3, electric potential variation $\Delta\phi$ and temperature variation ΔT expressed in [m], [V] and [K], respectively, evaluated at $(0.75L_1, 0.75L_2)$ within the two-dimensional physical domain employing the ELDZL7 kinematic model.

the stress distribution remains unchanged. The effect of thermo-electric coupling is more pronounced in the electric field components and electric flux distributions along the thickness direction, as shown in Fig. 18, particularly when the pyroelectric effect is included in the model. On the other hand, Fig. 19 indicates that the thickness plots of thermal primary and secondary variables are not influenced by the presence of an electric field within the laminate. Furthermore, it is worth observing that temperature gradient components are well predicted only when a higher number of harmonic expansion terms are used in the simulation ($\widetilde{N} = \widetilde{M} = 300$). When $\widetilde{N} = \widetilde{M} = 150$, indeed, the in-plane temperature gradient profile does not match the 3D FEM numerical predictions. On the other hand, the elements of the thermal flux vector are accurately predicted even with a lower number of expansion terms.

The last numerical example focuses on the thermo-electro-mechanical behavior of a spherical panel with radius $R_1 = R_2 = 0.03\,\mathrm{m}$. The two-dimensional physical domain required to define the reference surface in Eqn. (1), is such that $[\alpha_1^0, \alpha_1^1] \times [\alpha_2^0, \alpha_2^1] = [75, 105] \times [-20, 20]$ *deg*. The lamination scheme employs the same material sequence of the previous simulations, namely (ETE - 1/ETE - 3/ETE - 1/ETE - 2/ETE - 1) with (0/0/0/0/0), but with layers thicknesses equal to $h_2 = h_5 = 0.0001\,\mathrm{m}$, $h_2 = 0.00025\,\mathrm{m}$, $h_3 = 0.0003\,\mathrm{m}$ and $h_4 = 0.0005\,\mathrm{m}$. The structure is subjected to sinusoidal distributions of mechanical, thermal, and electric loads, defined according to Eqn. (84) with $\alpha = 3, \mathrm{D}, h$. The corresponding load magnitudes are provided as $\overline{q}_3^{(+)} = -75\,\mathrm{N/m^2}$, $\overline{q}_\mathrm{D}^{(+)} = 1.6\times 10^{-6}\,\mathrm{C/m^2}$, $\overline{q}_\mathrm{D}^{(-)} = 1.4\times 10^{-6}\,\mathrm{C/m^2}$, $\overline{q}_h^{(+)} = 4.4\,\mathrm{J/m^2}$ and $\overline{q}_h^{(-)} = 4.08\,\mathrm{J/m^2}$. The structure rests on an elastic foundation, following the Winkler-Pasternak model, located at the bottom surface with an elastic stiffness $k_{3f}^{(-)} = 5\times 10^7\,\mathrm{N/m^3}$, while the foundation shear modulus is $G_f^{(-)} = 5\times 10^6\,\mathrm{N/m^2}$. The results are evaluated at $(0.75L_1, 0.75L_2)$ within the physical domain, and consist of through-the-thickness distributions of multifield configuration, primary, and secondary variables of the physical problems. These results are presented in Figs. 20-24. This example enhances the investigations previously reported for the laminated rectangular plate. In this case, the structure exhibits a double curvature, and it is also subjected to mechanical and multifield external loads. The displacement field profiles can be found in Fig. 20, along with the distributions of electric potential and temperature increment. The overall deflection of the panel due to the thermal and electric loads is characterized by a zigzag and linear behaviour, respectively. In contrast, the deflection contribution from mechanical loads results in a linear dispersion of the

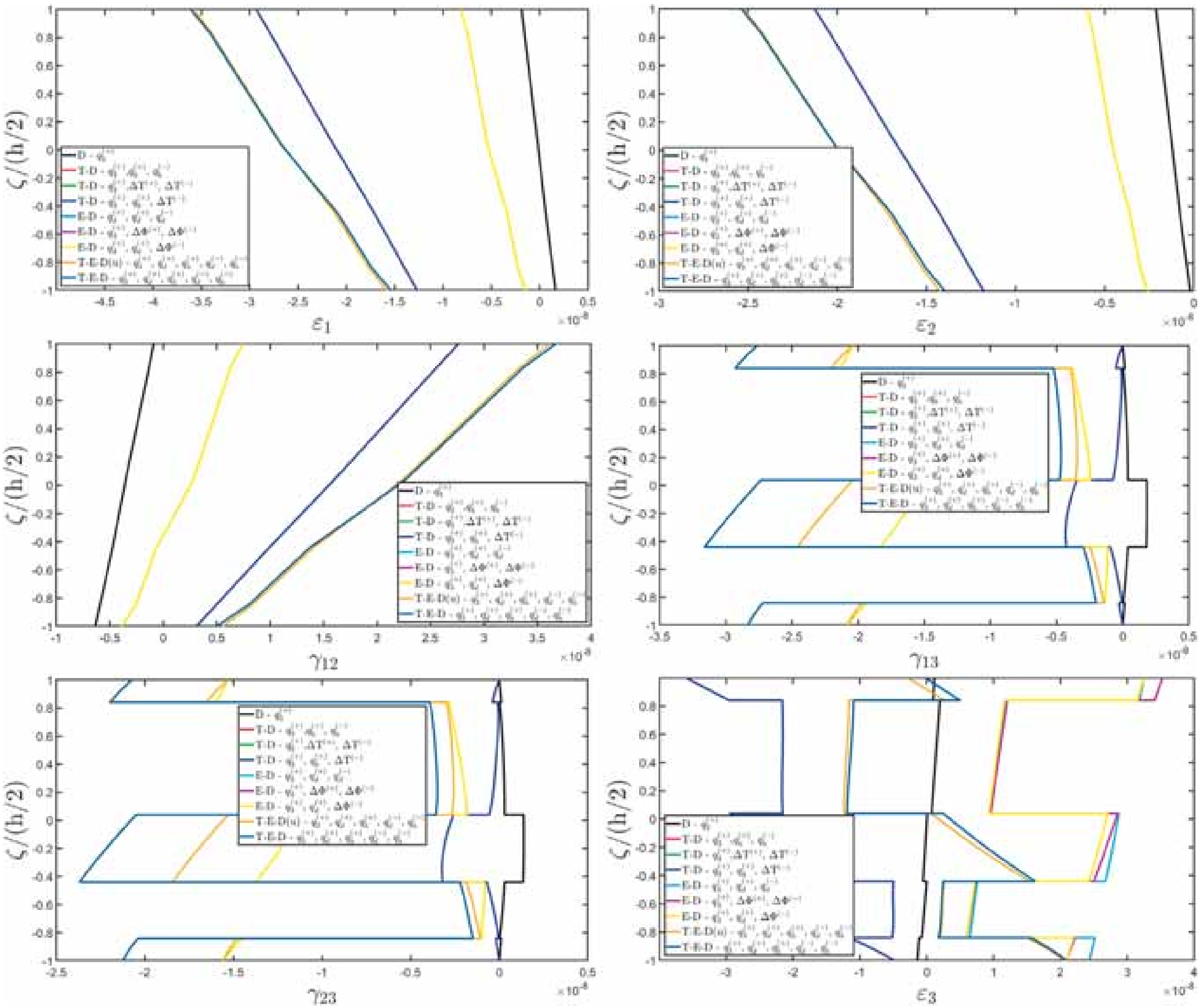

Fig. 21. Thermo-electro-mechanical analysis of a laminated spherical panel under mechanical, electric, and thermal loads with sinusoidal distribution. Through-the-thickness distribution of the elements of the three-dimensional strain vector $\boldsymbol{\varepsilon}(\alpha_1, \alpha_2, \zeta)$, expressed in [m/m], evaluated at $(0.75L_1, 0.75L_2)$ within the two-dimensional physical domain employing the ELDZL7 kinematic model.

in-plane displacement components and a uniform distribution of the out-of-plane displacement field. When T-E-D(u) simulations are considered, the total displacement field is obtained as summation of contributions from each individual load. The T-E-D results show a slight translation in the out-of-plane displacement field profile. On the other hand, the electric potential from E-D simulations changes when the additional effect of the thermal field is considered, even for an uncoupled analysis. This happens because the deflection of the panel due to thermal expansion induces an additional electric field resulting from piezoelectricity. In Fig. 21, the three-dimensional strain components exhibit a linear profile for in-plane axial strains, while non-uniform values of out-of-plane strain ε_3 are observed between adjacent laminae. In addition, each layer of the stacking sequence shows distinct out-of-plane distortion profiles, indicating that the variations in the volume fraction of cylindrical fibers affect the thermo-electro-mechanical properties of the homogenized material. On the other hand, the through-the-thickness stress profiles shown in Fig. 22 reveal higher shear stress magnitudes in laminae with lower distortions across all multifield simulations. This results from the cross-ply behavior of the laminae, which is characterized by uncoupled shear stresses from axial deformations. It is important to note that the σ_3 stress distribution is affected by the loading and boundary conditions. In particular, the application of the recovery procedure ensures the fulfillment of the mechanical loading conditions at the top surface, while the stress values are different at the bottom surface in different simulations. In absence of a mechanical surface pressure at the bottom side, the recovery procedure uses the stress value obtained from the elastic foundation model, depending on the vertical deflection U_3 of the structure. Fig. 23 shows the electric field and electric flux components. As expected, the introduction of the pyroelectric effect into the model results in an additional contribution to the electric field, causing a shift in the curve obtained from uncoupled T-E-D (u) analysis, particularly evident along the in-plane directions. Regarding the electric flux components, stepwise profiles are observed for $\mathscr{D}_1$ and $\mathscr{D}_2$ due to variations in the dielectric properties of the laminae. On the other hand, the $\mathscr{D}_3$ distribution shows only a variation in slope among adjacent layers. In addition, the coupling between physical phenomena leads to different profiles for electric quantities. However, the thermal primary and secondary variables are not significantly influenced by multifield coupling, as illustrated in Fig. 24. Here, the in-plane temperature gradient and thermal flux components depend only on the thermal loading conditions, while the introduction of an electric field causes a variation near the bottom surface of the panel. It

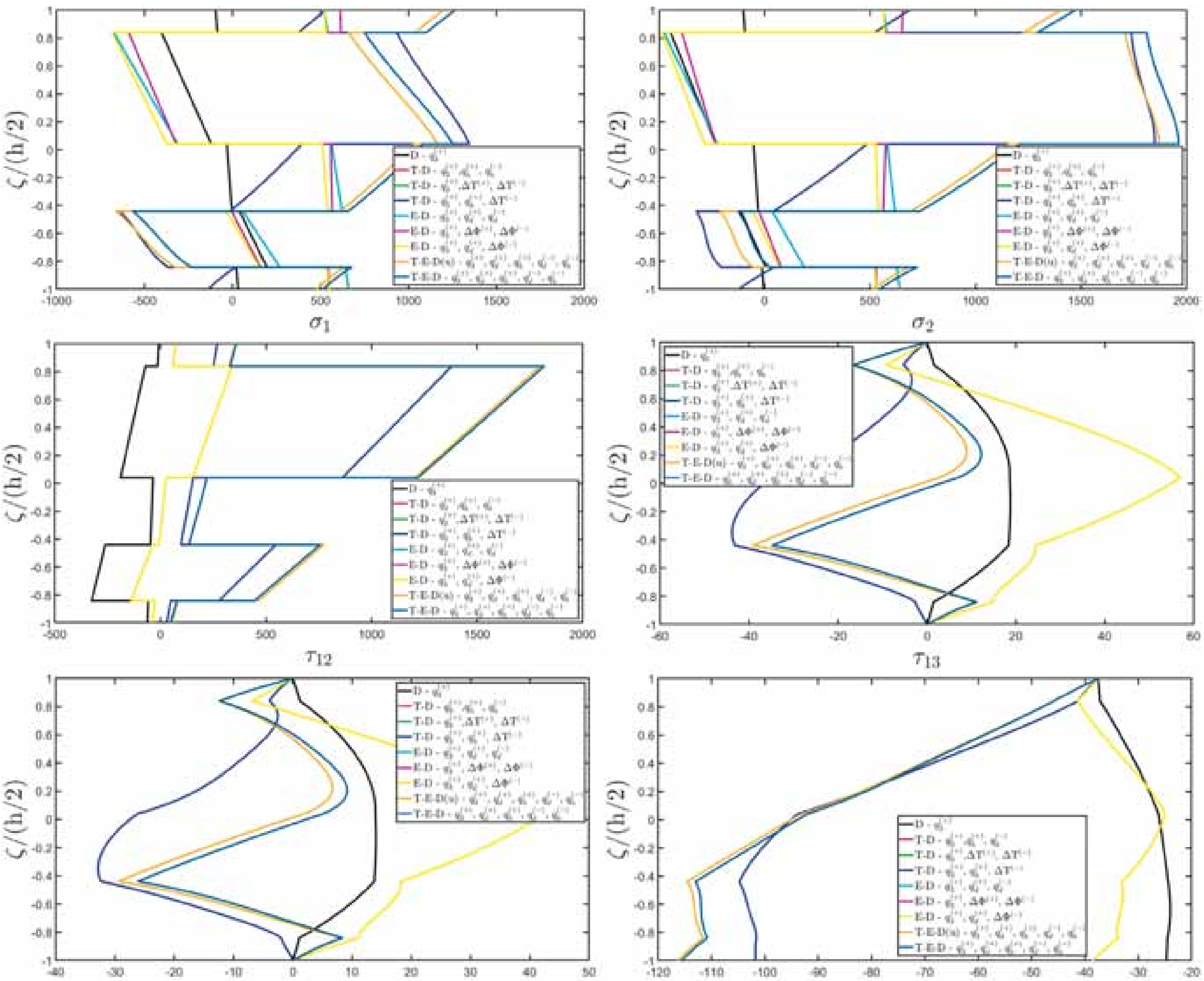

Fig. 22. Thermo-electro-mechanical analysis of a laminated spherical panel under mechanical, electric, and thermal loads with sinusoidal distribution. Through-the-thickness distribution of the elements of the three-dimensional stress vector $\boldsymbol{\sigma}(\alpha_1, \alpha_2, \zeta)$, expressed in $[\mathrm{N/m^2}]$, evaluated at $(0.75L_1, 0.75L_2)$ within the two-dimensional physical domain employing the ELDZL7 kinematic model.

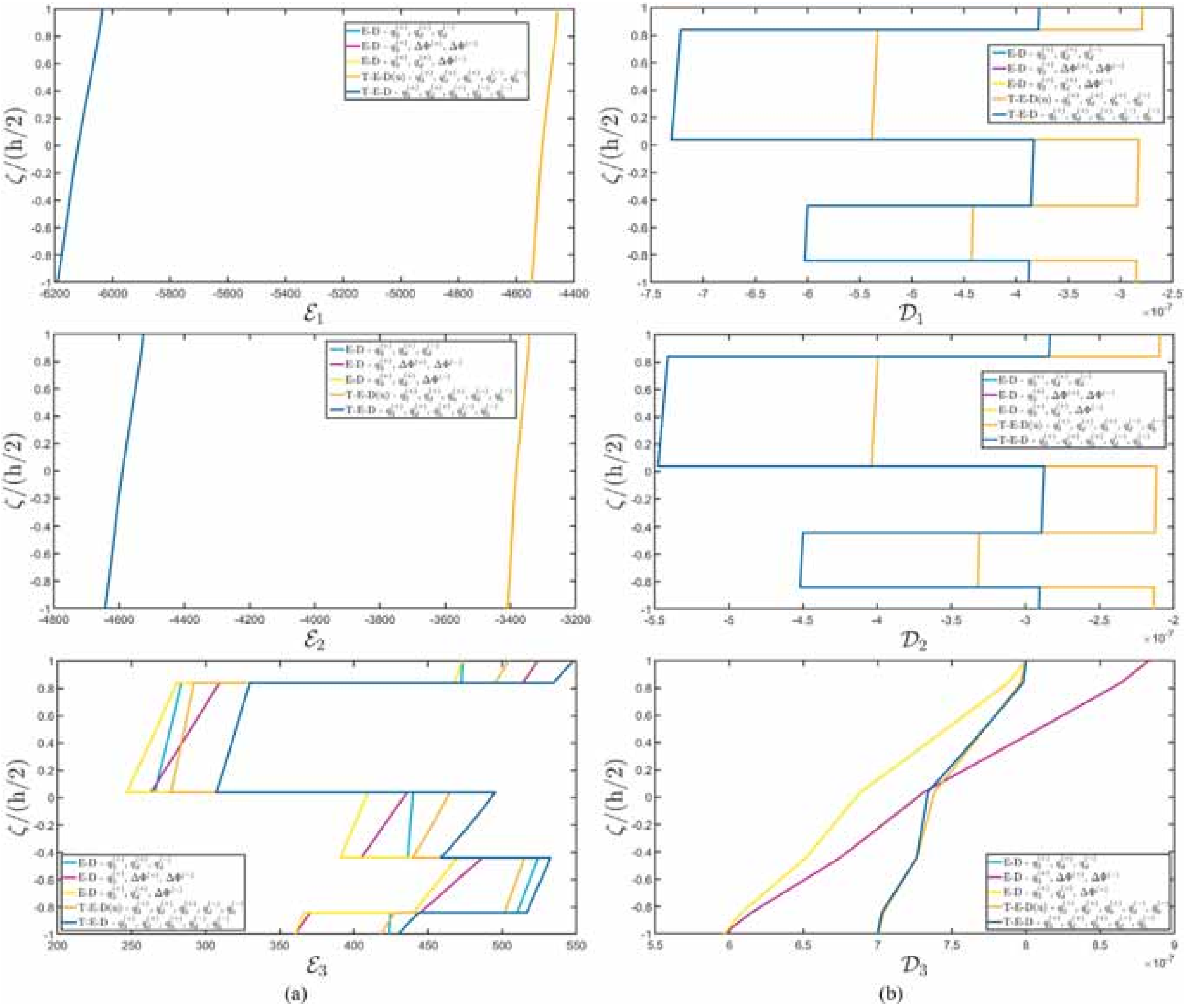

Fig. 23. Thermo-electro-mechanical analysis of a laminated spherical panel under mechanical, electric, and thermal loads with sinusoidal distribution. Through-the-thickness distribution of the elements of the electrostatic field vector $\mathscr{E}(\alpha_1, \alpha_2, \zeta)$ (a) and of the electric flux vector $\mathscr{D}(\alpha_1, \alpha_2, \zeta)$ (b), expressed in $[\mathrm{V/m}]$ and $[\mathrm{C/m^2}]$, respectively, evaluated at $(0.75L_1, 0.75L_2)$ within the two-dimensional physical domain employing the ELDZL7 kinematic model.

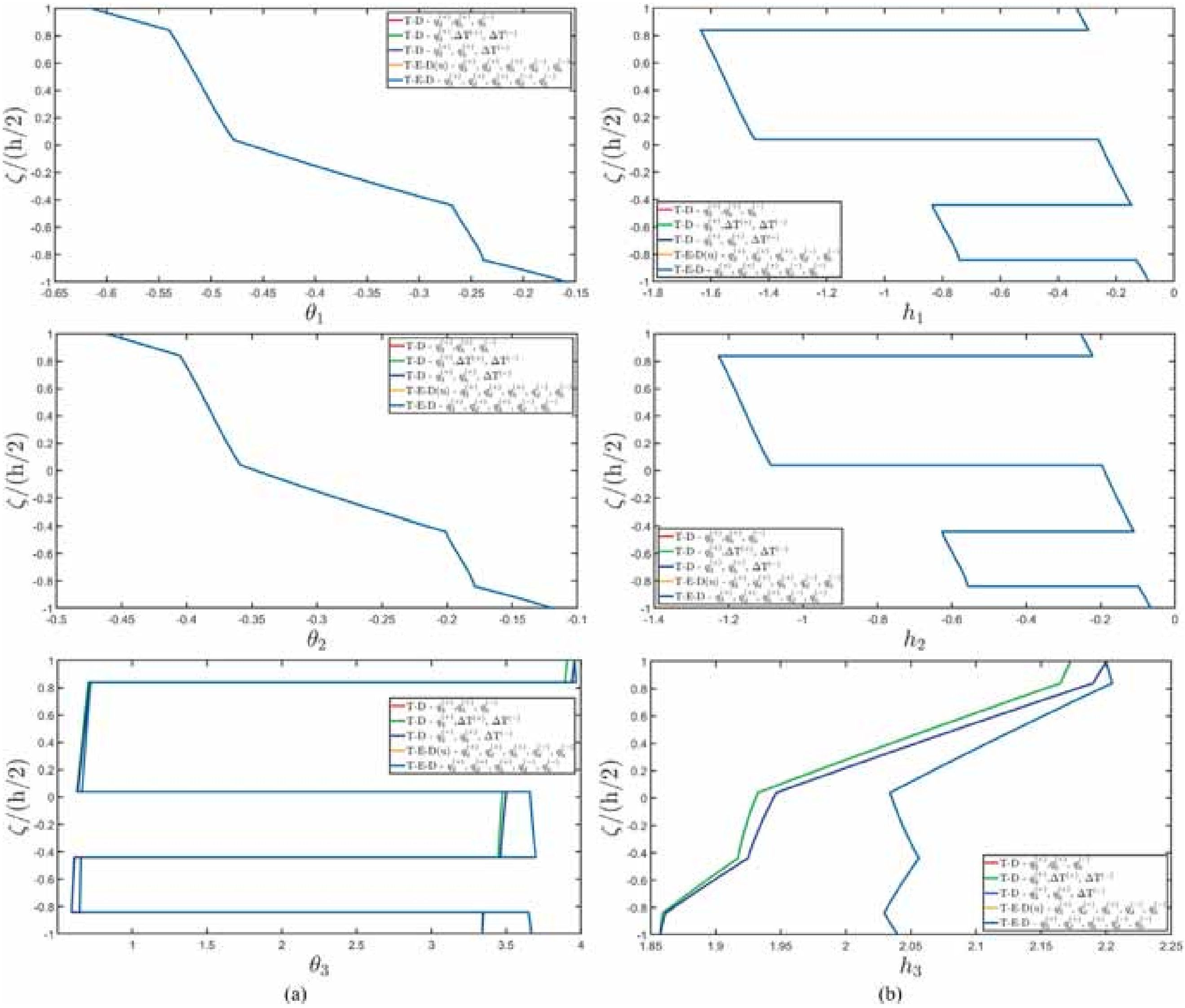

Fig. 24. Thermo-electro-mechanical analysis of a laminated spherical panel under mechanical, electric, and thermal loads with sinusoidal distribution. Through-the-thickness distribution of the elements of the temperature gradient vector $\boldsymbol{\theta}(\alpha_1, \alpha_2, \zeta)$ (a) and of the thermal flux vector $\boldsymbol{h}(\alpha_1, \alpha_2, \zeta)$ (b), expressed in $[\mathrm{K/m}]$ and $[\mathrm{J/m^2}]$, respectively, evaluated at $(0.75L_1, 0.75L_2)$ within the two-dimensional physical domain employing the ELDZL7 kinematic model.

should be noted that pyroelectric coefficients affect only the electric response, while thermal quantities remain consistent between T-E-D(u) and T-E-D simulations. Finally, when thermal loading conditions consist of prescribed temperature values, the through-the-thickness distributions obtained from the analysis are similar at the bottom surface, with a slight variation only at the top surface.

6. Conclusion

The work has introduced a novel two-dimensional formulation based on a generalized kinematic model for the multifield analysis of curved laminated panels made of innovative smart materials. The proposed theory considers a full coupling between thermal conduction, electricity, and mechanical elasticity in the physical problems. The fundamental equations, derived from the Master Balance principle, have been expressed in curvilinear principal coordinates and allows for the application of surface loads with various distributions, including mechanical, electrical, and thermal loads, as well as prescribed displacements, electric voltages, and temperature variations. A semi-analytical Navier solution has been developed, and the three-dimensional multifield response of the laminate has been obtained using a GDQ-based recovery procedure. Various numerical applications have demonstrated the efficiency of the formulation for both straight and curved laminated structures, evaluating the thermo-electro-mechanical response under different loading conditions. The results have been shown to match well predictions from highly demanding finite-element models. Furthermore, the study has explored some coupling effects not typically considered in commercial software, pointing out their impact on the overall structural response. At the present stage of the research, the solution is suitable only for specific geometries, material symmetries, and boundary conditions, even though the formulation is general. Furthermore, it allows for the prescription of temperature and electric potential only at the top and bottom surface. As a consequence, it is required that all layers exhibit thermal and electric properties. A possible enhancement of the theory can thus be its extension to a layer-wise formulation. Furthermore, a numerical solution can be implemented to analyze structures of various geometries, materials and external constraints. In this way, new possible multifield applications can be studied involving curved laminated structures.

CRediT authorship contribution statement

Francesco Tornabene: Writing – review & editing, Writing – original draft, Validation, Supervision, Software, Resources, Methodology, Investigation, Formal analysis, Data curation, Conceptualization. **Matteo Viscoti:** Writing – original draft, Investigation, Formal analysis, Data curation. **Rossana Dimitri:** Writing – review & editing, Supervision, Investigation, Formal analysis, Data curation.

Declaration of competing interest

The authors declare that they have no known competing financial interests or personal relationships that could have appeared to influence the work reported in this paper.

Data availability

No data was used for the research described in the article.

References

[1] Tzou HS, Tseng CI. Distributed piezoelectric sensor/actuator design for dynamic measurement/control of distributed parameter systems: a piezoelectric finite element approach. J Sound Vib 1990;138:17–34.

[2] Narita F, Fox M. A review on piezoelectric, magnetostrictive, and magnetoelectric materials and device technologies for energy harvesting applications. Adv Eng Mater 2018;20:1700743.

[3] Sandvand Å, Halvorsen E, Aasmundtveit KE, Jakobsen H. Identification and elimination of hygro-thermo-mechanical stress-effects in a high-precision MEMS pressure sensor. J Microelectromech Syst 2017;26:415–23.

[4] G.C. Sih, J.G. Michopoulos, S.C. Chou, Hygrothermoelasticity, Martinus Nijhoff Publishers, 1986.

[5] Wang J, Yang Y. Higher-order theories of piezoelectric plates and applications. Appl Mech Rev 2000;53:87–99.

[6] Kapuria S, Kumari P, Nath JK. Efficient modeling of smart piezoelectric composite laminates: a review. Acta Mech 2010;214:31–48.

[7] Safaei M, Sodano HA, Anton SR. A review of energy harvesting using piezoelectric materials: state-of-the-art a decade later (2008–2018). Smart Mater Struct 2019;28:113001.

[8] Rahmoune M, Benjeddou A, Ohayon R, Osmont D. New thin piezoelectric plate models. J Intell Mater Syst Struct 1998;9:1017–29.

[9] Tzou HS. Piezoelectric shells: Distributed sensing and control of continua. Kluwer Academic Publishers; 1993.

[10] Hong CC. Transient responses of magnetostrictive plates by using the GDQ method. European Journal of Mechanics-A/Solids 2010;29:1015–21.

[11] Ye W, Liu J, Zang Q, Lin G. Investigation of bending behavior for laminated composite magneto-electro-elastic cylindrical shells subjected to mechanical or electric/magnetic loads. Comput Math Appl 2020;80:1839–57.

[12] Osaretin IA, Rojas RG. Theoretical model for the magnetoelectric effect in magnetostrictive/piezoelectric composites. Phys Rev B 2010;82:174415.

[13] Monge JC, Mantari JL. Thermal bending response of functionally graded magneto-electric–elastic shell employing non-polynomial model. Mech Adv Mater Struct 2023;30:2882–98.

[14] Sokolnikoff IS. Mathematical theory of elasticity. New York: Mc-Graw Hill; 1956.

[15] Reddy JN. Mechanics of laminated composite plates and shells: theory and analysis. Boca Raton: CRC Press; 2003.

[16] Reddy JN, Robbins Jr DH. Theories and computational models for composite laminates. Appl Mech Rev 1994;47:147–69.

[17] Tornabene F, Viscoti M, Dimitri R, Reddy JN. Higher order theories for the vibration study of doubly-curved anisotropic shells with a variable thickness and isogeometric mapped geometry. Compos Struct 2021;267:113829.

[18] Washizu K. Variational Methods in Elasticity & Plasticity. Oxford: Pergamon Press; 1975.

[19] Reddy JN. A generalization of two-dimensional theories of laminated composite plates. Communications in Applied Numerical Methods 1987;3:173–80.

[20] Reddy JN. An evaluation of equivalent-single-layer and layerwise theories of composite laminates. Compos Struct 1993;25:21–35.

[21] Liew KM, Pan ZZ, Zhang LW. An overview of layerwise theories for composite laminates and structures: Development, numerical implementation and application. Compos Struct 2019;216:240–59.

[22] Tornabene F, Viscoti M, Dimitri R. Static analysis of anisotropic doubly-curved shell subjected to concentrated loads employing higher order layer-wise theories, Computer Methods in Engineering. Science 2022:22237.

[23] Tornabene F, Viscoti M, Dimitri R. Equivalent single layer higher order theory based on a weak formulation for the dynamic analysis of anisotropic doubly-curved shells with arbitrary geometry and variable thickness. Thin-Walled Struct 2022;174:109119.

[24] Thai HT, Kim SE. A simple higher-order shear deformation theory for bending and free vibration analysis of functionally graded plates. Compos Struct 2013;96:165–73.

[25] Al-Osta MA. An exponential-trigonometric quasi-3D HSDT for wave propagation in an exponentially graded plate with microstructural defects. Compos Struct 2022;297:115984.

[26] Mantari JL, Soares CG. Bending analysis of thick exponentially graded plates using a new trigonometric higher order shear deformation theory. Compos Struct 2012;94:1991–2000.

[27] Hoang VNV, Thanh PT. A new trigonometric shear deformation plate theory for free vibration analysis of FGM plates with two-directional variable thickness. Thin-Walled Struct 2024;194:111310.

[28] Bouazza M, Lairedj A, Benseddiq N, Khalki S. A refined hyperbolic shear deformation theory for thermal buckling analysis of cross-ply laminated plates. Mech Res Commun 2016;73:117–26.

[29] Icardi U, Sola F. Assessment of recent zig-zag theories for laminated and sandwich structures. Compos B Eng 2016;97:26–52.

[30] Murakami H. Laminated Composite Plate Theory with Improved In-Plane Responses. ASME Journal of Applied Mechanics 1986;53:661–6.

[31] Iurlaro L, Gherlone M, Di Sciuva M, Tessler A. Assessment of the refined zigzag theory for bending, vibration, and buckling of sandwich plates: a comparative study of different theories. Compos Struct 2013;106:777–92.

[32] Tessler A, Di Sciuva M, Gherlone M. A refined zigzag beam theory for composite and sandwich beams. J Compos Mater 2009;43:1051–81.

[33] Mantari JL, Oktem AS, Soares CG. Bending response of functionally graded plates by using a new higher order shear deformation theory. Compos Struct 2012;94:714–23.

[34] Milazzo A. Layer-wise and equivalent single layer models for smart multilayered plates. Compos B Eng 2014;67:62–75.

[35] Tornabene F, Viscoti M, Dimitri R. Equivalent Layer-Wise theory for the hygro-thermo-magneto-electro-elastic analysis of laminated curved shells. Thin-Walled Struct 2024;198:111751.

[36] Tornabene F, Viscoti M, Dimitri R. Thermo-Mechanical analysis of laminated Doubly-Curved Shells: Higher order Equivalent Layer-Wise formulation. Compos Struct 2024;335:117995.

[37] Tornabene F, Fantuzzi N, Bacciocchi M, Reddy JN. An equivalent layer-wise approach for the free vibration analysis of thick and thin laminated and sandwich shells. Appl Sci 2016;7:17.
[38] Tornabene F. Hygro-Thermo-Magneto-Electro-Elastic Theory of Anisotropic Doubly-Curved Shells. Bologna: Esculapio; 2023.
[39] Tiersten HF, Mindlin RD. Forced vibrations of piezoelectric crystal plates. Q Appl Math 1962;20:107–19.
[40] Khare RK, Kant T, Garg AK. Closed-form thermo-mechanical solutions of higher-order theories of cross-ply laminated shallow shells. Compos Struct 2003;59:313–40.
[41] Cho M, Oh J. Higher order zig-zag theory for fully coupled thermo-electric–mechanical smart composite plates. Int J Solids Struct 2004;41:1331–56.
[42] Arefi M, Zenkour AM. Thermo-electro-mechanical bending behavior of sandwich nanoplate integrated with piezoelectric face-sheets based on trigonometric plate theory. Compos Struct 2017;162:108–22.
[43] Tounsi A, Houari MSA, Benyoucef S. A refined trigonometric shear deformation theory for thermoelastic bending of functionally graded sandwich plates. Aerosp Sci Technol 2013;24:209–20.
[44] Zenkour AM, Hafed ZS. Bending analysis of functionally graded piezoelectric plates via quasi-3D trigonometric theory. Mech Adv Mater Struct 2020;27:1551–62.
[45] Tornabene F, Viscoti M, Dimitri R. Free vibration analysis of laminated anisotropic doubly-curved shell structures reinforced with three-phase polymer/CNT/fiber material. Eng Anal Bound Elem 2024;164:105762.
[46] Saleh B, et al. 30 Years of functionally graded materials: An overview of manufacturing methods. Applications and Future Challenges, Composites Part B: Engineering 2020;201:108376.
[47] Hollister SJ, Kikuchi N. A comparison of homogenization and standard mechanics analyses for periodic porous composites. Comput Mech 1992;10:73–95.
[48] Affdl JH, Kardos JL. The Halpin-Tsai equations: a review. Polym Eng Sci 1976;16:344–52.
[49] Nemat-Nasser S, Hori M. Micromechanics: overall properties of heterogeneous materials. Amsterdam: Elsevier; 2013.
[50] Tsai S, Hann T. Introduction to composite materials. Lancaster: Technomic Publishing Company; 1980.
[51] Mori T, Tanaka K. Average stress in matrix and average elastic energy of materials with misfitting inclusions. Acta Metall 1973;21:571–4.
[52] Shi DL, et al. The effect of nanotube waviness and agglomeration on the elastic property of carbon nanotube-reinforced composites. J Eng Mater Technol 2004;126:250–7.
[53] Li C, Thostenson ET, Chou TW. Effect of nanotube waviness on the electrical conductivity of carbon nanotube-based composites. Compos Sci Technol 2008;68:1445–52.
[54] Li JY, Dunn ML. Micromechanics of magnetoelectroelastic composite materials: average fields and effective behavior. J Intell Mater Syst Struct 1998;9:404–16.
[55] Di Gifico M, Nali P, Brischetto S. Refined Multilayered Plate Elements for Coupled Magneto-Electro-Elastic Analysis. Multidiscip Model Mater Struct 2009;5:119–38.
[56] Alaimo A, Benedetti I, Milazzo A. A finite element formulation for large deflection of multilayered magneto-electro-elastic plates. Compos Struct 2014;107:643–53.
[57] Tounsi A, Bedia EA, Benachour A. A new computational method for prediction of transient hygroscopic stresses during moisture desorption in laminated composite plates with different degrees of anisotropy. J Thermoplast Compos Mater 2005;18:37–58.
[58] Elshafei MA, Alraiess F. Modeling and analysis of smart piezoelectric beams using simple higher order shear deformation theory. Smart Mater Struct 2013;22:035006.
[59] Mohammadrezazadeh S, Jafari AA. Vibration suppression of truncated conical shells embedded with magnetostrictive layers based on first order shear deformation theory. J Theor Appl Mech 2019;57:957–72.
[60] Brischetto S, Tornabene F. Advanced GDQ models and 3D stress recovery in multilayered plates, spherical and double-curved panels subjected to transverse shear loads. Compos B Eng 2018;146:244–69.
[61] Tornabene F, Viscoti M, Dimitri R. On the Importance of the Recovery Procedure in the Semi-Analytical Solution for the Static Analysis of Curved Laminated Panels: Comparison with 3D Finite Elements. Materials 2024;17:588.
[62] Li XW, et al. Pyroelectric and electrocaloric materials. J Mater Chem C 2013;1:23–37.
[63] Zhang D, Wu H, Bowen CR, Yang Y. Recent advances in pyroelectric materials and applications. Small 2021;17:2103960.
[64] Benveniste Y. Magnetoelectric effect in fibrous composites with piezoelectric and piezomagnetic phases. Phys Rev B 1995;51:16424.
[65] Salehipour H, Shahmohammadi MA, Folkow PD, Civalek O. An analytical solution for vibration response of CNT/GPL/fibre/polymer hybrid composite micro/nanoplates. Mech Adv Mater Struct 2024;31:2094–114.
[66] Nie GJ, Zhong Z. Semi-analytical solution for three-dimensional vibration of functionally graded circular plates. Comput Methods Appl Mech Eng 2007;196:4901–10.
[67] Reddy JN, Ruocco E, Loya JA, Neves AM. Theories and analyses of functionally graded circular plates. Composites, Part C: Open Access 2021;5:100166.
[68] Wu CP, Liu YC. A review of semi-analytical numerical methods for laminated composite and multilayered functionally graded elastic/piezoelectric plates and shells. Compos Struct 2016;147:1–15.
[69] Thai HT, Kim SE. Analytical solution of a two variable refined plate theory for bending analysis of orthotropic Levy-type plates. Int J Mech Sci 2012;54:269–76.
[70] Oktem AS, Chaudhuri RA. Levy type analysis of cross-ply plates based on higher-order theory. Compos Struct 2007;78:243–53.
[71] Chaudhuri RA. On boundary-discontinuous double Fourier series solution to a system of completely coupled PDE's. Int J Eng Sci 1989;27:1005–22.
[72] Chaudhuri RA. On the roles of complementary and admissible boundary constraints in Fourier solutions to the boundary value problems of completely coupled r th order PDEs. J Sound Vib 2002;251:261–313.
[73] Oktem AS, Soares CG. Boundary discontinuous Fourier solution for plates and doubly curved panels using a higher order theory. Compos B Eng 2011;42:842–50.
[74] Kulikov GM, Plotnikova SV. Coupled thermoelectroelastic analysis of thick and thin laminated piezoelectric structures by exact geometry solid-shell elements based on the sampling surfaces method. Int J Numer Meth Eng 2021;122:2446–77.
[75] Kulikov GM, Plotnikova SV. Three-dimensional thermoelectroelastic analysis of structures with distributed piezoelectric sensors and actuators with temperature-dependent material properties. Mech Adv Mater Struct 2023;30:3979–96.
[76] Reddy JN. Introduction to the finite element method. New York: McGraw-Hill Education; 2019.
[77] Zienkiewicz OC, Taylor RL. The finite element method: solid mechanics, Vol. 2. New York: McGraw-Hill; 1967.
[78] Khater AH, Temsah RS, Hassan M. A Chebyshev spectral collocation method for solving Burgers'-type equations. J Comput Appl Math 2008;222:333–50.
[79] Shu C, Yeo KS, Yao Q. On the performance of three iterative methods for solution of GDQ algebraic equations. Comput Methods Appl Mech Eng 1998;167:1–15.
[80] Shu C. Differential quadrature and its application in engineering. Berlin Heidelberg: Springer Science & Business Media; 2012.
[81] Tornabene F. Generalized Differential and Integral Quadrature. Bologna: Esculapio; 2023.
[82] Chen W, Wang X, Zhong T. The structure of weighting coefficient matrices of harmonic differential quadrature and its applications. Commun Numer Methods Eng 1996;12:455–9.
[83] Tornabene F, Viscoti M, Dimitri R, Aiello MA. Higher order formulations for doubly-curved shell structures with a honeycomb core. Thin-Walled Struct 2021;164:107789.
[84] Bahadori R, Najafizadeh MM. Free vibration analysis of two-dimensional functionally graded axisymmetric cylindrical shell on Winkler–Pasternak elastic foundation by First-order Shear Deformation Theory and using Navier-differential quadrature solution methods. App Math Model 2015;39:4877–94.
[85] Tornabene F, Dimitri R, Viola E. Transient dynamic response of generally-shaped arches based on a GDQ-time-stepping method. Int J Mech Sci 2016;114:277–314.
[86] Daneshmehr A, Inman DJ, Fakhar AM. Free vibration analysis the cracked FGM beam under bending-torsion loading, using GDQ method. Appl Mech Mater 2013;330:942–7.
[87] Dimitri R, Tornabene F, Zavarise G. Analytical and numerical modeling of the mixed-mode delamination process for composite moment-loaded double cantilever beams. Compos Struct 2018;187:535–53.
[88] Shu C, Chew YT, Richards BE. Generalized differential and integral quadrature and their application to solve boundary layer equations. Int J Numer Meth Fluids 1995;21:723–33.
[89] Striz AG, Wang X, Bert CW. Harmonic differential quadrature method and applications to analysis of structural components. Acta Mech 1995;111:85–94.